

# Electromagnetic transitions as a probe for Superdeformation in $^{28}\text{Si}$

Luke Gareth Morris

Doctor of Philosophy

University of York

Physics

September 2019

---

## Abstract

There is great interest in superdeformation in light nuclei,  $A < 40$  region, in particular alpha-conjugate nuclei in the sd-shell. Enhanced collectivity for such light systems opens new opportunities to test nuclear-structure theories. Antisymmetrized molecular dynamics, large-scale shell model and beyond mean-field calculations which predict superdeformed structures in these regions can be validated and tuned with the aid of experimental evidence of superdeformed bands in light nuclei. A  $J^\pi = 6^+$  state at 12.865 MeV in  $^{28}\text{Si}$  with a measured  $B(E2)$  value of more than 25 W.u for the transition to the 10.946-MeV  $J^\pi = 4^+$  state is indicative of a highly collective transition and has been thought to form part of a candidate SD band. Measurements of in-band electromagnetic transitions are required to fully describe this proposed SD band. The CAGRA campaign is a combination of small-angle inelastic scattering with high resolution  $\gamma$ -ray spectroscopy. This method preferentially populates low-spin and isoscalar natural parity states. A 12 Clover + 4 LaBr<sub>3</sub> array was used in coincidence with the high resolution Grand Raiden spectrometer to momentum analyse inelastically scattered  $\alpha$ -particles. The experiment was performed at the Research Center for Nuclear Physics (RNCP) of Osaka University, Japan. This thesis will focus on the experimental challenges, analysis and results of the  $^{28}\text{Si}(\alpha, \alpha')$  reaction at  $9.1^\circ$  with  $E_{\text{beam}}^\alpha = 130$  MeV impinging on a  $^{\text{nat}}\text{Si}$  target. The first upper limits of the in-band  $\gamma$ -ray transition strength of 6.08 W.u from the  $J^\pi = 4^+$  to  $J^\pi = 2^+$  of the proposed superdeformed band in  $^{28}\text{Si}$  has been measured. This has the potential to constrain future theoretical predictions of superdeformation in  $^{28}\text{Si}$ .

# Contents

<b>List of Tables</b>	<b>6</b>
<b>List of Figures</b>	<b>7</b>
<b>1 Introduction</b>	<b>13</b>
1.1 Superdeformation in Nuclei . . . . .	16
1.2 Predictions of Superdeformation $^{28}\text{Si}$ . . . . .	21
1.3 Previous Evidence of Superdeformation in $^{28}\text{Si}$ . . . . .	25
<b>2 Theory</b>	<b>31</b>
2.1 Nuclear Deformation . . . . .	33
2.2 Electromagnetic transitions . . . . .	41
2.3 Reaction Theory . . . . .	44
2.4 Angular Correlations . . . . .	48
<b>3 Experimental Set-up</b>	<b>51</b>
3.1 CAGRA Project . . . . .	51
3.2 RCNP Facility . . . . .	52
3.3 Accelerator Capabilities . . . . .	52
3.4 Grand Raiden Spectrometer . . . . .	54
3.5 CAGRA Array . . . . .	63
3.6 Digital Acquisition . . . . .	69
3.7 CAGRA Data Analysis . . . . .	70

<b>4</b>	<b>Grand Raiden Corrections</b>	<b>71</b>
4.1	VDC Drift Time Corrections . . . . .	71
4.2	Time of Flight Corrections . . . . .	74
4.3	Particle Identification . . . . .	76
4.4	Kinematic Corrections . . . . .	77
4.5	Excitation Spectrum . . . . .	78
<b>5</b>	<b>CAGRA Analysis</b>	<b>82</b>
5.1	Energy Calibration: Clover Crystals . . . . .	82
5.2	CAGRA Efficiency . . . . .	84
5.3	Prompt Timing . . . . .	90
5.4	Clover Energy Rate Dependence . . . . .	91
5.5	Kalman Filter Baseline . . . . .	92
5.6	Clover Energy Determination . . . . .	93
5.7	Doppler Energy Corrections . . . . .	97
5.8	Addback Implementation . . . . .	102
5.9	BGO Suppression . . . . .	106
5.10	$\gamma$ -Ex Background Subtraction . . . . .	109
5.11	CAGRA $\gamma - \gamma$ Analysis . . . . .	110
5.12	LaBr <sub>3</sub> Analysis . . . . .	112
<b>6</b>	<b>Results</b>	<b>116</b>
6.1	$\gamma$ -Ex coincidence . . . . .	116
6.2	Ground-state & $\beta$ band . . . . .	120
6.3	Octupole Collectivity . . . . .	122
6.4	Unnatural parity state . . . . .	127
6.5	Unassigned states . . . . .	129
6.6	Search for the SD in-band transition . . . . .	130
6.7	$\gamma$ -branching ratios . . . . .	135

*CONTENTS*

---

6.8	Angular Correlations . . . . .	138
6.9	$\gamma$ - $\alpha$ Branching ratios . . . . .	141
6.10	SD In-Band transition B(E2) limit . . . . .	144
<b>7</b>	<b>Conclusions &amp; Further Work</b>	<b>146</b>
	<b>Bibliography</b>	<b>149</b>

# List of Tables

2.1	Weisskopf Estimates . . . . .	43
3.1	Specifications of Grand Raiden . . . . .	55
3.2	Ion-Optics calculations . . . . .	60
3.3	Summary of CAGRA positions, HV values and shielding used. . . . .	64
4.1	Multidimensional fit for kinematic corrections . . . . .	78
5.1	Calibration and absolute efficiency source information . . . . .	83
5.2	CAGRA crystal specifications . . . . .	89
6.1	All experimentally observed states, labels correspond to peaks in Figure 6.2. . . . .	119
6.2	Data from ENSDF evaluated data tables on relevant electromagnetic transitions in $^{28}\text{Si}$ . . . . .	131
6.3	$\gamma$ -ray branching ratio calculations for the $J^\pi=(4_7^+)$ state . . . . .	136
6.4	Fitted Optical model potential parameters . . . . .	138
6.5	Derived Optical model potentials and diffuseness parameters . . . . .	138
6.6	Polar angles and corresponding azimuthal angle as used in angcor . . . . .	139
6.7	Experimental angular correlation data and comparison to angcor . . . . .	141
6.8	CAGRA to focal plane ratios for all states populated in $^{28}\text{Si}$ . . . . .	142
6.9	W.u calculations scaled by $\text{BR}_{\alpha/\gamma}$ values . . . . .	144
6.10	Updated transitions strength with the addition of the in-band transition esti- mate. . . . .	145

# List of Figures

1.1	Ikeda Diagram . . . . .	14
1.2	HFB calculation of predicted toroidal shapes in nuclei . . . . .	16
1.3	Deformed Harmonic Oscillator Potential . . . . .	18
1.4	Superdeformed $^{36}\text{Ar}$ level scheme . . . . .	20
1.5	Illustration of the diverse clustering phenomena in nuclei . . . . .	22
1.6	Level scheme predictions from AMD calculations in $^{28}\text{Si}$ . . . . .	23
1.7	Energy surface plot from AMD calculations for $^{28}\text{Si}$ . . . . .	24
1.8	Intrinsic matter density distribution for $^{28}\text{Si}$ from AMD calculations . . . . .	25
1.9	Previous $\gamma$ -ray spectroscopy studies on $^{28}\text{Si}$ using Gammasphere . . . . .	27
1.10	Focal plane spectra from iThemba labs for the $^{28}\text{Si}(\alpha, \alpha')^{28}\text{Si}^*$ reaction from iThemba labs . . . . .	28
1.11	Differential Cross Section for the $J^\pi = 0^+$ band head of the SD band . . . . .	29
2.1	Finite-Range Liquid Drop Model predictions . . . . .	32
2.2	Nuclear Quadrupole Deformation . . . . .	35
2.3	$\Omega$ quantum number for the rotational model . . . . .	37
2.4	$I(I+1)$ linear energy dependence in rotational bands . . . . .	40
2.5	Traditional method of populating S.D bands in heavy nuclei . . . . .	45
2.6	DWBA prediction for inelastic scattering cross section . . . . .	47
3.1	Birdseye view of the RCNP facility . . . . .	52
3.2	Birdseye view of Grand Raiden Spectrometer . . . . .	54

---

3.3	Ion-optics for no dispersion matching . . . . .	56
3.4	Ion-optics for spatial dispersion matching condition. . . . .	57
3.5	Ion-optics for angular and spatial dispersion matching condition. . . . .	57
3.6	Layout of GRAF mode at RCNP. . . . .	59
3.7	Schematic view of the Grand Raiden focal plane detectors. . . . .	61
3.8	MWDC set-up . . . . .	63
3.9	CAGRA array set-up . . . . .	64
3.10	Typical $\gamma$ -ray interactions with a clover detector . . . . .	66
3.11	Data acquisition set-up . . . . .	69
4.1	Time distributions for MWDC's . . . . .	73
4.2	Converted drift time to drift length for the MWDC's . . . . .	73
4.3	Time of flight Corrections . . . . .	75
4.4	Particle Identification Plots . . . . .	76
4.5	Kinematic Corrections of the focal plane detectors . . . . .	78
4.6	Final full corrected focal plane spectra, showing the uncalibrated excitation spectrum of $^{28}\text{Si}$ . . . . .	79
4.7	Focal plane peak fitting procedure . . . . .	80
4.8	Focal plane calibration . . . . .	80
4.9	Calibrated singles focal plane spectrum . . . . .	81
5.1	$\gamma$ -ray energy calibration spectra . . . . .	83
5.2	$\gamma$ -ray energy calibration fitting . . . . .	84
5.3	Full energy $\gamma$ -ray photopeak fitting procedure . . . . .	86
5.4	CAGRA Absolute efficiency . . . . .	87
5.5	Prompt timing distribution between CAGRA timestamp and a coincident GR timestamp . . . . .	90
5.6	$\gamma$ -ray energy rate dependence . . . . .	91
5.7	Baseline sample and Kalman filter implementation . . . . .	93
5.8	$\gamma$ -ray energy determination procedure . . . . .	93

5.9	Pole-zero optimisation . . . . .	95
5.10	Rate dependent shift correction . . . . .	97
5.11	3-D representation of the $\beta$ distribution for a long lived state . . . . .	99
5.12	3-D representation of the $\beta$ distribution for a short lived state . . . . .	100
5.13	$\beta$ optimisation for a state with intermediate lifetime . . . . .	101
5.14	CAGRA crystal multiplicity . . . . .	104
5.15	Addback fold . . . . .	105
5.16	BGO timing . . . . .	106
5.17	BGO suppression implementation . . . . .	107
5.18	BGO spectra . . . . .	108
5.19	$\gamma$ Background subtraction . . . . .	109
5.20	Symmetrical $\gamma$ - $\gamma$ spectrum . . . . .	111
5.21	$\gamma$ - $\gamma$ Background subtraction . . . . .	112
5.22	LaBr <sub>3</sub> prompt timing spectrum . . . . .	113
5.23	Coincident LaBr <sub>3</sub> $\gamma$ -Ex spectra . . . . .	114
5.24	LaBr <sub>3</sub> $\gamma$ -ray energy spectrum . . . . .	115
6.1	$\gamma$ -Ex coincidence spectrum . . . . .	117
6.2	Focal plane coincident spectrum . . . . .	118
6.3	Rotational bands level scheme . . . . .	120
6.4	$\gamma$ -ray spectrum for the $J^\pi=4_1^+$ state of the ground-state oblate rotational band	121
6.5	$\gamma$ -ray spectrum for the $J^\pi=3_1^-$ band head of the $K^\pi=3_1^-$ octupole rotational band	123
6.6	$\gamma$ -ray spectrum for the $J^\pi=3_2^-$ and $J^\pi=5_2^-$ states . . . . .	124
6.7	$\gamma$ -ray spectrum at low energy for the $J^\pi=3_2^-$ and $J^\pi=(5^-, 3^-)$ states . . . . .	125
6.8	$\gamma$ -ray spectrum for the $J^\pi=3_1^+$ state . . . . .	128
6.9	$\gamma$ -ray spectrum for the unassigned state around 11.8 MeV . . . . .	130
6.10	$\gamma$ -ray spectrum for the proposed superdeformed band at intermediate energy .	132
6.11	$\gamma$ -ray spectrum for the proposed superdeformed band at high energy . . . . .	133
6.12	$\gamma$ -ray spectrum for the proposed superdeformed band at low energy . . . . .	134

---

6.13	Derived level Scheme for all direct $\gamma$ -ray transitions observed from populated states in $^{28}\text{Si}$ . . . . .	137
6.14	Experimental angular correlations compared to $\text{angcor}$ for the $J^\pi=4_1^+ \rightarrow 2_1^+$ transition . . . . .	140

# Acknowledgements

First, I want to thank my supervisor Professor David Jenkins for his support and guidance over the past four years. These years have supplied countless unforgettable memories and experiences, so I am very grateful of David for giving me this opportunity. I also appreciate all the help from all the staff members in the University of York nuclear physics group. Particularly Paul Davies for his help during the experiment, I am sure he had a great time in Osaka as I did too. James Cubiss has attended to my aid countless times and I thank him for his caring bedside manner. Jamie Brown has also been great help with the analysis, offering priceless suggestions and wisdom. From other nuclear groups I would like to thank Philip Adsley, who has been very patient with my consistent and constant barrage of stupid questions. All the CAGRA collaborators which helped with the experiment and analysis, particularly Atsushi Tamii, Nobu Kobayashi, Johann Isaak and Muhsin Harakeh. These people were indispensable and the success of this research would have been impossible without them. The RCNP facility staff members also played a huge role through their professionalism and expertise. The many friendships formed throughout these past years are too many to detail in full. I appreciate all the support from my friends. However, to name just a few, first I want to thank Guillaume who made my time in Paris a pleasure. Ben, Chris and Ryan have also supplied endless entertainment throughout my time in York.

Finally, I want to show my deepest appreciation to all of my closest friends and family from home who have been there for me.

# Declaration

I declare that this thesis is a presentation of original work and I am the sole author. This work has not previously been presented for an award at this, or any other, University. All sources are acknowledged as References.

# Chapter 1

## Introduction

The shape evolution of the nucleus illuminates some of the most enigmatic and fundamental properties of nuclear structure. Evidence of the most exotic shapes and vibrations in nuclei have contributed major advancements to nuclear theory. Superdeformation in nuclei is a prime example of the consequences of complex many-body-nucleon interactions. This research aims to study potentially one of the most deformed nuclear states known in nuclear physics. There is growing theoretical interest in  $^{28}\text{Si}$  because of its unique location on the nuclear chart, residing in the middle of the sd-shell.

$^{28}\text{Si}$  has a rich and varied deformation landscape with confirmed shape coexistence (Sheline et al., 1982). It is oblatelly deformed (disk shaped) in its ground-state, through excitation it is known to undergo multiple shape evolutions. It can undergo quadrupole (rugby ball shaped) and octupole deformations (Zalmstra et al., 1991). There is also a  $\beta$ -vibration built upon the  $J^\pi=2_1^+$  state of the ground-state band, further reflecting its complex dynamics (Sheline et al., 1982). A third shape has been proposed in high spin states with triaxial deformation (Sheline et al., 1982). Superdeformation has been theoretically predicted in this region and if experimentally confirmed, could have profound consequences on our understanding of nuclear clustering phenomena in nuclei.

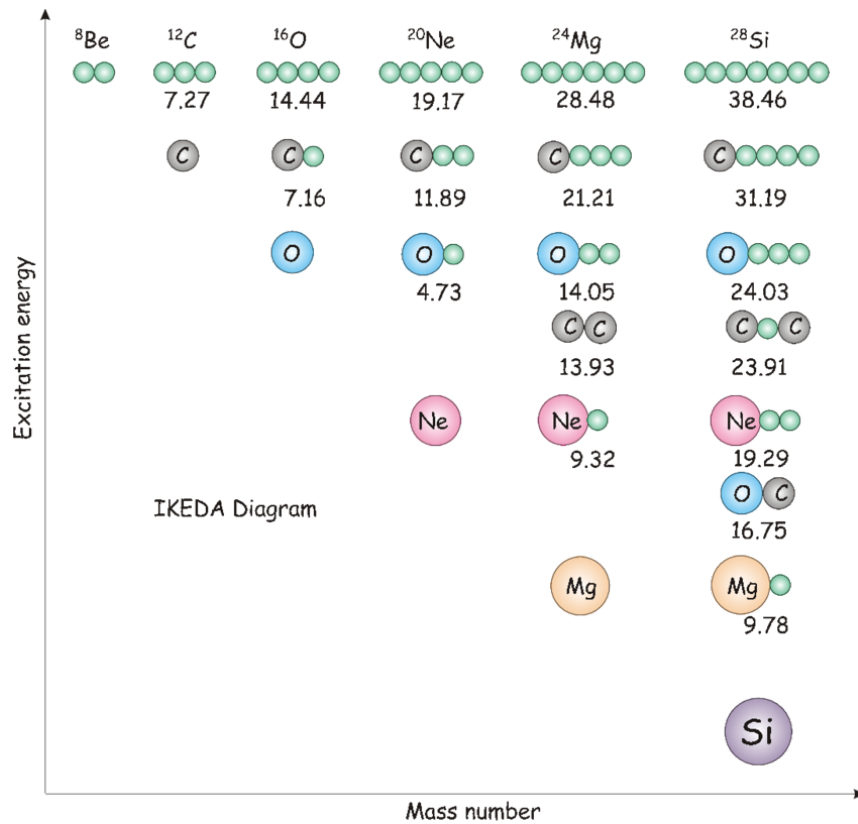


Figure 1.1: The Ikeda diagram which shows a simple picture of nuclear nuclear clustering. As excitation energy increases the clustering degrees of freedom increase (Freer et al., 1995). The linear chain of  $\alpha$ -particles is now widely discarded but the lower degrees of freedom are still predicted in current theoretical models.

There is a tendency for nature to form clustered structures. From astrophysics, through the formation of galaxies (thousands of lights years) to the clustering of atoms in chemistry ( $\text{\AA}$ ), creating molecules. Probing to even smaller lengths scales (fm) the same phenomena occurs within the atomic nucleus. This is most famously described by the Ikeda diagram. Figure 1.1 illustrates a very simple picture, neglecting its true quantum nature, of how the clustering degrees of freedom emerge with excitation energy. For example in  ${}^{12}\text{C}$ , where approximately 7.27 MeV is required to separate it into a 3  $\alpha$ -particle ( ${}^4\text{He}$ ) cluster system. Therefore, excitation energy is required to overcome this mass energy difference and separate the nucleus into smaller constituents. This is the reason cluster structures are expected to form close to and above the break-up threshold of the cluster state. Evidence

of this was found through the Hoyle state (Chernykh et al., 2007). This state is formed through the triple  $\alpha$  process in the initial stages of stellar nucleosynthesis. Firstly, two  $\alpha$  particles fuse together, to form an unstable intermediate  ${}^8\text{Be}$ , a third  $\alpha$  particle is captured through a 7.65 MeV resonance in  ${}^{12}\text{C}$ , forming a  $3\alpha$  cluster state (Chernykh et al., 2007). This has profound implications on the existence of human life. Without this cluster state we could not explain the natural abundance of  ${}^{12}\text{C}$ , which forms the basis of all living matter.

The Ikeda diagram also shows the possible cluster states in  ${}^{28}\text{Si}$ , with a  ${}^{24}\text{Mg} + \alpha$  cluster emerging around 9.78 MeV. At much higher energy, a  $7\alpha$  cluster state becomes energetically possible. A recent experiment has observed a  $7\alpha$  disassembly resonance in  ${}^{28}\text{Si}$  at very high excitation via a  ${}^{28}\text{Si} + {}^{12}\text{C}$  fusion reaction (Cao & Kim, 2018). Figure 1.2 shows the calculated excitation energy against quadrupole moment (Staszczak & Wong, 2014). For  ${}^{28}\text{Si}$  some toroidal shapes were predicted to be possible. This could reflect the Ikeda picture, with a  $7\alpha$  cluster structure, however now in a closed ring formation.

It's clear that there is an interesting and natural connection between superdeformation in nuclei and nuclear clustering phenomena. It is therefore important to review our current understanding of superdeformation and the relevant models which can be used to explain them.

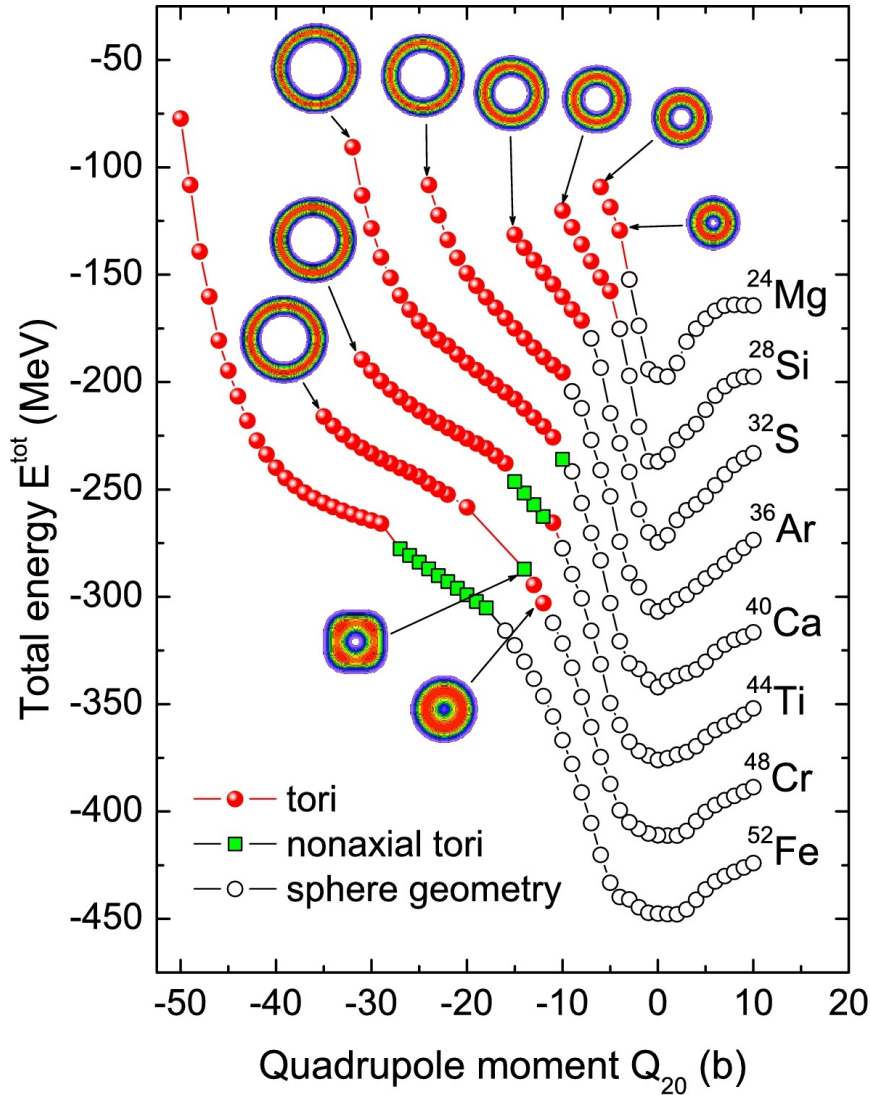


Figure 1.2: HFB calculation of predicted toroidal shapes in different nuclei (Staszczak & Wong, 2014).

## 1.1 Superdeformation in Nuclei

The first experimental observation of superdeformation in nuclei was certainly an unexpected discovery for the physics community. It was commended publicly in *Physics Today* by D. Kleppner being on par with the discovery of buckyballs and the supernovae 1987A observation around the same period (D.Kleppner, 1991). One of the major milestones leading up to their discovery was the addition of a shell-correction energy to the Nilsson

model, called the Strutinsky method (Strutinsky, 1967). Striking predictions from this model included a second minimum in the potential energy surface at large deformation. This double-humped structure was observed by Flerov et.al. in the search for heavy elements in the 60's (Flerov & Ter-Akopian, 1987). During the first production of  $^{260}\text{Rf}$ ,  $\gamma$  decays were still detected up to 15 ms after synthesis. This could be only explained by the Strutinsky model. Here,  $^{260}\text{Rf}$  was produced in a meta-stable state within a second minimum of the potential energy surface. To reduce its energy, it could either quantum-mechanically tunnel through the barrier to the normally deformed band, explaining the increased  $\gamma$ -decay lifetime, or fission. The first superdeformed rotational band was not discovered until 1986 (Twin et al., 1986). Here, states up to  $60\hbar$  in  $^{152}\text{Dy}$  were seen with 19 transitions equally spaced from 602 to 1449 keV, known as the picket fence. The measured moment of inertia of  $85 \pm 2 \hbar^2 \text{ MeV}^{-1}$  corresponded to that of a superdeformed band with  $\beta \approx 0.6$ .

This discovery was influential on the commissioning of many  $\gamma$ -ray spectrometers such as Gammasphere, Euroball and later GRETINA and AGATA. With these arrays, many superdeformed bands have been discovered around the mass regions 40, 60, 80, 130, 150, 190 and 240.

This grouping can be explained through a simple deformed harmonic oscillator potential model, as seen in Figure 1.3. Large shell gaps are preserved for a 2:1 ratio of the major to minor axis in  $\beta$ -deformed nuclei and additionally new energy degeneracies are formed. Typical ratios of 1.5:1 to 2:1 are then broadly characterised as superdeformed. There has been no experimental evidence of hyperdeformation, ratios up to 3:1. However, recent SU(3) theoretical models have predicted such phenomena in light nuclei. Here, shape isomers are formed with a third minimum in the potential energy surface with hyperdeformation (Cseh et al., 2019).

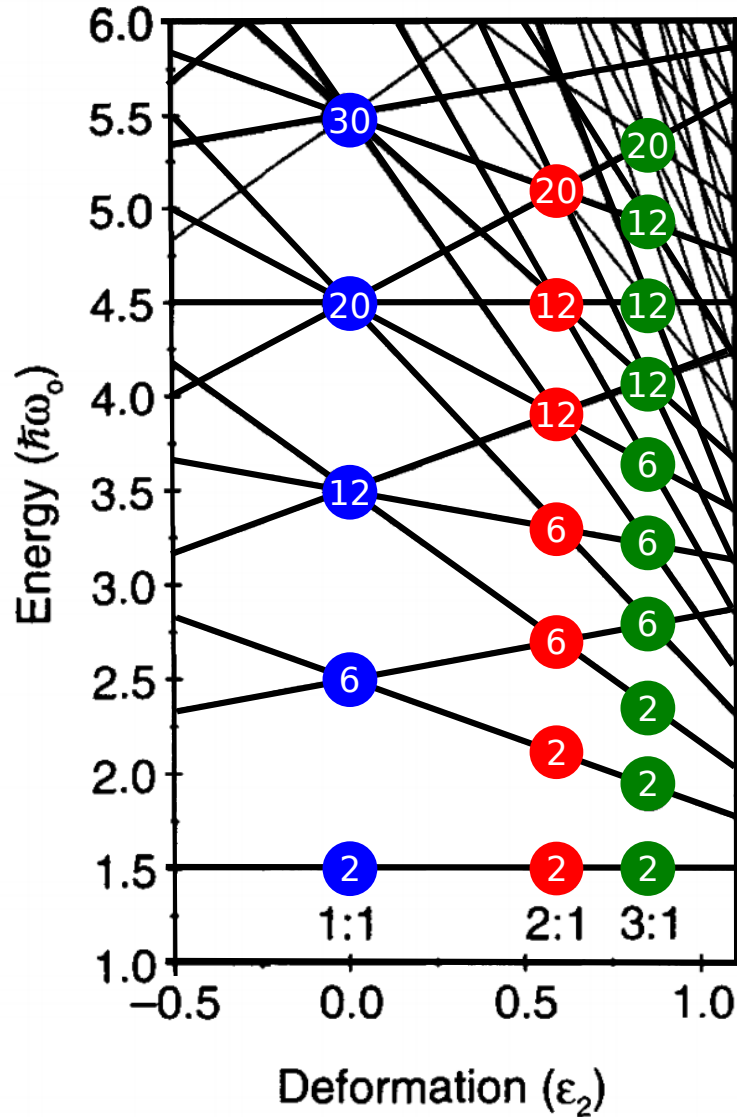


Figure 1.3: Deformed harmonic oscillator potential energy levels. New energy level degeneracies are formed as the nucleus is deformed. The blue circles represent level degeneracies for spherical nuclei, red for superdeformed and green are for hyperdeformed. Adapted from (Freer et al., 1995).

In heavy nuclei, such as  $^{152}\text{Dy}$ , the SD bands can be explained through the Strutinsky method. However, in lighter nuclei this has had limited success. The search for superdeformation in lighter nuclei, particularly in sd-shell nuclei, is of great interest to nuclear theory. Many theories have been applied in this region with rich and varied predictions of the emergence of superdeformation. Nuclei in the sd-shell region serve as a unique testing

ground for exploring mean fields in coexistence with clustering degrees of freedom. These nuclei have shown strong affinity to form  $\alpha$ ,  $^{12}\text{C}$  and  $^{16}\text{O}$  cluster states (Chiba et al., 2017).

The most recently discovered SD band in lighter nuclei was in  $^{42}\text{Ca}$  through a Coulomb excitation study (Hadyńska-Klęk et al., 2016). That study, was performed at Laboratori Nazionali di Legnaro using a 170-MeV  $^{42}\text{Ca}$  beam impinged on a  $^{208}\text{Pb}$  and  $^{197}\text{Au}$  target. The electromagnetic transitions following the subsequent Coulomb excitation were then measured with AGATA (Akkoyun et al., 2012). A superdeformed and slightly triaxial sideband built on the  $J^\pi=0_2^+$  state was found to have a  $\beta = 0.43(2)$  and  $\gamma = 13(_{-6}^{+5})^\circ$  (Hadyńska-Klęk et al., 2016). However, this method is unavailable to probe superdeformation in  $^{28}\text{Si}$ , since the band head for the proposed SD band lies at 9.7 MeV. Coulomb excitation would not permit a single step excitation to this energy within the Cline's safe energy criterion (Zielińska & Gaffney, 2016).

The lightest superdeformed band was found in the, N=Z nucleus,  $^{36}\text{Ar}$ , through the  $^{24}\text{Mg}(^{20}\text{Ne}, 2\alpha)^{36}\text{Ar}$  reaction (Svensson et al., 2000). High-spin states were populated up to  $J^\pi = 16^+$  and connected to states down to low-spin, as seen on the left of Figure 1.4 on the simplified level scheme. They used the spherical shell model and cranked Nilsson-Strutinsky calculations to determine  $\beta \approx 0.45$ . The insert shows the comparison between the experiment and shell model calculation. Almost pure rotational behaviour is seen up to  $10\hbar$ , where backbending starts to occur.

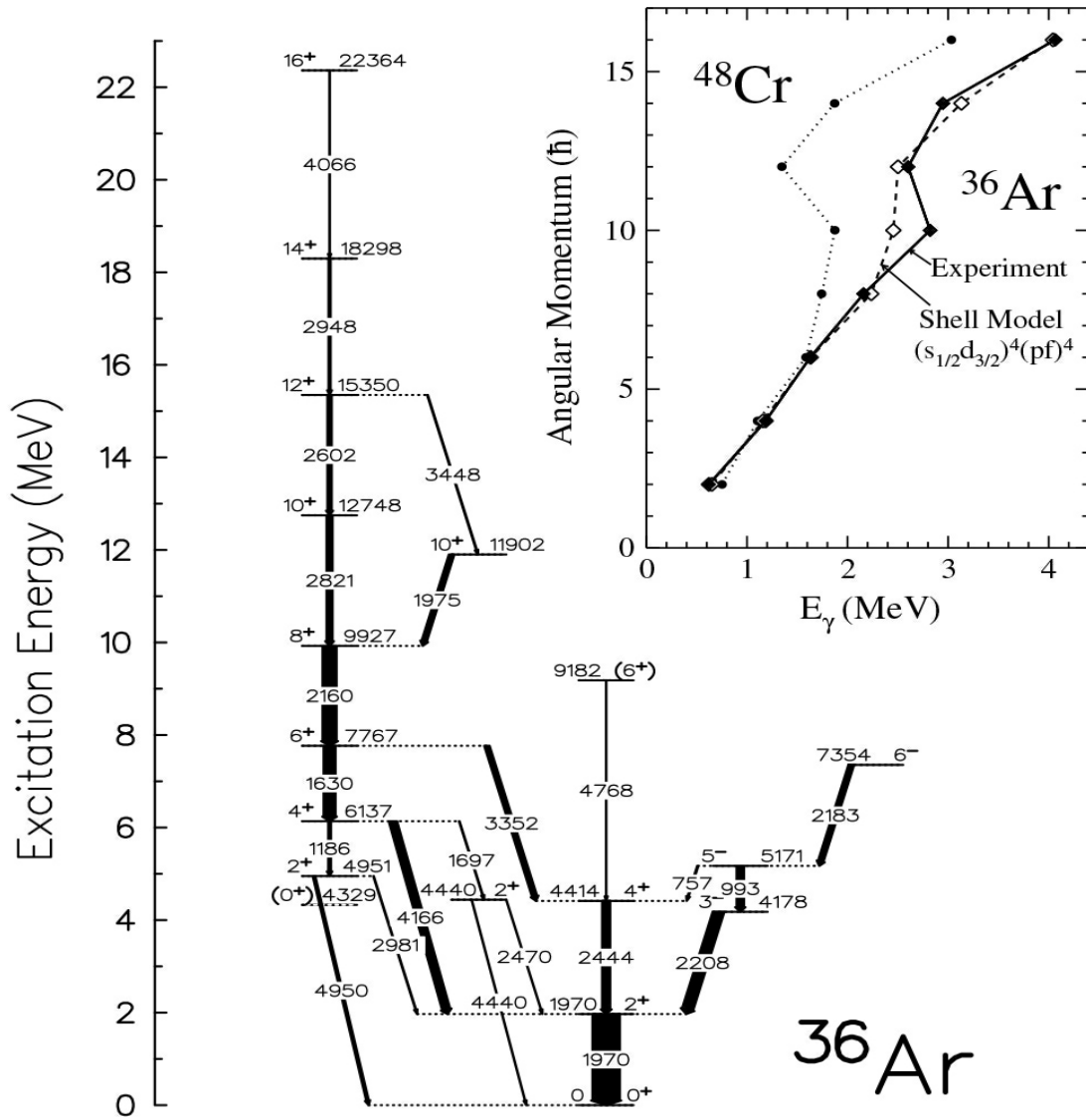


Figure 1.4: Simplified level scheme, detailing the superdeformed band in  $^{36}\text{Ar}$ , the lightest system to undergo superdeformation (Svensson et al., 2000).

## 1.2 Predictions of Superdeformation $^{28}\text{Si}$

The first theoretical models used to predict SD in light nuclei were based on the anisotropic harmonic oscillator model (Cseh & Scheid, 1992). This takes the 1-D simple harmonic oscillator potential into 3-D. The deformation is assumed to be ellipsoidal with  $a_1:a_2:a_3=\omega_1:\omega_2:\omega_3$ , where  $a_i$  is the axis length and  $\omega_i$  is the oscillator quanta frequency in  $i^{\text{th}}$  direction. The potential is then formed from the sum of the standard harmonic oscillator potential for each axis:

$$V = \frac{1}{2} m \sum_{i=1}^3 \omega_i^2 x_i^2, \quad (1.1)$$

then the predicted single particle energies are given by:

$$E(n_1, n_2, n_3) = \hbar \sum_{i=1}^3 \omega_i (n_i + \frac{1}{2}). \quad (1.2)$$

These form the basis of the Harvey's and Wildermuth's descriptions. The former relates highly deformed states to the clustering degrees of freedom, while the latter connects the cluster model to a shell model basis. Applying these, Cseh *et al* predicted  $^{24}\text{Mg} + \alpha$ ,  $^{20}\text{Ne} + 2\alpha$  and  $^{16}\text{O} + 3\alpha$  alpha cluster structures with 2:1:1 deformation ratios (Cseh & Scheid, 1992).

Antisymmetrized molecular dynamics (AMD) is one of the main and most recent nuclear models to describe nuclear clustering. This approach has been applied to a diverse range of nuclear structure phenomena, molecular resonances,  $\alpha$ -condensation and heavy-ion collision and many more as illustrated in Figure 1.5. AMD brings together coexistence between clustering and the mean-field. Its main approach is to express the wavefunction through a sum of independently localised Gaussian wave packets, each one representing either a single nucleon or cluster structure.

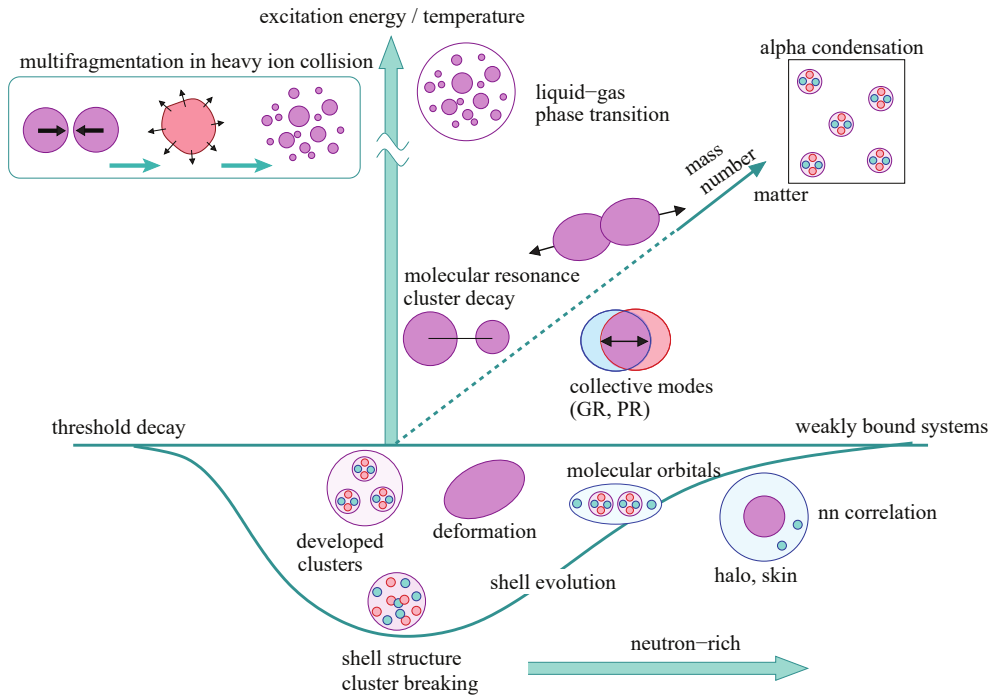


Figure 1.5: Illustration of the diverse clustering phenomena in nuclei depending on isospin and excitation energy. There is an emergence of clustering degrees of freedom with excitation energy which is in competition with mean-field effects, at lower excitation energies. AMD calculations unify both mean-field and clustering effects into one complete framework. (Kanada-En'yo et al., 2012).

A recent calculation performed on  $^{28}\text{Si}$  by Taniguchi *et al* used a deformed-basis AMD model including multi-configuration mixing. They also constrained the quadrupole deformation parameter,  $\beta$ , and distance,  $d$ , between possible clusters (Taniguchi et al., 2009). They also studied excited states in  $^{28}\text{Si}$  by applying energy variation to both  $\beta$  and  $d$ . This method has proven successful in other light superdeformed nuclei. It was applied

to superdeformation in  $^{42}\text{Ca}$ , where predicted  $B(E2)$  values were in good agreement with experiment (Taniguchi et al., 2007). They reproduced the oblate band, normal-deformed band and a SD band in  $^{28}\text{Si}$ . The predicted  $B(E2)$  values were also in agreement with experiment. However, no experimental  $B(E2)$  values exist for the proposed SD band in  $^{28}\text{Si}$ , so this was not compared. Furthermore, they predicted the  $J^\pi = 0^+$  band-head to lie at 13.8 MeV, much higher than the best candidate which lies at 9.71 MeV (Adsley & Jenkins, 2017).

Taniguchi *et al* predicted a very large deformation of  $\beta \approx 0.8$  with an angular momentum of  $6 \hbar^2$  MeV for the proposed SD band in  $^{28}\text{Si}$ . In 2017 they made further calculations using AMD, with the Gogny D1S effective interaction (Chiba et al., 2017). Their basis wave functions from the AMD calculation were then used in a generator coordinate method (GCM) calculation. From this they could calculate predicted energy levels.

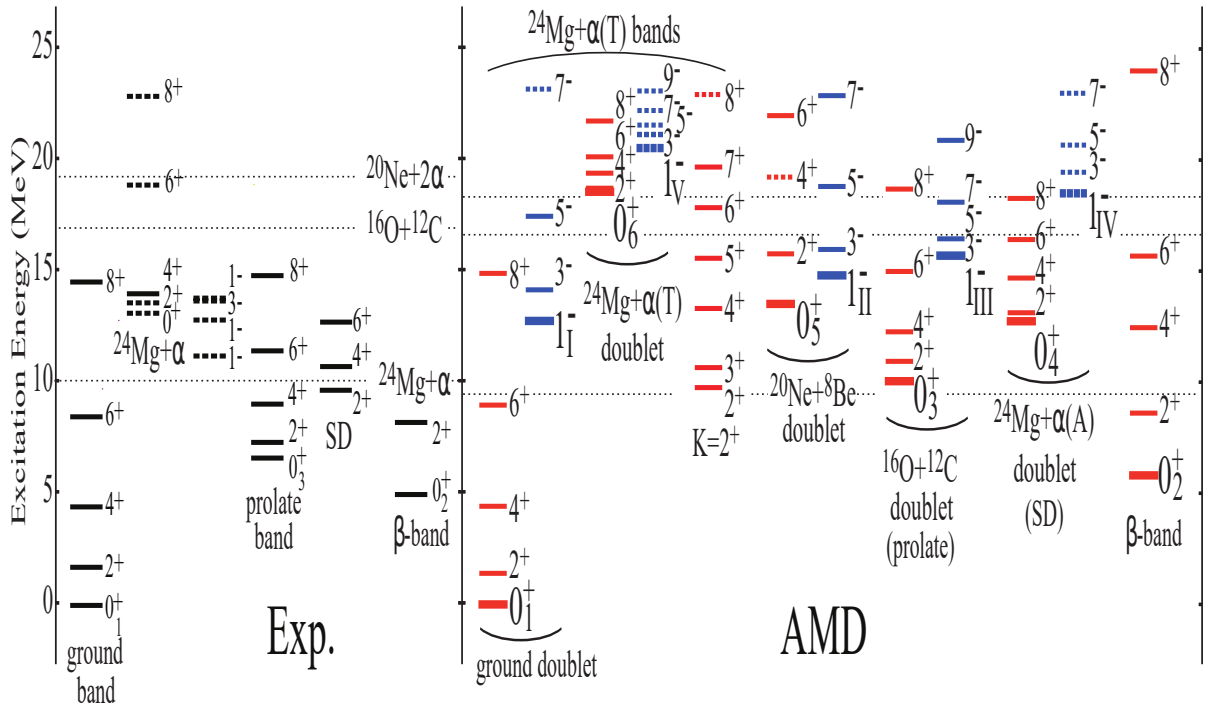


Figure 1.6: AMD calculations with predicted partial level scheme compared to experimentally observed levels in  $^{28}\text{Si}$  (Chiba et al., 2017).

Figure 1.6 shows the comparison between their predictions and experiment. To summarise their results: An oblate minimum in a  $\beta - \gamma$  energy surface plot with mixed  $^{20}\text{Ne} + ^8\text{Be}$  cluster configurations, this was paired with a negative-parity band, labelled  $^{20}\text{Ne} + ^8\text{Be}$  doublet. The oblate minimum is also mixed with  $^{24}\text{Mg} + \alpha$  cluster configurations. This forms a group of band structures, labelled  $^{24}\text{Mg} + \alpha(\text{T})$  in Figure 1.6. The  $^{16}\text{O} + ^{12}\text{C}$  cluster configuration is mixed with the prolate deformed minimum and the SD state minimum is mixed with a  $^{24}\text{Mg} + \alpha$  cluster configuration. Figure 1.7(a) shows the energy surface plot for the  $J^\pi = 0^+$  and Figure 1.7(b) shows the inversion doublet,  $J^\pi = 1^-$ . The most important result was the SD minimum at  $(0.85, 5^\circ)$  and its corresponding matter density distribution in Figure 1.8(c).

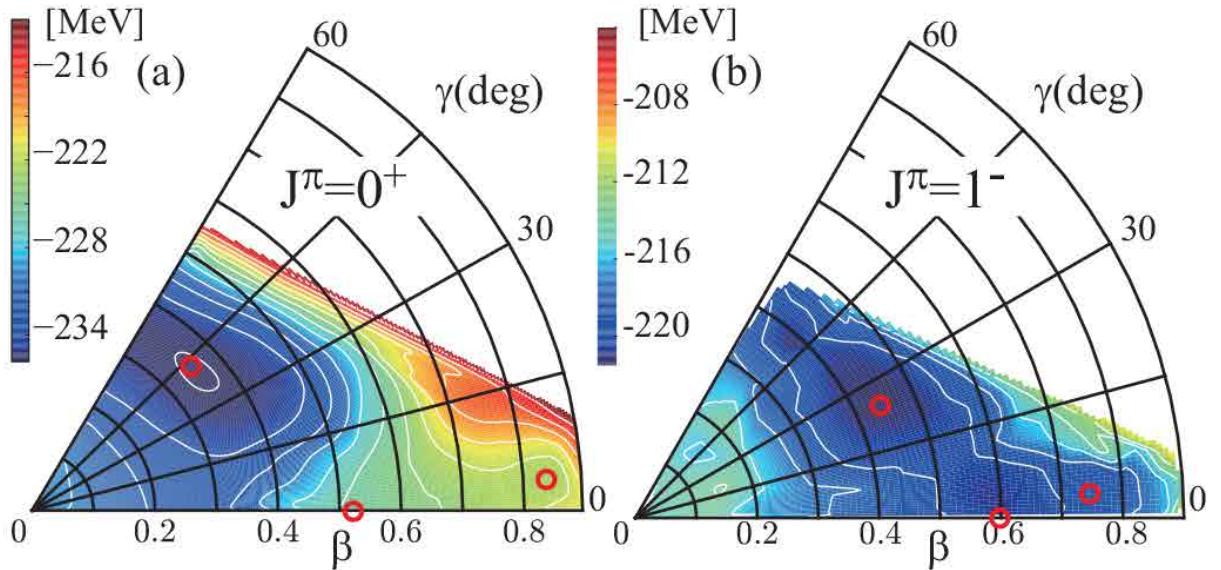


Figure 1.7: (a) Energy surface plot for the  $J^\pi = 0^+$  cases with energy minima at  $(\beta, \gamma) = (0.36, 46^\circ)$  corresponding to oblate deformation, prolate deformation predicted at  $(0.5, 0^\circ)$  and the third minimum at  $(0.85, 5^\circ)$  is the predicted SD state. The red circles indicate the location of each minima. (b) Minima for the  $J^\pi = 1^-$  inversion doublet (Chiba et al., 2017).

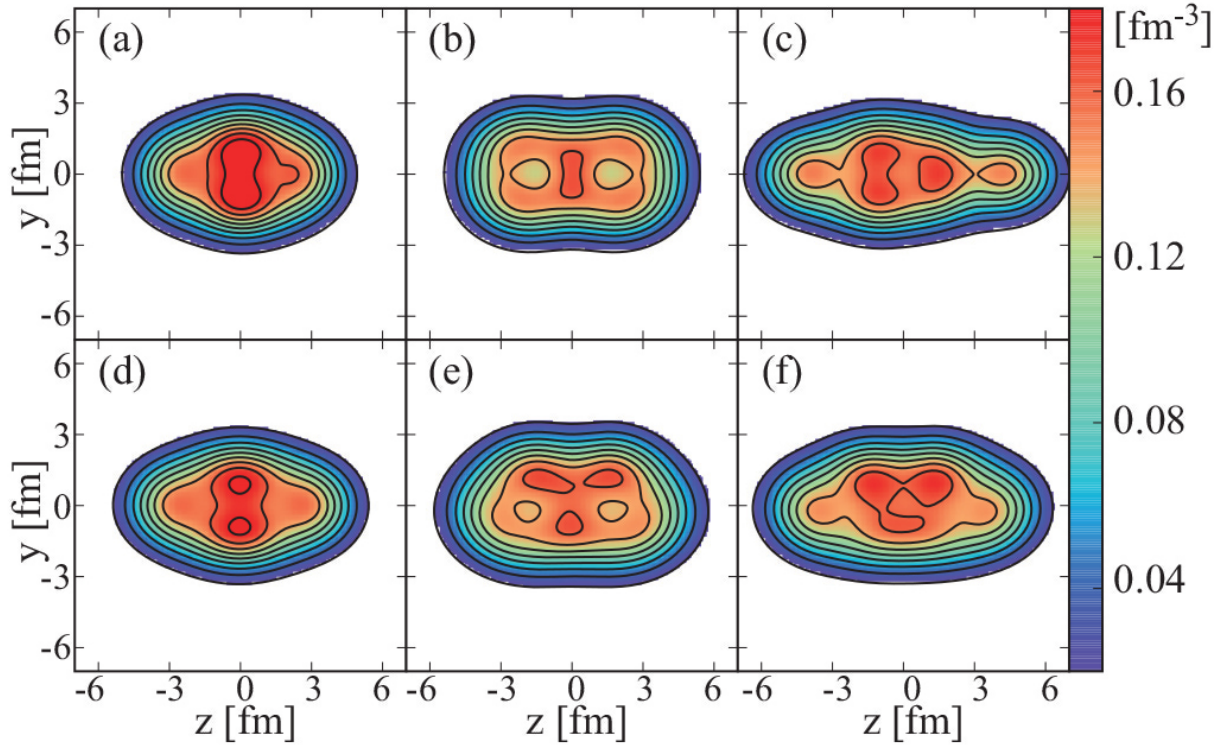


Figure 1.8: Calculated intrinsic matter density distributions corresponding to minima data points on Figure 1.7. Here, (a), (b) and (c) are for the oblate, prolate and SD minima on Figure 1.7(a). The inversion doublets (d), (e) and (f) are from the minima in Figure 1.7(b) (Chiba et al., 2017).

These calculations suggest very rich clustering configurations in  $^{28}\text{Si}$  with large crossover with superdeformation. To get a complete picture of the motivation of this project the experimental evidence linked to these predictions is necessary.

### 1.3 Previous Evidence of Superdeformation in $^{28}\text{Si}$

Pioneering research by Brenneisen *et al* gave the first credible argument for experimental evidence of SD in  $^{28}\text{Si}$  (Brenneisen et al., 1995). This review and research on the structure of  $^{28}\text{Si}$  above 10 MeV is the most detailed study of its kind. Theoretical calculations predicted the band head of the candidate SD band to lie near or above 10 MeV. Therefore, the Brenneisen *et al* research was vital in identifying candidate states belonging to a possible

SD band. Majority of the data included in Brenneisen et al. (1995) came from studying  $^{24}\text{Mg}(\alpha, \gamma)^{28}\text{Si}$  and  $^{27}\text{Al}(p, \gamma)^{28}\text{Si}$  reactions. These reactions do not preferentially populate high spin states due to the high centrifugal barrier. Instead, many of the higher spin states have been studied using n- $\gamma$  coincidence measurements through  $^{25}\text{Mg}(\alpha, n\gamma)$  reactions, such as that performed by Glatz et al. (1981b). Another major campaign for high spin states was carried out by S.Kubono through studying  $^{12}\text{C}(^{20}\text{Ne}, \alpha)$  reactions (Kubono et al., 1986). The main focus of these studies was to learn more about the shape coexistence in  $^{28}\text{Si}$  between the known oblate ground-state band and the excited normally deformed band. However, the  $^{12}\text{C}(^{20}\text{Ne}, \alpha)$  reaction populated a previously unobserved  $J^\pi=6^+$  state, which was later remeasured by Brenneisen *et al* through  $^{24}\text{Mg}(\alpha, \gamma)^{28}\text{Si}$  reactions.

Importantly for this research was the Brenneisen's *et al* measurement of a 1919-keV  $\gamma$ -ray transition from the  $J^\pi = 6^+$  state at 12.86 MeV to a  $J^\pi = 4^+$  level at 10.945 MeV with  $(2J+1)\Gamma_\gamma > 0.37$  ev. The corresponding  $B(E2)$  value for this decay was  $> 25$  W.u. which is indicative of strong collectivity. Furthermore, it's interesting that the most populated state below 12 MeV was the  $J^\pi = 4^+$  state at 10.945 MeV. This had an unexpected yield, 10 times greater than the first and second  $J^\pi = 4^+$  states belonging to the oblate ground-state band and the normally deformed band, respectively. Similar preference for the 10.945-MeV state population was also seen in  $^{24}\text{Mg}(^6\text{Li}, d)$  reaction at 73 MeV bombarding energy (Tanabe et al., 1983).

An experiment performed with the Gammasphere  $\gamma$ -ray spectrometer, ANL, with the main aim to investigate mirror symmetry in  $^{31}\text{S}$  with  $^{31}\text{P}$  was reanalysed by Jenkins et al. (2012). The experiment had a large  $^{28}\text{Si}$  channel population through the  $^{12}\text{C}(^{20}\text{Ne}, \alpha)^{28}\text{Si}$  reaction with an initial beam energy of 32 MeV. Gammasphere includes 100 HPGe detectors with Compton suppression capability. Through  $\gamma$ - $\gamma$  coincidence analysis, the in-band transition from the  $J^\pi=6^+$  to  $J^\pi=4^+$  states of the proposed SD band first seen by Brenneisen et al. (1995) was verified. This was achieved by gating on the out of band transition from the  $J^\pi = 4^+$  state of the SD band. The results show a  $\gamma$ -ray transition at 1919 keV which corresponded to the in-band transition, as seen in Figure 1.9. This result was then the main motivator for this thesis research. The results from the Gammasphere experiment

did not confirm the existence of the superdeformed band. However, it did show promising signs. Considering, transitions from the  $J^\pi = 4^+$  state of the proposed SD band to the oblate ground-state band were subdued, with a  $B(E2) \approx 0.01$  W.u. In contrast, transitions to the normally deformed prolate band seemed to be dominant, with a measured  $B(E2)$  value of  $\approx 5.0$  W.u. This information shows some structural comparison between the proposed SD band and the prolate band. This, together with the large  $J^\pi = 6^+$  to  $J^\pi = 4^+$  transition strength, does suggest a highly deformed rotational band.

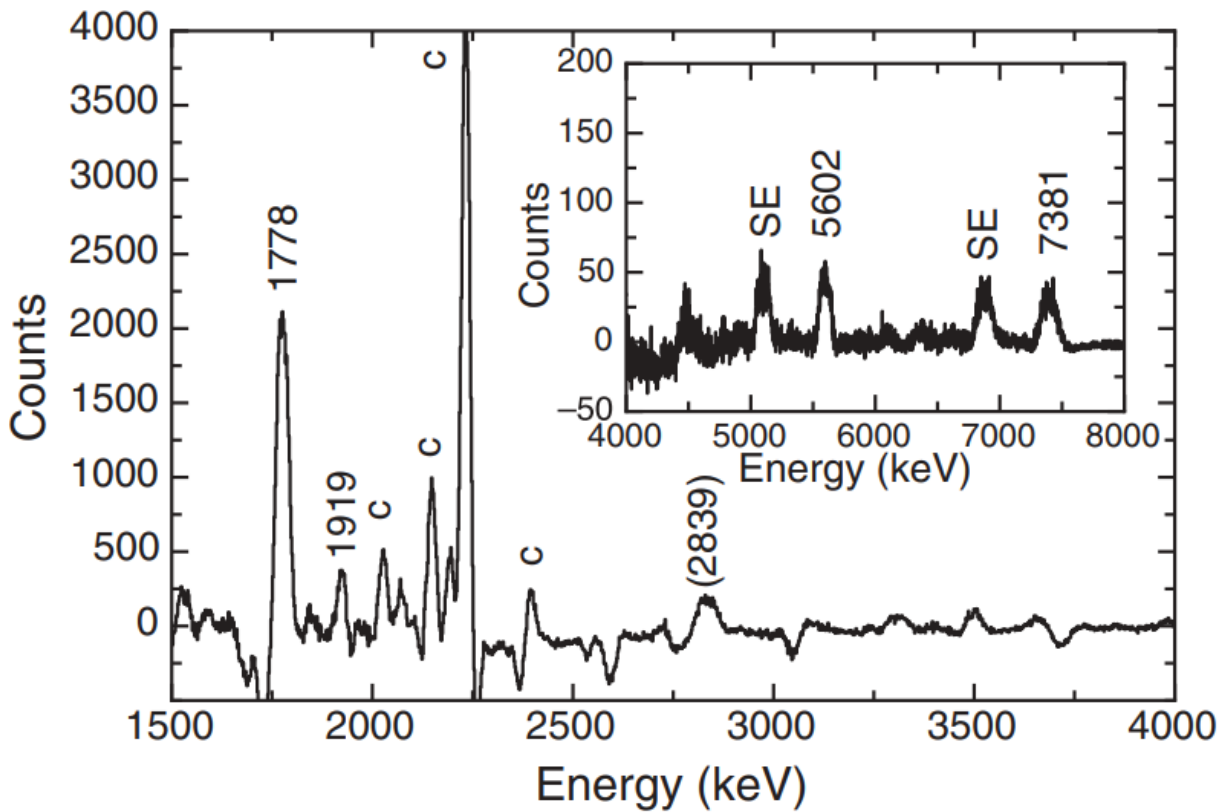


Figure 1.9:  $\gamma$ - $\gamma$  coincidence spectrum taken from a Gammasphere experiment. Events shown were gated on the 3565-keV transition from the 10.945-MeV,  $J^\pi = 4^+$ , state of the proposed SD band. Here, peaks labelled c are contaminate transitions. The insert shows the high energy component of the spectrum where a 1919-keV transition was observed (Jenkins et al., 2012).

A recent and more direct research project on the proposed superdeformed band was performed at iThemba labs, South Africa, where the band-head has been identified (Adsley & Jenkins, 2017) using  $\alpha$ -particle inelastic scattering at angles in the range of  $0$ - $6^\circ$ . The excitation energy of  $^{28}\text{Si}$  was reconstructed using the K600 high resolution spectrometer, this is of very similar design to that of the Grand Raiden spectrometer at Research Centre for Nuclear Physics (RCNP), Osaka.

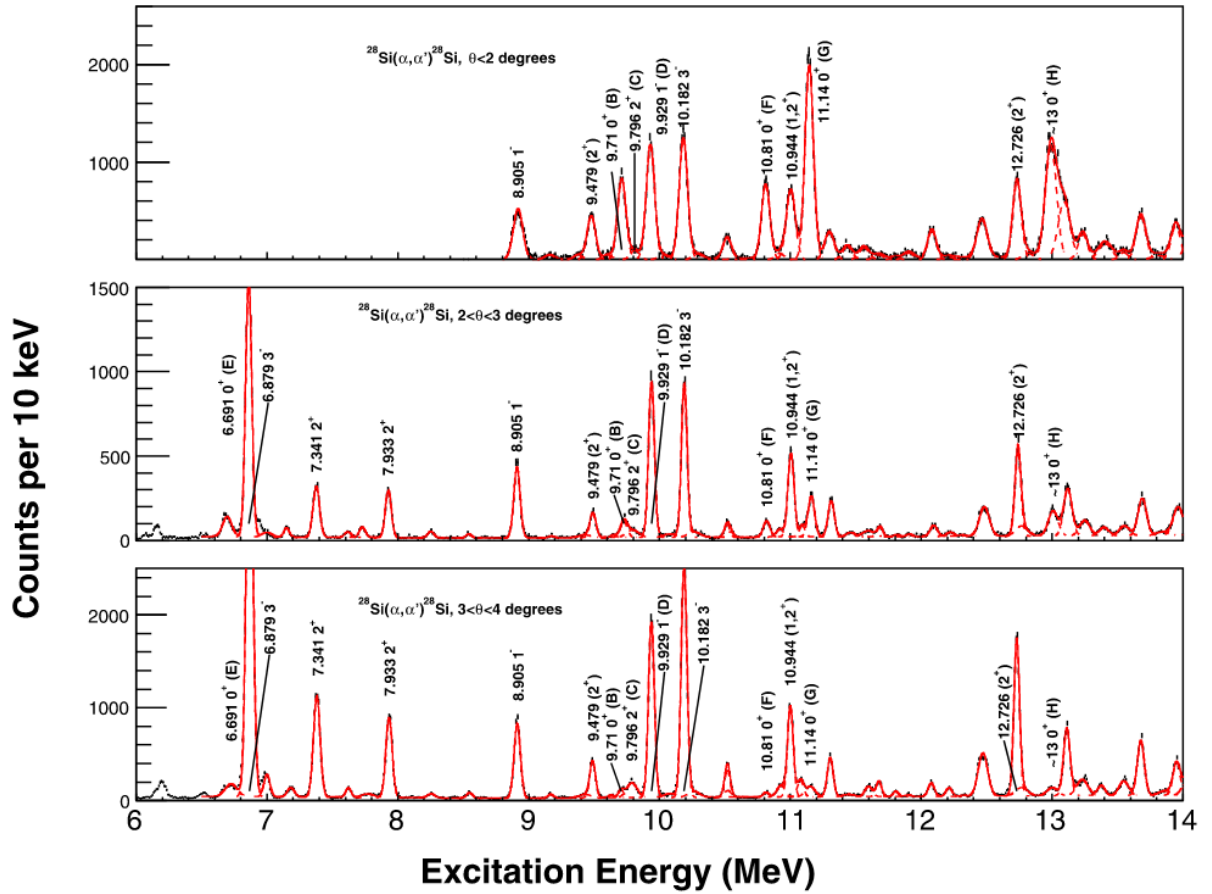


Figure 1.10: Focal plane spectra for the  $^{28}\text{Si}(\alpha, \alpha')^{28}\text{Si}^*$  reaction measured at different scattering angles (Adsley & Jenkins, 2017). This can be used to compare results from this research to check consistency in the reaction mechanism. However, they did not perform measurements as high as  $9.1^\circ$ .

Excitation spectra can be seen in Figure 1.10 from this experiment for varying angles. Several  $J^\pi = 0^+$  states were observed above 9 MeV. Notably, was a  $J^\pi = 0^+$  state identified at 9.71 MeV. This was confirmed by measuring the differential cross section of this state for different scattering angles, as seen in Figure 1.11 (Adsley & Jenkins, 2017). Here, the experimental differential cross section was compared to that calculated for a  $J^\pi = 0^+$  state by DWBA calculations. The two curves correspond to different optical potentials used, both consistent with a  $J^\pi = 0^+$  state, with the differential cross section maximum at  $0^\circ$ . Theoretical predictions from a semimicroscopic algebraic model was in good agreement with the experimental observation (Cseh & Riczu, 2016), therefore they concluded this was indeed the band-head of the proposed SD band.

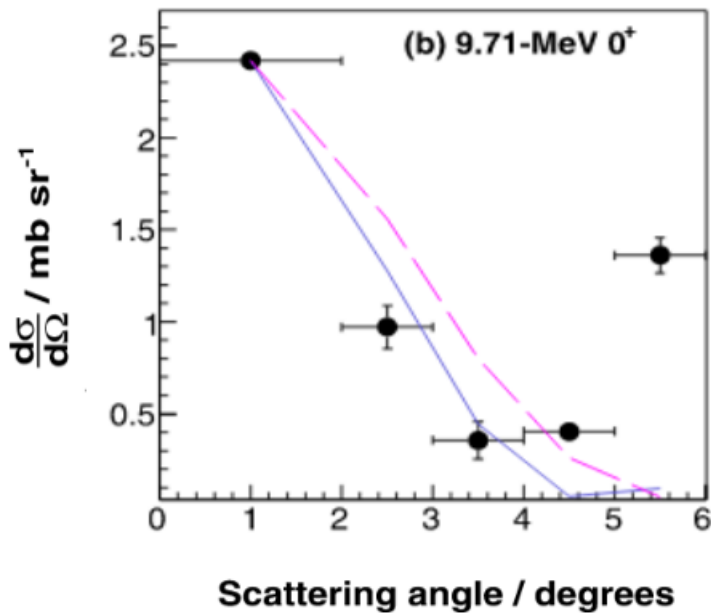


Figure 1.11: Results of the differential cross section for the  $J^\pi = 0^+$  band head of the SD band. The two curves represent different DWBA calculations with alternative optical model parameters both for a  $J^\pi = 0^+$  state distribution (Adsley & Jenkins, 2017).

There were no high resolution  $\gamma$ -ray spectroscopy capabilities available during the experiment at iThemba. Therefore, any electromagnetic transitions from the new  $J^\pi = 0^+$  state of the proposed SD band could not be detected. As the proposed SD band-head lies below the  $\alpha$  particle decay threshold (9984.14 keV) in  $^{28}\text{Si}$ , there should be no competition with particle decay (Wang et al., 2012). The 10.91-MeV  $J^\pi = 4^+$  state of the proposed SD band does lie above this threshold, therefore the branching ratio for the  $\alpha$ -breakup will have to be taken into account. The present research did have high resolution  $\gamma$ -ray spectroscopy capabilities with the CAGRA array. Additionally,  $\alpha$ - $\gamma$  branching ratios can be calculated, as raw focal plane spectra can be compared to gated  $\gamma$  coincidence spectra. If particle decay is forbidden, the state population integral measured at the focal plane should be 1:1 with direct  $\gamma$ -decays from that state in coincidence with the focal plane. Unfortunately, the  $\gamma$  counts have to be efficiency corrected and this can introduce significant error, especially when extrapolating to high  $\gamma$ -ray energies.

# Chapter 2

## Theory

The conventional image of a nucleus is naively spherical considering that the majority all experimentally known nuclei in their ground states are deformed. It is only near specific numbers of protons and neutrons where sphericity is the equilibrium shape. These form the so called closed shell magic nuclei at  $N, Z = 2, 8, 20, 28, 50, 82$  and for neutrons 126. This phenomena shows there is a competition between microscopic and macroscopic effects within the nucleus. The magic numbers are a distinct example of the single particle nature within nuclei, i.e. nucleons moving independently within a mean field potential, in which is the basis of the independent particle model. The introduction of using mean field potentials, such as the Woods-Saxon potential together with the contribution of the spin-orbit interaction was enough to explain the experimentally observed stability at magic numbers.

However, for non-magic nuclei, some notion of collectivity among all of their constituents is required to explain the emergence of deformation. The Nilsson model (Nilsson et al., 1969) and Collective Models are the main groups of models in which explain nuclear deformation. The Nilsson model is an extension of the independent particle model, where the Wood-Saxon is replaced with a deformed potential. The  $2J+1$  degeneracy of each  $J$  state is now broken, as each sub-state no longer orbits within a spherically symmetric potential. The extent to which the sub-states shift in energy depends on the degree of

deformation.

A collective model treats the nucleus within a macroscopic framework. The most famous of these is the liquid drop model (Bethe & Bacher, 1936). This model ignores the individual motion of nucleons and is analogous to molecules within a liquid drop. The ground-state binding energies of nuclei away from magic numbers are well described by this model. More advanced liquid drop models such as the finite-range liquid drop model have increased precision near to magic numbers (Möller et al., 2016) - see Figure 2.1 for its predictions compared to experiment. This model combines both microscopic and macroscopic approaches adding shell corrections to the liquid drop model (Möller et al., 2016). However, these models have limited success in modelling excited states.

Nuclear cluster models have also added to our understanding of the shape of nuclei. Here, certain nuclei can be thought to be made up of building blocks of smaller nuclei, analogous to atomic molecules. A wide range of nuclear cluster models have been applied to explain superdeformation in light nuclei, including  $^{28}\text{Si}$ .

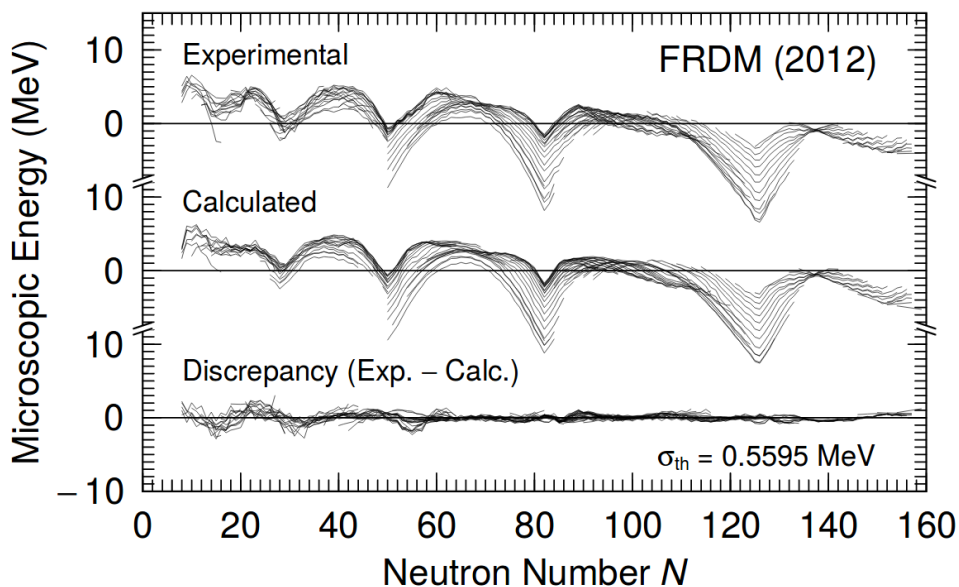


Figure 2.1: Comparisons of 2149 experimentally measured ground-state masses and their predicted values using the finite-range liquid drop model. This model well produces the spikes seen around the magic number regions (Möller et al., 2016).

## 2.1 Nuclear Deformation

### Deformation Parameters

A complete understanding of the complex and often puzzling inner working of nuclei is a huge undertaking for nuclear theory. However, experimentally there are a wide range of model independent observables that can be measured or calculated to characterise nuclear structure. These include charge density distributions, which can be measured via electron elastic scattering (Anni et al., 1995). Fitting to data from such experiments yields the following relation:

$$R = r_0 A^{\frac{1}{3}}, \quad (2.1)$$

which estimates the radius,  $R$ , of a nucleus with mass number  $A$ . Both the radius and the proportional constant,  $r_0$ , can also be experimentally determined via electron elastic scattering measurements (Suda & Wakasugi, 2005). For  $^{28}\text{Si}$ , this corresponds to  $R = 3.796$  fm when  $r_0 = 1.25$  fm and assuming a constant homogeneous density of protons and neutrons. Therefore, if the radius significantly deviates from this value, there must be a significant underlying change in nuclear structure. The major disadvantage of electron scattering is that it is only able to study stable nuclei in their ground states. However, recent advancements in ion trap techniques and storage rings have opened up new possibilities of electron scattering on exotic nuclei (Suda & Simon, 2017). The lifetimes of excited states in light nuclei are in the ps to fs time scale, which is far too short for any coherent elastic scattering methods to achieve appreciable statistics.

The nucleus is a quantum mechanical system with no classically rigid boundary or surface. Therefore, a more appropriate measure of the charge distribution is the root-mean-squared (rms) charge radius (Campbell et al., 2016):

$$\langle r^2 \rangle = \frac{3}{5} r_0^2 A^{\frac{2}{3}} = \frac{\int_0^\infty \rho(\vec{r}) r^2 d^3r}{\int_0^\infty \rho(\vec{r}) d^3r}, \quad (2.2)$$

where,  $\rho$ , is the charge density function. Laser-spectroscopy is one of the main model independent techniques to measure the rms. Here, an isotope shift is seen in atomic

transition frequencies due to changes in size and mass within a particular isotopic chain (Campbell et al., 2016). This technique is only applicable to stable nuclei or long lived isomeric states and is unavailable for the study of short lived excited states.

Any physical system which has a charge distribution will have an associated multipole field. In classical electromagnetism, electric fields are produced via static charge distributions, whereas currents produce magnetic fields. Performing a power series expansion on these fields forms the multipole expansion. The magnitude of each term depends on the charge distribution. A point charge is solely described by the first order term, more commonly known as the monopole and only exist for the electric field, as there is no experimental evidence for magnetic monopoles. The electric dipole is a linear separation of charge and is represented by the second order term. The magnetic dipole field describes a point charge in motion around a closed loop and the third order expansion represents the quadrupole term. For electric fields, the quadrupole term represents four point charges in a square lattice.

This formalism is therefore convenient to represent the spatial and current distribution of nucleons within nuclei. A spherical symmetric charge distribution will have a vanishing dipole moment. Any emergence of quadrupole or higher multipole terms are therefore a unique identifier for nuclear deformation. When nuclei deform, they become elliptical and therefore have a non-zero quadrupole moment. Classically, this term is represented by:

$$Q_0 = \int (\rho(3z^2 - r^2))dV. \quad (2.3)$$

This is a volume integral over the density distribution,  $\rho$ . Here,  $z$  is the position along the symmetry axis as seen in Figure 2.2. It is important to stress that this can not be experimental observed as it only quantifies deformation in the intrinsic reference frame of the nucleus. The nucleus is always spherical in the laboratory frame of reference. However, what can be measured is the experimental spectroscopic quadrupole moment (Campbell et al., 2016):

$$Q_s = \frac{3\Omega^2 - I(I + 1)}{(I + 1)(2I + 3)} Q_0. \quad (2.4)$$

This is the quantum mechanical equivalent of Equation 2.3 but now in the laboratory frame. Here,  $\Omega$  represents the projection of the angular momentum  $I$  quantum number onto the symmetry axis. Therefore, if  $Q_s$  is experimentally measured,  $Q_0$  can be calculated. Figure 2.2 shows how the shape of the nucleus is related to  $Q_s$  with respect to the symmetry axis. For  $Q_s > 0$  the nucleus is stretched out with respect to the symmetry axis, this is known as prolate deformation.  $Q_s < 0$  represents oblate deformation, with the sphere compressed with respect to the symmetry axis.  $Q_s = 0$  occurs only for spherical nuclei.

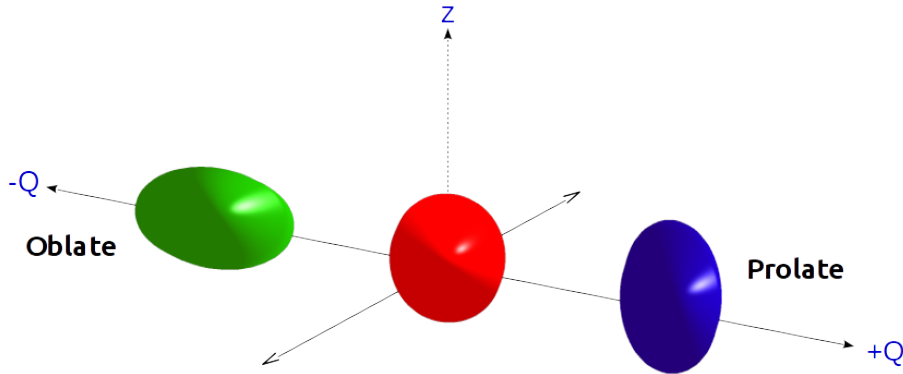


Figure 2.2: Nuclear Quadrupole deformation;  $Q > 0$  gives prolate deformation a stretched sphere with respect to the  $z$  symmetry axis.  $Q < 0$  represents oblate deformation, compressed sphere with respect to  $z$  symmetry axis.  $Q = 0$  corresponds to a spherical nucleus.

$Q_0$  is also closely linked to the  $\beta_2$  deformation parameter. Which is defined by:

$$\beta_2 = \frac{4}{3} \sqrt{\frac{\pi}{5}} \frac{\Delta R}{R_{av}}, \quad (2.5)$$

$$Q_0 = \frac{3}{\sqrt{5}\pi} Z e R_{Av}^2 \langle \beta_2 \rangle (1 + 0.36 \langle \beta_2 \rangle), \quad (2.6)$$

where  $\Delta R$  is the difference in length of the semi-minor and semi-major axis of an ellipsoid, which represents the deformed nuclear shape.  $R_{av}$  is the average nuclear radius as given by Equation 2.1.

## Rotations and Vibrations of Nuclei

In the view point of nuclear matter behaving as a deformed macroscopic system. It's a natural progression to consider how rotations and vibrations can be used to explain aspects of nuclear structure. Any classically rotating object will have an associated moment of inertia given by:

$$\xi = \sum_{i=0}^{\infty} m_i r_i^2 = \int_V \rho(\vec{r}) ||r||^2 dV. \quad (2.7)$$

Therefore, depending on the matter distribution the moment of inertia will change. The following summarises the solutions to Equation 2.7 for some example nuclear matter distributions.

$$\xi = \frac{2}{5} m R_{Av}^2 \text{ (Solid Sphere),} \quad (2.8)$$

$$\xi = \frac{2}{5} m R_{Av}^2 (1 + 0.31 \langle \beta_2 \rangle) \text{ (Solid Ellipsoid),} \quad (2.9)$$

$$\xi = \frac{9}{8\pi} m R_{Av}^2 \langle \beta_2 \rangle \text{ (Fluid Ellipsoid).} \quad (2.10)$$

As the moment of inertia is not a direct experimental observable, it's more useful to see how it contributes to the rotational energy of the system:

$$E_{\text{Rot}} = \frac{1}{2} \xi \omega^2 = \frac{1}{2} \xi \left( \frac{\ell}{\xi} \right)^2 = \frac{\hbar^2}{2\xi} I(I+1), \quad (2.11)$$

where  $I$  is the total angular momentum and  $\omega$  is the classical angular velocity, the factor  $\frac{\hbar^2}{2\xi}$  is known as the rotational energy constant,  $E_0$ , which only depends on the moment of inertia. Experimentally, it is observed that  $E_0^{\text{fluid}} > E_0^{\text{exp}} > E_0^{\text{solid}}$ , which reflects the range of the nuclear force. Its short range does not permit interactions between all nucleons, which would be reflective of a solid. On the other hand, pairing and nearest neighbour interactions means nucleons are not so weakly bonded to be completely characteristic of a pure fluid.

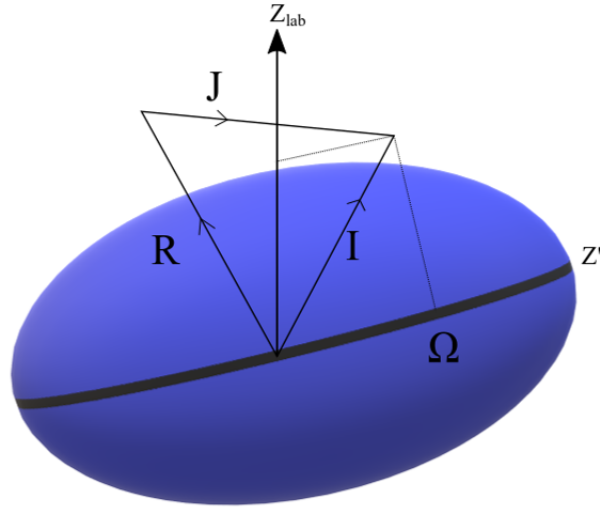


Figure 2.3: This shows how the intrinsic angular momentum ,  $J$ , and the rotational angular momentum ,  $R$ , are geometrically connected to the total angular momentum  $I$ . This also shows the relationship between the laboratory frame and the intrinsic symmetry frame of reference (Wood & Rowe, 2010).

## Rotational band theory

Another one of the most successful collective models is the rotor model. This expands on the simple description of nuclear rotations as discussed until now. This model separates its Hamiltonian into rotational and intrinsic components (Wood & Rowe, 2010):

$$\hat{H} = \hat{H}_{\text{rot}} + \hat{H}_{\text{int}}, \quad (2.12)$$

here, the rotational term is given by:

$$\hat{H}_{\text{rot}} = \frac{\hbar^2}{2} \left[ \frac{\hat{R}_{x'}^2}{\xi_{x'}} + \frac{\hat{R}_{y'}^2}{\xi_{y'}} + \frac{\hat{R}_{z'}^2}{\xi_{z'}} \right], \quad (2.13)$$

where the Euler angle coordinate system is used due to its convenience in describing rotations. As seen in Figure 2.3 the laboratory coordinate system  $(x_{\text{lab}}, y_{\text{lab}}, z_{\text{lab}})$  is now used to fix an intrinsic frame of reference  $(x', y', z')$ . Conventionally, the intrinsic frame is set by the relative angles between  $z'$  and each laboratory coordinate. In Equation 2.13,  $\xi_i$  and  $R_i$  are now the relative moment of inertia and rotational angular momentum components

with respect to the new intrinsic reference frame. The total intrinsic,  $\hat{\mathbf{J}}$ , and rotational,  $\hat{\mathbf{R}}$ , angular momentum now forms the total angular momentum,  $\hat{\mathbf{I}} = \hat{\mathbf{R}} + \hat{\mathbf{J}}$ . The projection of this vector onto the symmetry axis then gives the more appropriate quantum number  $\hat{\Omega}$ . Expressing Equation 2.13 in terms of  $\hat{\mathbf{I}}$  and  $\hat{\mathbf{J}}$  and expanding yields:

$$\hat{H} = \frac{\hbar^2}{2} \sum_i \left[ \frac{\mathbf{I}_i^2}{\xi_i} + \frac{\hat{\mathbf{I}} \cdot \hat{\mathbf{J}}}{\xi_i} \right] + \hat{H}_{int}. \quad (2.14)$$

The Hamiltonian in this form highlights that the intrinsic and rotational degrees of freedom are coupled (Wood & Rowe, 2010). This is known as the Coriolis interaction, as it increases in strength for stronger rotations.

For the case of prolate and oblate deformation, which have two fold symmetry along  $z'$ , the  $z'$  axis is then labelled as the symmetry axis. The rotational angular momentum and moment inertia is therefore also symmetrical around  $z'$ , giving  $\xi_{x'} = \xi_{y'}$  &  $R_{x'} = R_{y'}$ . With these exceptions, Equation 2.14 yields the following analytical eigenvalue solution:

$$E'_{\Omega I} = \frac{\hbar^2}{2} \left[ \frac{I(I+1)}{\xi_{x'y'}} + \left( \frac{1}{\xi_{z'}} - \frac{1}{\xi_{x'y'}} \right) \Omega^2 \right]. \quad (2.15)$$

Therefore, for even-even nuclei where the ground-state  $J^\pi = 0^+$  gives also  $\Omega = 0$ . With this, Equation 2.15 then reduces to:

$$E = E_0 + \frac{\hbar^2}{2\xi_{x'y'}} I(I+1). \quad (2.16)$$

This is equivalent to Equation 2.11, which was derived from a very simple rotor model but now with edition of the ground-state energy  $E_0$ . However, for non-zero  $\hat{\Omega}$  projections, Equation 2.15 becomes:

$$E_\alpha = E_{\alpha\Omega} + \frac{\hbar^2}{2\xi_\alpha} I(I+1). \quad (2.17)$$

Fitting to experimental data will fix  $E_{\alpha\Omega}$  and  $\xi_\alpha$  and is unique for a given band-head with a characteristic  $\hat{\Omega}$  projection. Symmetry laws play a huge role in characterising rotations. The wave function describing a simple rotor is a superposition of both  $|\Omega IM\rangle$  and  $|\Omega IM\rangle$  states, given by:

$$|\Omega IM \rangle + \epsilon(-1)^{I+\Omega} |-\Omega IM \rangle. \quad (2.18)$$

The sign of  $\epsilon$  determines if the wave function is either symmetric,  $\epsilon = +ve$ , or antisymmetric,  $\epsilon = -ve$ , via rotations about the symmetry axis. Equation 2.18 shows symmetric solutions, with  $\Omega = 0$  and odd values of  $I$  disappearing. Therefore, only even values of  $I$  are possible. This is reversed for the antisymmetric case, where only odd  $I$  value solutions survive. The  $I(I+1)$  dependence in energy together with the symmetry restrictions on  $\mathbf{I}$  form what is called a rotational band. The rotor model powerfully predicts the low energy structure of many even-even nuclei. The  $J^\pi = 0^+$  ground-state of  $^{28}\text{Si}$  is well-known to be oblately deformed (Peach et al., 2016). Therefore, a rotational band built upon this would be restricted to

$$\mathbf{I}^+ = 0^+, 2^+, 4^+, 6^+ \dots^1.$$

Another well-known rotational band in  $^{28}\text{Si}$  is the prolate deformed band built on the  $0_3^+$  state (Glatz et al., 1981a) at 6696 keV, again with the same sequence of  $I$  values as the g.s oblate band. Figure 2.4 shows the striking proportionality between excitation energy and  $I(I+1)$ , as is expected from the rotational model. The examples plotted include all of the main experimentally observed low excitation rotational bands in  $^{28}\text{Si}$ . Fitting a linear polynomial to each band and taking the gradient gives the experimentally determined rotation energy constant.

---

<sup>1</sup>As stated earlier, for  $J^\pi = 0^+$  you must have  $\Omega = 0$ , and therefore  $J^\pi = I^+$

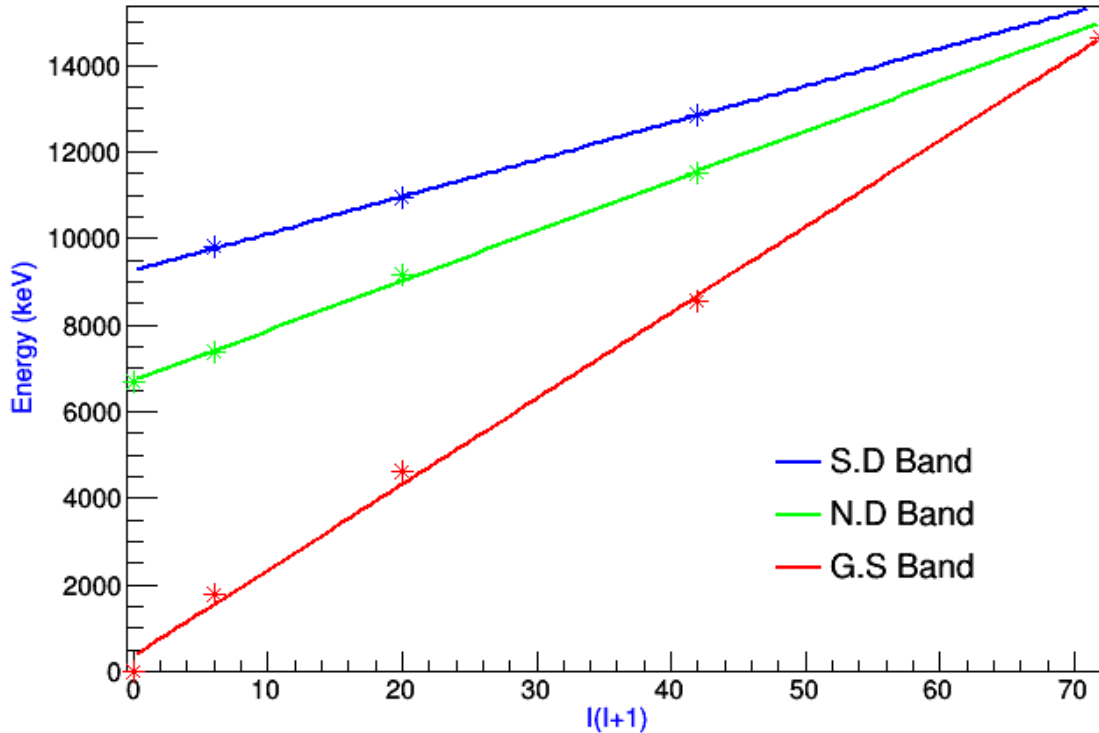


Figure 2.4:  $I(I+1)$  Energy dependence for the SD band, N.D band and g.s rotational bands in  $^{28}\text{Si}$ .

## Vibrational Bands

The vibrational model of nuclei is another very successful collective model. Here, the nucleus is described via oscillations of the nuclear matter. The complexity of the vibrations depends on the oscillations degree of freedom. A convenient formalism which characterises these oscillations is given by:

$$R(t, \theta, \phi) = \left( 1 + \sum_{\lambda \geq 1} \sum_{\mu = -\lambda}^{\lambda} \alpha_{\lambda\mu}(t) Y_{\lambda\mu}(\theta, \phi) \right). \quad (2.19)$$

$R(t, \theta, \phi)$  is now the time dependent radius of the nuclear surface at a position parameterised by the Euler angles  $\theta$  and  $\phi$ . Again,  $R_0$  is the average nuclear radius given by Equation 2.1 and  $\alpha_{\lambda\mu}$  are the expansion coefficients for each of the spherical harmonic terms,  $Y_{\lambda\mu}(\theta, \phi)$ . Here,  $\lambda$  and  $\mu$  are the quantum numbers which define the type of vi-

bration.  $\lambda = 0$ ,  $\mu = 0$  represents monopole vibrations, here the entire nuclear surface expands and contracts, known aptly as a breathing mode. For dipole vibrations,  $\lambda = 1$ . A dipole vibration with  $\mu = 0$  is simply a translation of the nucleus about its centre of mass, which will not contribute to the internal energy of the system and therefore is a forbidden excitation mode. However, for  $\mu = 1$  there is a motion around the centre of mass of two bodies. For example a distinct separation in the distribution of protons and neutrons oscillating out of phase with respect to the centre of mass. This mode is known as the giant dipole resonance. The next order vibration is the quadrupole,  $\lambda = 2$ . For the  $\mu = 2$  mode this corresponds to oscillations between prolate and oblate deformation through a spherical intermediate stage. All of these three shapes have axial symmetry and vibrations also maintain axial symmetry. These kind of vibrations are named  $\beta$ -vibrations. However, non-zero  $\lambda = 2$  components break this axial symmetry causing a degree of triaxiality. This is known as a  $\gamma$ -vibration. Octupole vibrations occur for  $\lambda = 3$ . Here, nuclei can be seen to form pear like shapes. For example  $\mu = 0$  would have the orientation of the pear flipping direction through one axis in oscillations.

## 2.2 Electromagnetic transitions

The study of electromagnetic transitions of nuclei through  $\gamma$ -ray spectroscopy has been at the forefront of nuclear structure research for more than 60 years. The development of HPGe arrays with the addition of crystal segmentation along with algorithms to improve  $\gamma$ -ray tracking capabilities have enabled spectroscopy with unparalleled combined efficiency and energy resolution. A review by Eberth and Simpson summarises the great success and milestones of  $\gamma$ -ray spectroscopy with Ge detectors over the past 60 years (Eberth & Simpson, 2008). These steady developments consistently revealed the connection between electromagnetism and deformation in nuclei.

From fundamental laws of electromagnetism, changes in magnetic fields produce electric fields and changes in electric fields produce magnetic fields. Therefore, the internal structure of nuclei is strongly linked to the type of radiation that is emitted. This high-

lights an important connection between the multipole moment, which describes the internal structure, to electromagnetic transitions. Classically, the power radiated by any electromagnetic radiation depends on the amplitude of the multipole moment  $[m(\sigma L)]$  and is given by (Krane, 1987):

$$P(\sigma L) = \frac{2(L+1)c}{\epsilon_0 L [(2L+1)!!]^2} \left( \frac{\omega}{c} \right)^{2(L+1)} [m(\sigma L)]^2, \quad (2.20)$$

where  $\sigma$  is either E or M representing electric or magnetic radiation respectively. Here,  $L$ , is the order of the multipole expansion and  $\omega$  is the angular frequency. The nucleus can not continuously radiate this power due to the restrictions of energy quantisation. In a quantum mechanical description, the quantised radiation,  $\gamma$ -decay, is a transition from an initial state  $\Psi_i$  to a final state  $\Psi_f$ . The multipole amplitude,  $m(\sigma L)$ , now has to be replaced with its operator form which changes the nucleus from its initial to its final state, i.e.

$$m_{fi}(\sigma L) = \int \psi_f^* m(\sigma L) \psi_i dv. \quad (2.21)$$

This is the matrix element of the multipole operator.  $|m(\sigma L)|^2$  in Equation 2.20 is then replaced with  $|m_{fi}(\sigma L)|^2$ . This term is known as the reduced transition probability and is typically denoted by  $B(\sigma L)$ . It is more appropriate to quantify these transitions through a decay rate instead of power radiated, as each photon carries away  $E_\gamma = \hbar\omega$  and then using the reduced transition probability, yields:

$$\lambda(\sigma L) = \frac{2(L+1)}{\epsilon_0 L [(2L+1)!!]^2 \hbar} \left( \frac{E_\gamma}{\hbar c} \right)^{2(L+1)} B(\sigma L). \quad (2.22)$$

This shows there is an energy dependence and a structural dependence to the electromagnetic decay rate. The energy dependence is restricted by the available phase space, with larger energy transitions being more favourable. The nuclear structure dependence is contained within  $B(\sigma L)$ . The degree to which the initial and final wave-functions overlap

Table 2.1: Experimental and single particle estimates for the reduced transition probability factor,  $B(\sigma L)$ . Here,  $E_\gamma$  is the  $\gamma$ -ray energy (MeV) and  $\lambda(\sigma L)$  is the experimentally determined decay constant ( $s^{-1}$ )

<b>L</b>	<b>Experimental</b>		<b>Single Particle</b>	
	$B_{\text{exp}}(\text{EL}) [e^2 \text{fm}^{2L}]$	$B_{\text{exp}}(\text{ML}) [\mu_N^2 \text{fm}^{2(L-1)}]$	$B_{\text{sp}}(\text{EL}) [e^2 \text{fm}^{2L}]$	$B_{\text{sp}}(\text{ML}) [\mu_N^2 \text{fm}^{2(L-1)}]$
<b>1</b>	$\lambda(\text{E1}) 6.289 \times 10^{-16} E_\gamma^{-3}$	$\lambda(\text{M1}) 5.688 \times 10^{-14} E_\gamma^{-3}$	$6.446 \times 10^{-2} A^{2/3}$	1.790
<b>2</b>	$\lambda(\text{E2}) 8.163 \times 10^{-10} E_\gamma^{-5}$	$\lambda(\text{M2}) 7.380 \times 10^{-8} E_\gamma^{-5}$	$5.940 \times 10^{-2} A^{4/3}$	$1.650 A^{2/3}$
<b>3</b>	$\lambda(\text{E3}) 1.752 \times 10^{-3} E_\gamma^{-9}$	$\lambda(\text{M3}) 0.158 E_\gamma^{-7}$	$5.940 \times 10^{-2} A^2$	$1.650 A^{4/3}$
<b>4</b>	$\lambda(\text{E4}) 5.893 \times 10^3 E_\gamma^{-11}$	$\lambda(\text{M4}) 5.330 \times 10^5 E_\gamma^{-9}$	$6.285 \times 10^{-2} A^{8/3}$	$1.746 A^2$

will depend on the quantum numbers which define each state. In particular their total angular momentum ( $J$ ), parity ( $\pi$ ) and isospin projection ( $T_z$ ).

Inserting the values for each multipole order,  $L$ , in Equation 2.22 and rearranging for  $B(\sigma L)$  gives the experimentally determined reduced transition probability. These are listed in Table 2.1 in their reduced forms, here  $\lambda(\sigma L)$  is the experimentally determined decay constant, which can be calculated from half life measurements. The most important information contained in the reduced transition probabilities is the degree of collectivity. This is determined by calculating the theoretical  $B(\sigma L)$  values from a single particle transition. The magnetic,  $\hat{M}_L$  and electric,  $\hat{Q}_L$ , multipole operators are well-known for these single particle de-excitations (Weisskopf, 1951). These depend on the spherical harmonics,  $Y_\ell^m(\theta, \phi)$ , radius and nuclear magnetic  $g$  factor. Applying the relevant single particle magnetic operators to Equation 2.21 yields:

$$B(EL) = \frac{1}{2J_i + 1} \left| \langle \psi_f | \hat{Q}_L | \psi_i \rangle \right|^2, \quad (2.23)$$

$$B(ML) = \frac{1}{2J_i + 1} \left| \langle \psi_f | \hat{M}_L | \psi_i \rangle \right|^2, \quad (2.24)$$

Table 2.1 shows the single particle estimates in their reduced forms for each multipole order,  $L$ . These estimates only depend on the mass number,  $A$ , of the nucleus.

Taking the ratio:

$$B(\sigma L) = \frac{B_{\text{exp}}(\sigma L)}{B_{\text{sp}}(\sigma L)}, \quad (2.25)$$

gives the transition strength in Weisskopf units (*W.u.*). Therefore a transition strength of,  $B(\sigma L) \approx 1$  *W.u.* suggest only a single or very few nucleons contribute to the transition. A  $B(\sigma L) \gg 1$  *W.u.* then suggests large collectivity with many nucleons contributing to the transition, or even the entire nucleus through rotation or vibration.

## 2.3 Reaction Theory

Essential to any nuclear physics experiment is a complete understanding of the reaction mechanisms involved between the incident projectile and target nuclei. The main two classifications are direct and compound. These are distinguished by the interaction time scales of the reacting nuclei. The widths of the observed structures in the excitation spectrum, for example in a high resolution spectrometer is then related to the states lifetime via the uncertainty principle:

$$\Delta E \Delta t \geq \frac{\hbar}{2}. \quad (2.26)$$

The timescale,  $\Delta t$ , is the combination of the transit time of the projectile through the target nucleus and the time taken to rearrange any constituent nucleons within the target nucleus. If there is a strong wavefunction overlap between the initial and final exit channel then the interaction may only involve very few nucleons. If the interaction timescale is on the order of the transit time of the projectile through the target, then this is considered a direct reaction. However, a more strict definition involves the number of degrees of freedom of motion. For example if a nucleus excites through a purely rotational state or vibration located at the surface. This involves few degrees of freedom and is considered direct. In terms of experimental observables, you would expect a forward focused, anisotropic ejectile angular distribution due to the small angular momentum transfer. For

compound reactions you expect the opposite, as the large interaction timescale allows multiple interactions within the nucleus. Therefore, we expect a statistical and isotropic response in the angular distribution as thermal equilibrium is achieved.

Traditionally, compound reactions such as fusion evaporation have been used to study SD in heavier nuclei (Lopez-Martens et al., 2016). Figure 2.5 shows how different structures are formed. The compound nucleus is produced in a high spin and high energy state within the entry distribution. Several light nuclei are then ejected from the hot nucleus as it tries to reach thermal equilibrium. Most of the time the nucleus cool to the N.D bands following the yrast line. However, it's possible to get trapped in the second minimum, forming an SD band.

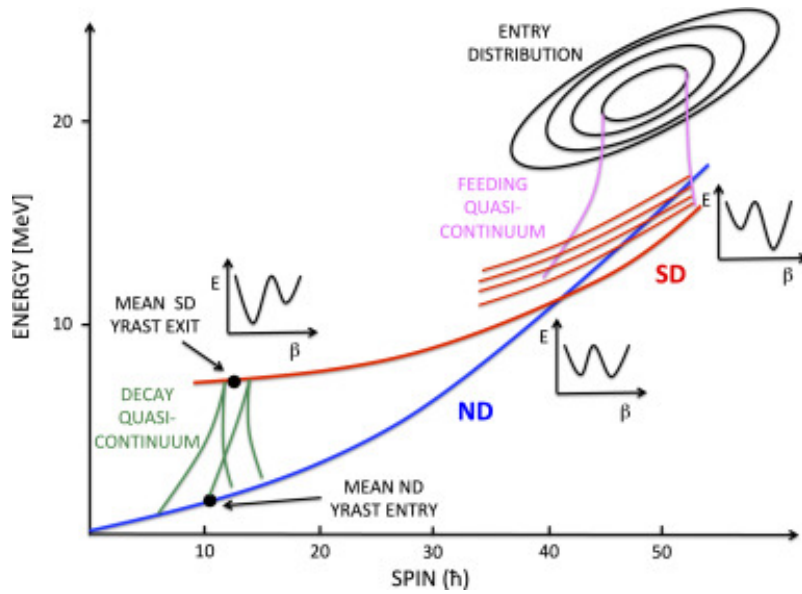


Figure 2.5: Traditional method of populating SD bands in heavy nuclei using compound nuclear reactions. Here, compound nuclei are formed with high energy and spin within the entry distribution and are either trapped inside a second minimum forming a SD band or cool straight to the N.D band (Lopez-Martens et al., 2016) .

Inelastic scattering is a prime example of a direct reaction, for example  $^{28}\text{Si}(\alpha, \alpha')^{28}\text{Si}^*$ . The many-body problem of the two interacting nuclei is very difficult to solve directly.

The optical model reduces this complex problem by using an effective interacting potential:

$$V = I + iW, \quad (2.27)$$

where  $I$  is the real component of the potential and  $W$  is the imaginary. In the plane wave description of elastic scattering, the flux of the incoming plane wave and outgoing spherical wave is conserved. Solving the Schrödinger with only the real part, yields the well-known Rutherford scattering cross section. However, for inelastic processes, flux has to be attenuated from the elastic channel. This is achieved by the introduction of the imaginary term,  $W$ , known as an optical potential. The wavefunction produced from solving the Schrödinger equation with the optical potential can be used as a starting point for more complicated calculations such as the Distorted-Wave Born Approximation (DWBA) approach.

The DWBA approach introduces distortion in the waves of the nuclear + Coulomb field to increase accuracy. The distorted potentials are normally forced to fit experimental elastic cross sections. Codes such as DWUCK4 (zero-range) and DWUCK5 (finite range) are widely used to solve such problems. The DWBA approach assumes a direct excitation for inelastic processes. If there are multiple channels with connecting transitions then the coupled-channel Born approximation should be used. Codes such as Chuck3 can solve a set of coupled-channel equations and calculate differential cross sections for direct and multi-step excitation.

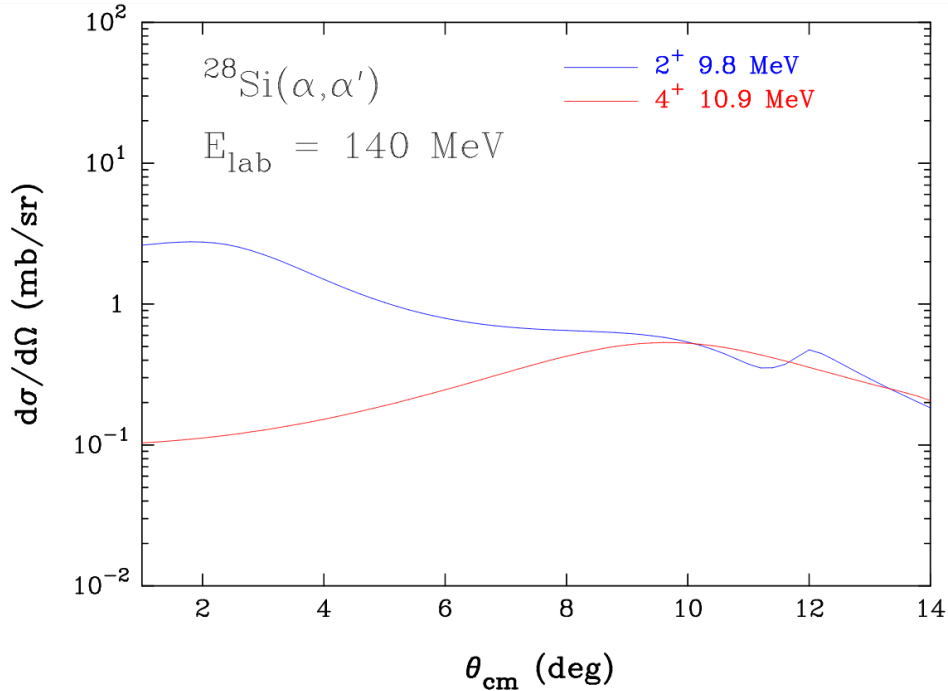


Figure 2.6: DWBA calculations for a  $J^\pi = 2^+$  and  $J^\pi = 4^+$  state produced through alpha inelastic scattering, with  $E_{\text{lab}} = 140$  MeV. The differential cross section is maximum around  $10^\circ$ .

The differential cross section for the excitation of  $^{28}\text{Si}$  to the 10944.0-keV  $J^\pi=4^+$  state was calculated with the DWBA approach. Figure 2.6 shows the results for this calculation, with a maximum in the cross section around  $10^\circ$ . However, Grand Raiden was set to an angle of  $9.1^\circ$  due to physical restrictions of the GRAF mode set-up at RCNP. Generally, low spin populations should peak at smaller scattering angles. Hence why this method preferentially populates low spin states. The reaction chosen also preferentially populates natural parity states. Through conservation of spin:

$$I_f = I_\alpha + I_{^{28}\text{Si}} + \ell = 0 + 0 + \ell, \quad (2.28)$$

therefore  $I_f = \ell$ . Then by conservation of parity,

$$\pi_f = \pi_\alpha \pi_{^{28}\text{Si}} (-1)^\ell = \pi^+ \pi^+ (-1)^\ell, \quad (2.29)$$

therefore,  $\pi_f = (-1)^\ell$ . This constrains the possible states to be populated to  $0^+$ ,  $1^-$ ,  $2^+$ ,  $3^-$  and  $4^+$  etc. These are known as natural parity states and so other states populated are therefore called unnatural parity states and will be significantly suppressed.

The beam energy was chosen to ensure direct reactions. At high beam energies single-step excitation is dominant (Tamii et al., 2009). Direct reactions are primarily surface reactions, particularly with inelastic scattering. This then strongly populates collective degrees of freedom, such as rotations and vibrations. All these properties made inelastic scattering of 130s-MeV  $\alpha$  particles at  $9.1^\circ$  to be the best choice for probing SD bands in  $^{28}\text{Si}$ .

## 2.4 Angular Correlations

The spatial distribution of  $\gamma$ -decay can not always be assumed to be isotropic. The angular dependence of  $\gamma$ -decay depends on the initial and final magnetic substate (m-state) of the transition. If no preference for the m-state population exists or no particular nuclear orientation is established, then the summation over all possible angular distributions will be isotropic. However, strong applied magnetic fields, nuclear reactions and the measurement of the angle between a  $\gamma$ -decay with respect to another in a cascade can all lead to anisotropic angular distributions.

Strong magnetic fields can cause an unequal m-state population if cooled to extremely low temperatures. Here, a significant population can preserve its nuclear orientation. At higher temperature, thermal motion will break the orientation. The distribution of thermal energies are then as described by the Boltzmann distribution. This technique requires special conditions and was not feasible during this experiment.

Measuring relative angles between cascade  $\gamma$ -decays is known as angular correlation,  $W(\theta, \Delta m_\ell)$ .

$$W(\theta, 0) = \frac{3}{8\pi} \sin^2\theta, \quad (2.30)$$

$$W(\theta, 1) = \frac{3}{16\pi} (1 + \cos^2\theta), \quad (2.31)$$

$$W(\theta, -1) = \frac{3}{16\pi} (1 + \cos^2\theta), \quad (2.32)$$

where,  $\theta$  is the angle between the two cascade  $\gamma$ -decays and  $\Delta m_\ell$  is the change in magnetic substate. For example, a cascade decay from an unpolarised target with  $J_i = 0 \rightarrow J_f = 1$  via an intermediate  $J = 1$  state will have this effect. The first dipole transition

has to transfer one unit of angular momentum  $m_i = 0 \rightarrow m_f = \pm 1$  as  $m_i = 0 \rightarrow m_f = 0$  is forbidden. Therefore a  $(1 + \cos^2\theta)$  distribution will be observed relative to the first decay. In general the distributions follows the sum of Legendre polynomials which are a function of the multipolarity,  $\ell_1$  and  $\ell_2$  of the two photons of the form:

$$W(\theta, \ell_1, \ell_2) = 1 + A_2 \cos^2 + A_4 \cos^4 + A_6 \cos^6 \dots + A_{2L} \cos^{2L} \theta, \quad (2.33)$$

where the experimental  $a_{2L}$  fitted coefficients can be compared to calculated values which depend on  $\ell_1$  &  $\ell_2$ .

The third method is through nuclear reactions and measuring particle- $\gamma$  angular correlations. More specifically for this research,  $\alpha$ - $\gamma$  angular correlations between the scattered  $\alpha$ -particle and subsequent  $\gamma$ -decay from the excited  $^{28}\text{Si}$  nucleus. One major simplification to the problem occurs for  $\alpha$  scattering at  $0^\circ$  or  $180^\circ$ . This is known as the Litherland and Ferguson method II (Ferguson, 1974). As the reaction plane is defined by  $\hat{\mathbf{L}} = \hat{\mathbf{r}} \wedge \hat{\mathbf{p}}$ , then as  $\hat{\mathbf{p}}$  remains parallel to the beam axis,  $\hat{\mathbf{p}}_z$  and by definition  $\hat{\mathbf{L}}_z = 0$ . This constrains the possible m-state population to:

$$m_{\max} = I_{\text{Si}} + s_\alpha + s_{\alpha'}, \quad (2.34)$$

as  $I_{\text{Si}}$  and  $s_\alpha = 0$  then  $m_{\max} = s_{\alpha'}$  and the angular distribution becomes:

$$W(\theta) = \sum_{\kappa} A''_{\kappa} Q_{\kappa} P_{\kappa}(\cos\theta). \quad (2.35)$$

This is the superposition of all possible m-states.  $P_{\kappa}$  is again the associated Legendre polynomials.  $Q_{\kappa}$  is the attenuation coefficients which account for finite opening angles of the clover detectors. Then the  $A''_{\kappa}$  coefficients are analysed the same as in Equation 2.33.

When the projectile is no longer scattered parallel or anti-parallel to the beam axis then Litherland and Ferguson method II no longer holds. This requires more sophisticated methods and requires computation.

Angcor is the only code that has been specifically created to calculate  $\alpha$ - $\gamma$  angular correlations for all projectile scattering angles. As an input this code requires the m-state

population distribution. This is one of the outputs of the DWBA Chuck3 program as discussed previously. The angular distribution can only be evaluated over one azimuthal plane e.g. the reaction plane. There is also a symmetry in the angular distribution around the reaction plane.

The spin and parities of the initial, intermediate and final states of the reaction process was also needed for the *angcor* inputs. Information on the type  $\gamma$ -transition also had to be included, particularly its energy and multipolarity with mixing ratio,  $\delta$ . These parameters will then define a unique angular distribution.

This allows the experimentally observed states spin and parity to be confirmed. This technique is very useful for the CAGRA campaign as many of the spin and parity assignments of  $^{28}\text{Si}$  at and above 10 MeV remain tentative.

# Chapter 3

## Experimental Set-up

### 3.1 CAGRA Project

The CAGRA project (**C**lover **A**rray **G**amma-ray spectrometer at **R**CNP for **A**dvanced **R**esearch) was a diverse and multipurpose campaign, which contained experiments to explore both nuclear structure and nuclear astrophysics. Its main aim was to combine the high energy resolution of HPGe clover type detectors in coincidence with a high resolution spectrometer. These were also complimented by the addition of LaBr<sub>3</sub> scintillator detectors, of which offer increased efficiency and fast timing over their HPGe counterparts. This unique combination of detector systems allowed for new and exciting nuclear physics to be explored.

The CAGRA campaign was a global collaboration, which included contributions from many, universities, research labs and government institutes. Of the 12 clover detectors used in the campaign; Argonne National Laboratory (**ANL**) contributed 8, the US Army (**ARL**) supplied 2 and the institute of Modern Physics (**IMP**) gave 2. The 4 LaBr<sub>3</sub> detectors used were from INFN sezione di Milano. The DAQ for the CAGRA array was brought over from **ANL**. The rest of the equipment was supplied by the home facility, **R**esearch **C**entre for **N**uclear **P**hysics (**RCNP**).

## 3.2 RCNP Facility

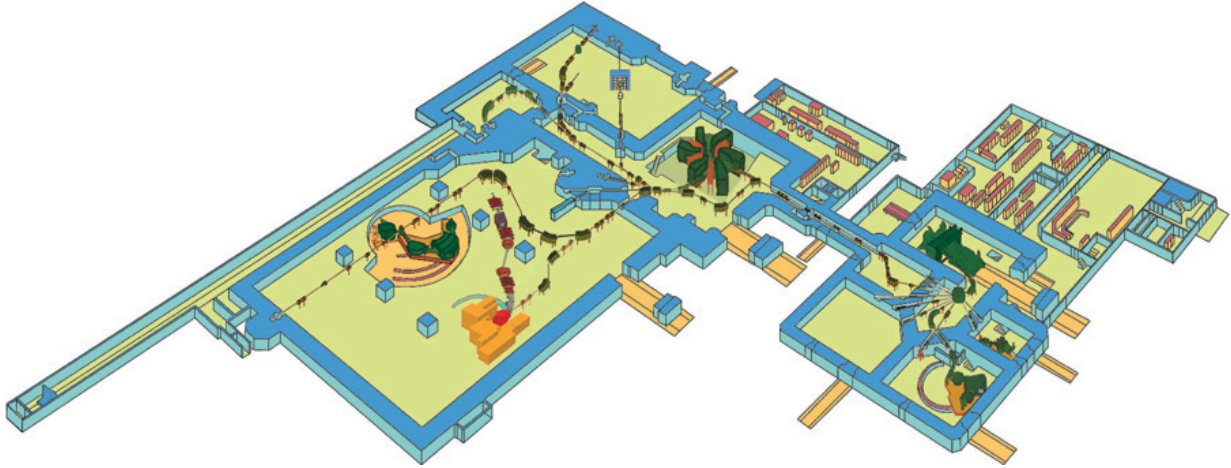


Figure 3.1: Birdseye view of the RCNP facility, in particular the location of the AVF cyclotron and Grand Raiden.

The RCNP facility as shown in Figure 3.1 is a diverse research facility for nuclear and particle physics. The facility has two particle accelerators; the Ring and azimuthal varying field (AVF) cyclotrons. This twin accelerator system is connected to multiple beam lines with dedicated detector systems. Of main interest here is the West Hall, which is where Grand Raiden and CAGRA was situated.

## 3.3 Accelerator Capabilities

The AVF and RING cascade cyclotron system was used in the CAGRA campaign. The AVF is predominately used as an injector system for the RING cyclotron. However, for low beam energies, the AVF can be used as a dedicated accelerator. For this research, the AVF accelerated  $\alpha$  particles to the required total kinetic energy of 130 MeV.

### K140 AVF cyclotron

This accelerator was commissioned in 1973 and uses the Azimuthally-Varying-Field (**AVF**) design. Key to any successful cyclotron is the isochronism condition. Here, the time

period of an ion must be independent of the path length taken. The ion frequency,  $\omega_{rev}$ , is determined by:

$$\omega_{rev} = \frac{q B_0}{m_0}, \quad (3.1)$$

where  $B_0$  is the magnetic field strength of the cyclotron,  $m_0$  and  $q$  is the mass and charge respectively of the ion. Therefore, for a fixed magnetic field strength and ion frequency, the time period is constant. An alternating electric field is applied to the ions to achieve acceleration. This field is typically in the order of MHz. This is within the radio frequency range of the electromagnetic spectrum and is the origin of the name given to the field applied, known as the **RF**. Clearly, the RF applied,  $\omega_{RF}$ , has to be in phase with the intrinsic ion frequency or else the ion will not be coherently accelerated. i.e  $\omega_{RF} = h \omega_{rev}$ , where  $h$  is the cyclotron harmonics. This is known as the synchronous condition.

If the speed of the ion becomes relativistic, then the mass in Equation 3.1 needs to be scaled by  $\gamma$ , which is dependant on the velocity of the ion. This will break the isochronism and synchronous condition and to overcome this, either the RF or magnetic field has to dynamically change. The AVF achieves this by having a magnetic field gradient to account for the changing relativistic mass. Hence, the name Azimuthally-Varying-Field. For the RCNP AVF cyclotron, the typical magnetic field strength is 1.6 T and has 1 or 3 cyclotron harmonics available. The chosen harmonic was  $h = 3$ , this is equivalent to two beam bunches per RF cycle. The RF frequency was 12.4 MHz, therefore the beam bunch interval was 80.65 ns.

During this research, the average beam current of  $\alpha$  particles on target produced by the AVF was around 3 enA.

### 3.4 Grand Raiden Spectrometer

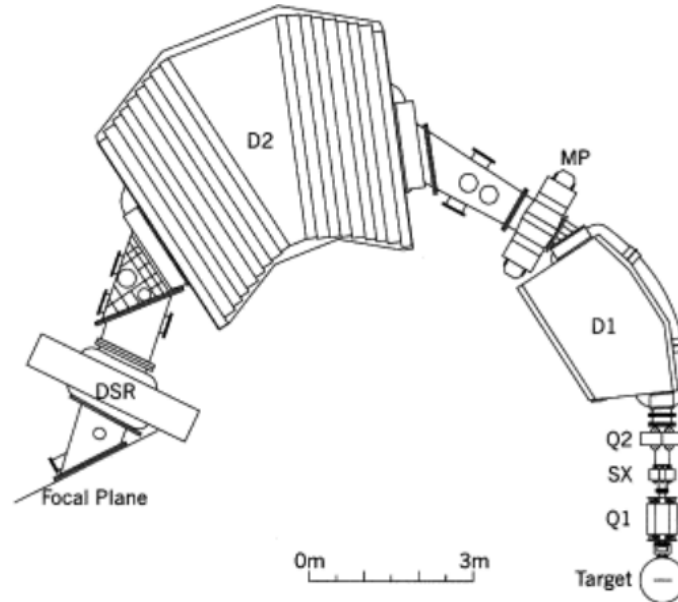


Figure 3.2: Birdseye view of Grand Raiden Spectrometer. Highlighting relative position of ion optics and target position.

Grand Raiden is a high-resolution magnetic spectrometer. These devices have made significant impact on nuclear spectroscopy. Excitation functions of many reactions and nuclei have been studied through these devices. Their main advantage over other detectors is the ability to maintain high precision, even at high excitation energy. As level density increases with excitation energy, high resolving power is required to resolve states in these regions. Resolving power can be quantified as the ratio of momentum over momentum spread,  $\frac{p}{\Delta p}$ . Grand Raiden has achieved a resolving power of  $40 \times 10^3$ . This was achieved with a 300-MeV proton beam, via  $^{168}\text{Er}(p,p')$  inelastic scattering. The resolving power for 130-MeV  $\alpha$  particles via  $^{28}\text{Si}(\alpha, \alpha')$  inelastic scattering in this experiment was lower. This was due to the lower beam energy and lighter mass of the target. The recoil momentum of  $^{28}\text{Si}$  is much more significant than  $^{168}\text{Er}$  also the thick,  $11 \text{ mg/cm}^2$ ,  $^{\text{nat}}\text{Si}$  target and lower beam energy will increase energy losses and increase momentum spread even before reaching the spectrometer.

Table 3.1: Specifications of Grand Raiden

Specifications	Value
Ion Optics Configuration	QSQDMDD
Horizontal Acceptance Angle	$\pm 20$ mr
Vertical Acceptance Angle	$\pm 60$ mr
Resolving Power $p/\Delta p$	37,076
Focal Plane Tilting	$45^\circ$
Deflection Angle	$162^\circ$
Magnetic Rigidity (Max)	$54 T \cdot m$
Vertical Magnification	5.98
Horizontal Magnification	-0.417

The fundamental operation of spectrometers is underpinned by the Lorentz force:

$$\vec{\mathbf{F}} = q \cdot \vec{\mathbf{E}} + q \vec{\mathbf{V}} \times \vec{\mathbf{B}}. \quad (3.2)$$

The momentum of an ion after interaction with the target, for example through inelastic scattering, needs to be conserved as this is how the excitation energy is reconstructed. From Equation 3.2, from the cross product, the force applied from a magnetic field is always perpendicular to the ions velocity/momentum. Most spectrometers employ only linear magnetic fields, to conserve momentum. There are spectrometers that use both electric and magnetic fields. However, these fields are more complex and can't be linear if momentum is to be conserved. With no Electric field, Equation 3.2 becomes  $\vec{\mathbf{F}} = q \vec{\mathbf{V}} \times \vec{\mathbf{B}}$ . Equating to the centripetal force and rearranging yields:

$$\frac{\vec{\mathbf{P}}}{q} = \vec{\mathbf{B}} \rho, \quad (3.3)$$

this is known as the magnetic rigidity. It becomes clear here that for a fixed ion of charge,  $q$ , and fixed magnetic field strength,  $B$ , the only degrees of freedom are momentum,  $\vec{\mathbf{P}}$ , and the radius of curvature,  $\rho$ , which the ion is deflected through by. i.e. the greater the momentum the larger the radius of curvature becomes, and vice versa. In Figure 3.2,  $B$  represents the magnetic field strength of the dipole magnets labelled D1 and D2. For  $^{28}\text{Si}(\alpha, \alpha')$  inelastic scattering, the more energy the  $\alpha$  particle loses during this interaction

the greater the excitation energy in  $^{28}\text{Si}$ . The momentum distribution depends on which excited states are populated and the momentum then governs the radius of curvature of the  $\alpha$  particle passing through Grand Raiden. The focal plane at the end of GR as seen in Figure 3.2 precisely tracks the positions and angles of the ions passing through it. The degree of precision of all these characteristics then determine the overall resolving power of the high resolution spectrometer.

## Ion-optics

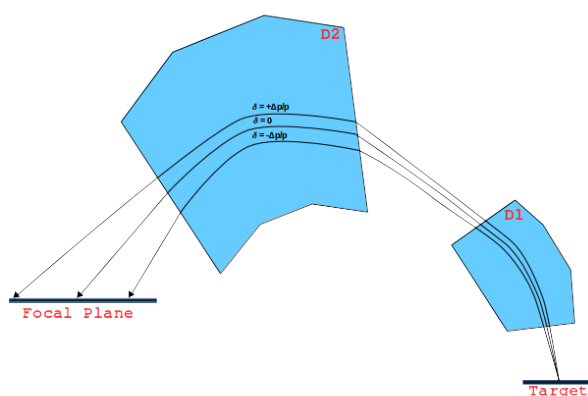


Figure 3.3: Illustration for ion-optics with no dispersion matching.

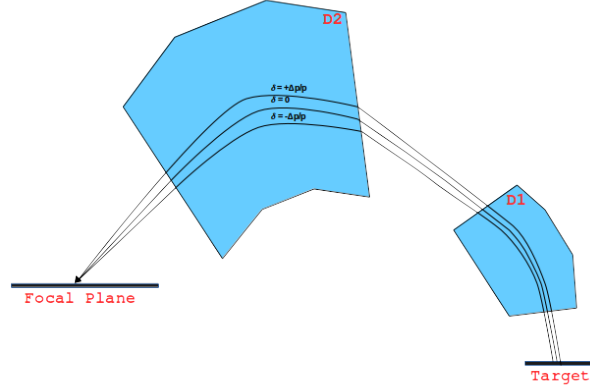


Figure 3.4: Ion-optics for spatial dispersion matching condition.

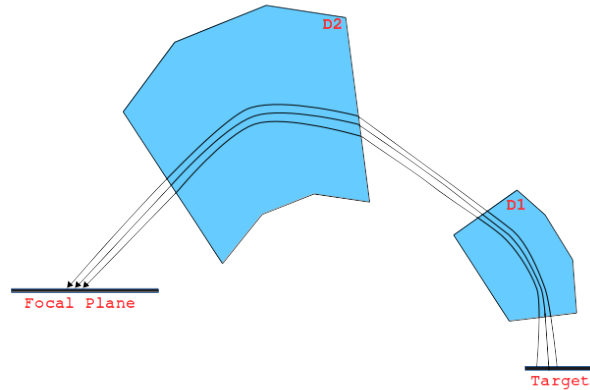


Figure 3.5: Ion-optics for angular and spatial dispersion matching condition.

Each ion optical apparatus will contribute a change in phase space of the beam. The easiest way to represent and track these changes is through matrix representation:

$$\mathfrak{R}_{final} = R_N \cdot R_{N-1} \cdot \dots \cdot R_0 \cdot \mathfrak{R}_{initial}, \quad (3.4)$$

where  $\mathfrak{R}$ , is a function of all the essential parameters to describe the phase space of the beam. i.e  $\mathfrak{R}(x, y, \theta, \phi, \vec{P})$ . All of the initial starting point parameters of the beam are contained in  $\mathfrak{R}_{initial}$ . Each matrix element in Equation 3.4,  $R_N$ , represents the effect of one

magnet on the current phase space. They are sequentially applied until the final phase space  $R_{\text{final}}$  is determined, this is known as a Transfer Map. A code named ORBIT was used to calculate the Transfer Map and to obtain the ion-optical properties of GR. Kinematics of the scattered ions at the target position can be reconstructed and a significant improvement in resolution can be achieved if the ion optics of the entire beam line and spectrometer is set-up correctly. This requires the beam line optics (pre-target) to be matched with the spectrometer (post-target). This is known as Dispersion matching.

Dispersion occurs when the ion deviates from its central expected orbit by amount  $\delta$ , as is calculated from the Transfer map. The initial momentum and spatial distribution will have a natural spread, these deviations will then perturbate through the ion optics, deteriorating resolution and smearing out any angular information that could be used for the kinematic reconstruction, Figure 3.3 illustrates this effect. If these,  $\delta$ , dispersions at the target position are not accounted for then significant spatial and angular deviations will occur within GR, as can be seen magnified at the focal plane. Figure 3.4 shows how choosing the right ion optics before the target to spatially separate depending on the scale of  $\delta$  removes this effect at the focal plane. More so, if the angular dispersions are accounted for before the target, as can be seen in Figure 3.5, then the angular deviations at the focal plane can also be removed. For GR, the ion optics is designed so that the horizontal entrance angle to the focal plane,  $\theta_{FP}$ , is proportional the horizontal scattering angle at the target position,  $\theta_{tg}$ . The y position on the focal plane is directly proportional the vertical scattering angle at the target position,  $\phi_{tg}$ . This would not be achievable without angular and spatial dispersion matching.

Higher order solutions to the Transfer map via a Taylor expansion gives what are known as aberrations. Solving the Transfer map for these higher order terms will reveal what the correlation between state parameters are. For example in Table 3.2 ( $x|\theta^3$ ) quantifies the third order correlation between  $\theta$  and  $x$ . These correlations are essential in explaining the kinematic distributions seen in the focal plane. As will be discussed further in Chapter 4.4.

## GRAF Mode

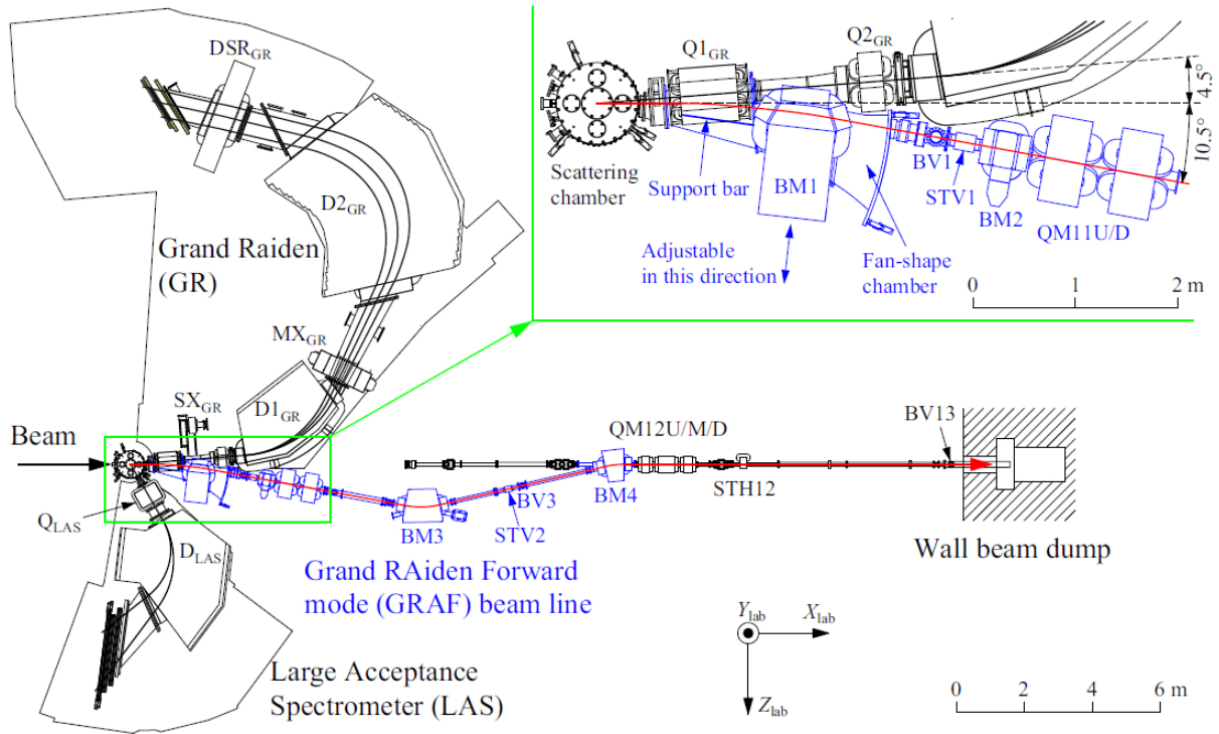


Figure 3.6: Layout of GRAF mode at RCNP.

In the standard configuration of Grand Raiden, a Faraday cup and beam stop is positioned 2 m downstream from the target, where CAGRA is located, as seen in Figure 3.6. Therefore, the Bremsstrahlung,  $\gamma$ -rays and neutrons produced at the beam stop would not reach CAGRA and contribute to an increased background. The neutrons produced would have also damaged the clover detectors, deteriorating resolution throughout the campaign. As can be seen in Figure 3.6, the beam dump in GRAF mode was moved 7 m downstream.

Table 3.2: Ion-Optics calculations from multiple programs (Terashima, 2018)

Ion Property	Orbit	Orbit (2 <sup>nd</sup> order)	GICOSY	GICOSY (3 <sup>rd</sup> order)	Q2	SX Removed
$\langle x x \rangle$	-0.4167	-0.4164	-0.4178	-0.4171	-0.4761	-0.4761
$\langle x \theta \rangle$	0	0	$1 \times 10^{-3}$	0	$1 \times 10^{-3}$	$1 \times 10^{-3}$
$\langle x \delta \rangle$	15.45	15.453	15.451	15.451	15.451	15.451
$\langle y y \rangle$	5.98	5.98	6.13	6.13	6.18	6.18
$\langle y \phi \rangle$	$-1.66 \times 10^{-3}$	$-4.77 \times 10^{-3}$	$1 \times 10^{-3}$	$1 \times 10^{-3}$	$2 \times 10^{-2}$	$2 \times 10^{-2}$
$\langle x \theta\theta \rangle$	$-1.74 \times 10^{-3}$	0	$5.9 \times 10^{-2}$	$5.4 \times 10^{-2}$	0.28	5.95
$\langle x \phi\phi \rangle$	0	$3.8 \times 10^{-3}$	$1.5 \times 10^{-2}$	$1.5 \times 10^{-2}$	$2.8 \times 10^{-3}$	-0.524
$\langle x x\theta \rangle$	-0.25	-0.244	-0.24	-0.24	0.14	7.91
$\langle x \theta\delta \rangle$	37.078	37.094	36.7	36.7	36.71	36.71
$\langle x \delta\delta \rangle$			-9.52	-9.52	-9.52	-9.52
$\langle x \theta\theta\theta \rangle$	-2.79	87.83	90.54	-3.25	0.811	3.6
$\langle x \theta\phi\phi \rangle$	0.026	4.5	6.14	1.05	1.68	-10.42
$\langle x \theta\theta\delta \rangle$	1.093	161.2	162.8	4.79	1.84	47.5
$\langle x \theta\delta\delta \rangle$	-0.045	-19.94	-18.9	1.12	-0.33	-0.33
$\langle x \phi\phi\delta \rangle$	10.65	10.64	10.64	10.39	10.49	4.83
$\langle x \delta\delta\delta \rangle$			34.25	60.26	60.26	60.26
$\Theta_x$	44.98°	44.98°	44.86°	44.86°	45.02°	45.02°
$\Theta_y$	65.3°	65.45°	68.5°	68.5°	67.97°	74.06°

Figure 3.2 shows the configuration of the focusing magnets, summarised as QSQDMDD. The quadrupole magnets, Q, focus the beam only in one plane and defocus in the other. The sextupole magnet, S, should be there to mitigate any dispersions and to remove  $(x|\phi^2)$  aberrations. However, in GRAF mode the sextupole magnets had to be removed because of space restrictions; this had consequences in the ability to reconstruct the kinematics of the inelastic scattering, see Chapter 4.4.

## Focal Plane Detectors

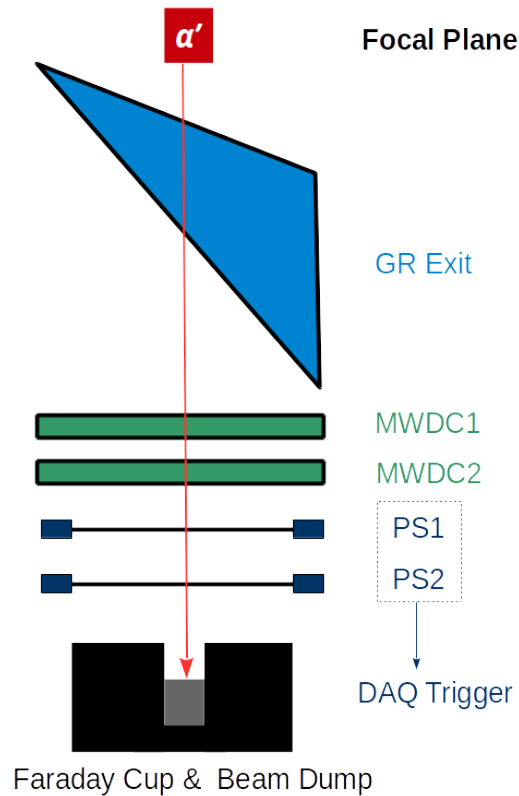


Figure 3.7: Schematic view of the Grand Raiden focal plane detectors.

The focal plane detectors track precisely the position of  $\alpha$  particles and from this, the angle can be reconstructed. As can be seen in Figure 3.7, the particles pass through two Multiwire Drift Chambers, labelled MWDC1 and MWDC2. The  $\alpha$  particles then pass through two plastic scintillator detectors, labelled PS1 and PS2. A coincidence between the PS1 and PS2 is required to trigger the DAQ and considered to be a true event. The elastically scattered  $\alpha$  particles are focused onto the Faraday Cup and beam dump, located at the very end of the beam line.

## MWDC

The multiwire chamber is a gas filled detector, here a mixture of argon (70%) and isobutane (30%) was used. The gas is ionised as the  $\alpha$  particles pass through, leaving an ion track. The subsequent ion pairs that are formed are then collected via an applied electric field. Two Cathode plates on either side of the MWDC apply negative bias of -5.9 keV, which collect the positive ions. The electrons produced from the ionisation are attracted to the anodes. The anode wires are made up of two planes. Each plane is made up of two types of wires, sense and potential wires. The readout signals are taken from the sense wires. The potential wires and sense wires are normally grounded to achieve a uniform electric field. However, the potential wires were biased to -0.3 keV. This strengthens the electric field around the sense wires and therefore increases their efficiency. However, this worsens spatial resolution, as the uniform field is disturbed. The X plane wires, as seen in Figure 3.8, are vertically aligned, with one in every three anode wires being a grounded sense wire. The U plane wires are inclined at  $48.2^\circ$ , here every one in two anode wires are sense wires. In its basic application, depending on which wires are triggered, gives an approximate trajectory. However, its spatial resolution can not be finer than the wire spacing.

To achieve position resolution finer than the wire spacing, the time interval between the wire signal and the PS1 trigger is measured. A LeCroy 2735DC board was used as a preamplifier and discriminator for all of the wires in the four planes. These signals were used as the starting trigger of a LeCroy 337 Time to Digital Converter (TDC) with the PS1 trigger being its stopping signal. This time difference represents the drift time of the electrons to the anodes. A track's trajectory will then have a set of unique timing distributions. These distributions are passed through look-up tables that convert from drift time to drift distance. These distances then precisely trace out the  $\alpha$  particles trajectory to achieve sub wire spatial resolution and also gives the angle in which it entered the focal plane.

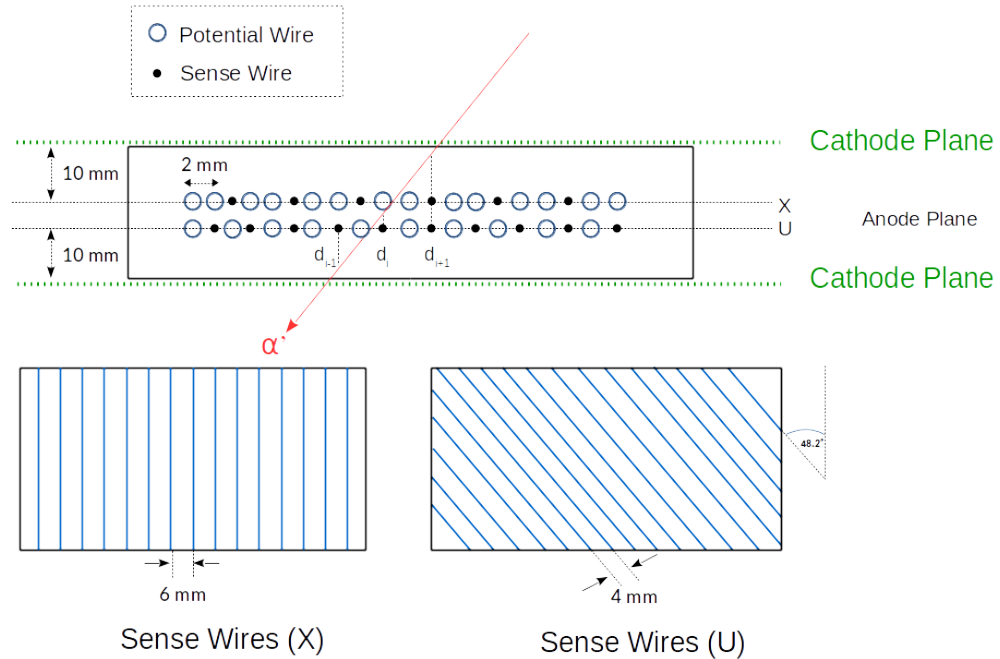


Figure 3.8: Overview of the MWDC configuration of sense and anode wires relative to the cathode plane. Lower figure is of the layout of the sense wires, X plane (left) and U plane (right).

### 3.5 CAGRA Array

The CAGRA array contains 12 HPGe detectors and 4 LaBr<sub>3</sub> scintillators. The HPGe detectors are of the clover type. Figure 3.10 shows the typical design of these detectors showing the 4 isolated HPGe crystals, which all share one cryostat. Each clover was reversed biased as detailed in Table 3.3. Before explaining the advantages of this design, it's important to describe the ways in which  $\gamma$ -rays interact with matter.

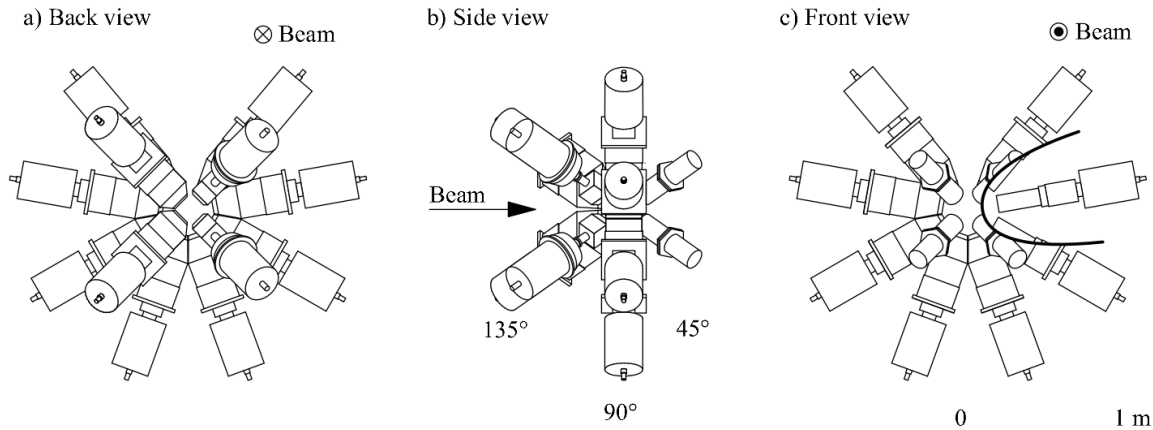


Figure 3.9: (left) Upstream view of CAGRA. (middle) Side view showing the three distinct lab angles  $45^\circ$ ,  $90^\circ$  and  $135^\circ$  of the clover and  $\text{LaBr}_3$  detectors with respect to the beam axis. (right) shows a front view, downstream of the beam.

## Interaction of $\gamma$ rays with matter

There are three distinct interactions of  $\gamma$  rays with matter, photoelectric effect, Compton scattering and pair production. For the photoelectric effect, due to conservation of momentum, a free electron can't absorb a  $\gamma$  ray. However, a bound electron to an atom can then share the momentum with the entire atom. Once absorbed the electron is ejected from

Table 3.3: Summary of CAGRA positions, HV values and shielding used.

Slot	Detector	Angle	Distance to target (cm)	Bias Voltage (V)	Shielding
1.	$\text{LaBr}_3$	$45^\circ$	16	-950	10 mm (Pb) + 4 mm (Cu)
2.	$\text{LaBr}_3$	$45^\circ$	16	-810	10 mm (Pb) + 4 mm (Cu)
3.	$\text{LaBr}_3$	$45^\circ$	16	-970	10 mm (Pb) + 4 mm (Cu)
4.	$\text{LaBr}_3$	$45^\circ$	16	-814	10 mm (Pb) + 4 mm (Cu)
5.	ANL clover	$90^\circ$	20.8	+3000	2 mm (Pb) + 2 mm (Cu)
6.	ANL clover	$90^\circ$	20.8	+3000	2 mm (Pb) + 2 mm (Cu)
7.	ANL clover	$90^\circ$	20.8	+3500	2 mm (Pb) + 2 mm (Cu)
8.	ANL clover	$90^\circ$	20.8	+3000	2 mm (Pb) + 2 mm (Cu)
9.	ANL clover	$90^\circ$	20.8	+2500	2 mm (Pb) + 2 mm (Cu)
10.	ANL clover	$90^\circ$	20.8	+3500	2 mm (Pb) + 2 mm (Cu)
11.	ANL clover	$90^\circ$	20.8	+3000	2 mm (Pb) + 2 mm (Cu)
12.	ANL clover	$90^\circ$	20.8	+4000	2 mm (Pb) + 2 mm (Cu)
13.	ARL clover	$135^\circ$	20.8	+3500	2 mm (Pb) + 2 mm (Cu)
14.	ARL clover	$135^\circ$	20.8	+3000	2 mm (Pb) + 2 mm (Cu)
15.	IMP clover	$135^\circ$	20.8	+3500	4 mm (Pb) + 2 mm (Cu)
16.	IMP clover	$135^\circ$	20.8	+3500	4 mm (Pb) + 2 mm (Cu)

the atom with kinetic energy  $E_k = h\nu - E_b$ . With  $E_b$  being the binding energy of the electron and  $\nu$  being the frequency of the  $\gamma$ -ray. It is this energy which is then absorbed by the detector material, the electron loses energy in the following ways: Collisional energy losses arise from the electromagnetic interaction of the electron with the material, this interaction can ionise or excite the atoms in the material. This is the dominating energy loss process for low energy electrons. There is also a possibility for electron nuclear scattering and at low energies this is determined by the Rutherford cross section. Another energy loss mechanism is due to Bremsstrahlung, here any ion which decelerates emits radiation. However, for electrons in Ge, the energy in which this process will become dominant is for electrons of kinetic energy above 14.1 MeV and can be neglected below 1 MeV.

Another way  $\gamma$ -rays interact with matter is Compton scattering. Here, instead of the  $\gamma$ -ray being absorbed it is scattered. The amount of energy lost depends on the scattering angle, and is maximum at  $180^\circ$ . The kinetic energy lost by the  $\gamma$ -ray is given to the recoiled electron, and this energy is deposited in the crystal. Compton scattering dominates for intermediate  $\gamma$ -ray energies.

If the energy of the  $\gamma$ -ray is above twice the rest mass energy of an electron, then pair production is possible. Here, the energy of the  $\gamma$  ray is converted into creating an electron-positron pair. Any surplus energy above 1.022 MeV is shared between the electron-positron pair. The electron-positron pair then deposit their energy into the crystal, until they come to rest. The positron then will annihilate with another electron and emit two 511-keV  $\gamma$ -rays. If both of these  $\gamma$  rays are absorbed the full energy is detected. If both  $\gamma$  rays escape then this is known as double escape. When only one of them are detected this is known as single escape. Pair production dominates for higher energies. With these three interactions, only photoelectric interactions deposits full energy. The other two processes require multiple interactions before full energy deposition. The clover detector was therefore designed to mitigate the losses from these two processes and increase full energy efficiency.

As shown in Figure 3.10, Cu and Pb shielding was placed in front of each clover detector, their thicknesses are detailed in Table 3.3. These were used to stop low energy x-rays and

Bremsstrahlung being detected, reducing low energy noise and decreasing the trigger rates. Pb is used as it has a high density and is relatively cheap absorber material. However, Pb can itself produce x-rays and so an extra layer of Cu is added to absorb these secondaries.

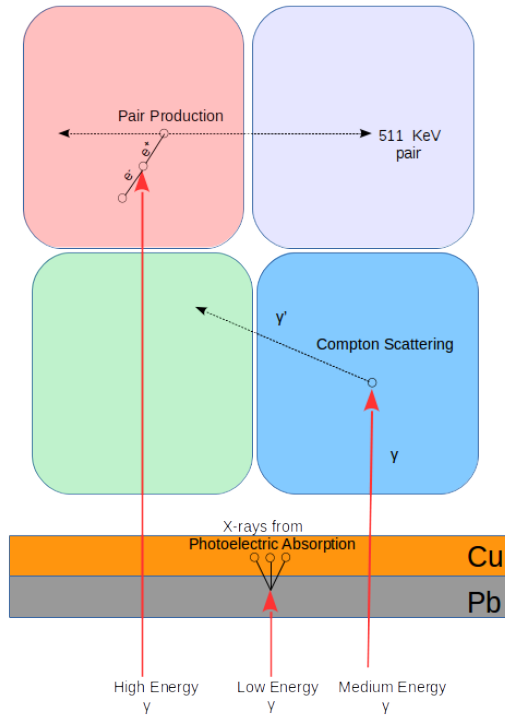


Figure 3.10: Layout of a typical clover detector with the different interactions possible, also showing the layout of the Pb and Cu shielding.

## Addback

Addback is one of the ways to increase full energy photo peak efficiency. This is achieved by summing the energy of adjacent crystals. This can be between crystals of the same or even different clovers. For example, in the interactions detailed in Figure 3.10 the Compton scattered  $\gamma$ -rays could deposit a fraction of its full energy in one crystal, then go on to undergo further Compton scattering or photoelectric absorption. Another example could be though pair production, here the two 511-keV annihilation  $\gamma$ -rays could be detected in two opposite crystals. In all these cases the energy is shared between multiple crystals. Therefore, if the energy can be summed, the full energy can be recovered. The reliability

of this technique is dependent on the multiplicity of the event, i.e. the number of crystals that are triggered per event. This itself can be dependent on the background rate, noise thresholds and  $\gamma$  yields of the reaction being studied. Increased crystal multiplicities will make it more difficult to distinguish between these different type of events. To ensure that events are truly correlated the time difference between triggered crystals can be taken. Only events within a pre-set time window will be then summed over energy. However, this technique requires sufficient time resolution for it to be effective.

## BGO suppression

When Compton scattering occurs and the scattered  $\gamma$ -ray escapes the array, this results in an incomplete energy deposition. To reduce this effect and improve the full energy to background ratio, BGO suppression can be implemented. Here, the clover detectors are surrounded by BGO (Bismuth Germanate) scintillators. BGO has a large combined Z and density, which yields a high intrinsic detection efficiency for  $\gamma$ -rays. Now, a Compton scattered  $\gamma$ -ray has a high probability of interacting within the BGO detector after it escapes the clover HPGe crystals. If a signal in any crystal is promptly followed by an adjacent BGO, the event can be vetoed, as this will be seen as an incomplete energy deposition. BGO suppression suffers the same issues as described in the description of addback, requiring sufficient time resolution and low event multiplicities. For this set-up all clover detectors had BGO suppression capabilities except for the IMP Clovers in slots 15 and 16.

## LaBr<sub>3</sub>

Lanthanum bromide doped with cerium, LaBr<sub>3</sub>(Ce), is an inorganic scintillator and holds some significant advantages over HPGe semiconductor detectors. Their increased efficiency and exceptional time resolution, has allowed for new exciting research. In particular, for particle- $\gamma$  coincidence techniques, such as the STELLA campaign. This is part of the UK FATIMA collaboration, based at the Andromède facility in Orsay, which aims to measure

the  $^{12}\text{C} + ^{12}\text{C}$  fusion cross section below the Coulomb barrier. Mixing  $\text{LaBr}_3$  and HPGe detectors is also becoming a popular technique. For example at TRIUMF, where they combined DANTE, a  $\text{LaBr}_3/\text{BaF}_2$  scintillator array with GRIFFIN containing 16 HPGe clover detectors. Here, the performance of  $\gamma$ - $\gamma$  coincidence techniques can be improved by combining the unique advantages of each detector type.

Both particle- $\gamma$  and  $\gamma$ - $\gamma$  techniques aim to reduce background contribution to measurements and simultaneously tag events to reduce likelihood of chance coincidence. The rate of random coincidence,  $R$ , is given by:

$$R = 2\tau r_1 r_2, \quad (3.5)$$

where  $\tau$ , is the time window between the two events and  $r_1$  and  $r_2$  are the rates of the two uncorrelated decay quanta. Therefore, the random coincidence rate can be reduced by decreasing  $\tau$ . The fast timing from  $\text{LaBr}_3$  improves time resolution and therefore allows for smaller time windows to be achieved. In the CAGRA array, therefore coincidence events between two  $\text{LaBr}_3$  detectors would give the best time resolution, however at cost of energy resolution. It can be favourable then to use  $\text{LaBr}_3$  as an initial tag, then to look at events in the clover detectors for high resolution spectroscopy.

The original design of CAGRA consisted only of clover detectors. However, the forward angle detectors at  $45^\circ$  were changed to  $\text{LaBr}_3$  scintillator detectors. The estimated background from Bremsstrahlung and neutrons was expected to be too high for the HPGe detectors in these positions.

The differential cross section for Rutherford scattering is highest at forward angles, for 130-MeV  $\alpha$ -particle scattering from  $^{28}\text{Si}$  at  $45^\circ$ , approximately 10 MeV of kinetic energy is lost. The stopping distance for 120-MeV  $\alpha$  particles in aluminium is approximately 35 mm. The Aluminium target chamber was only 3 mm thick, therefore the scattered particles will pass through and be implanted into the shielding in front of the  $\text{LaBr}_3$  detectors. Therefore thicker Pb and Cu shielding was needed to absorb the low energy x-rays and bremsstrahlung produced and to make sure  $\alpha$  particles did not reach the detectors.

### 3.6 Digital Acquisition

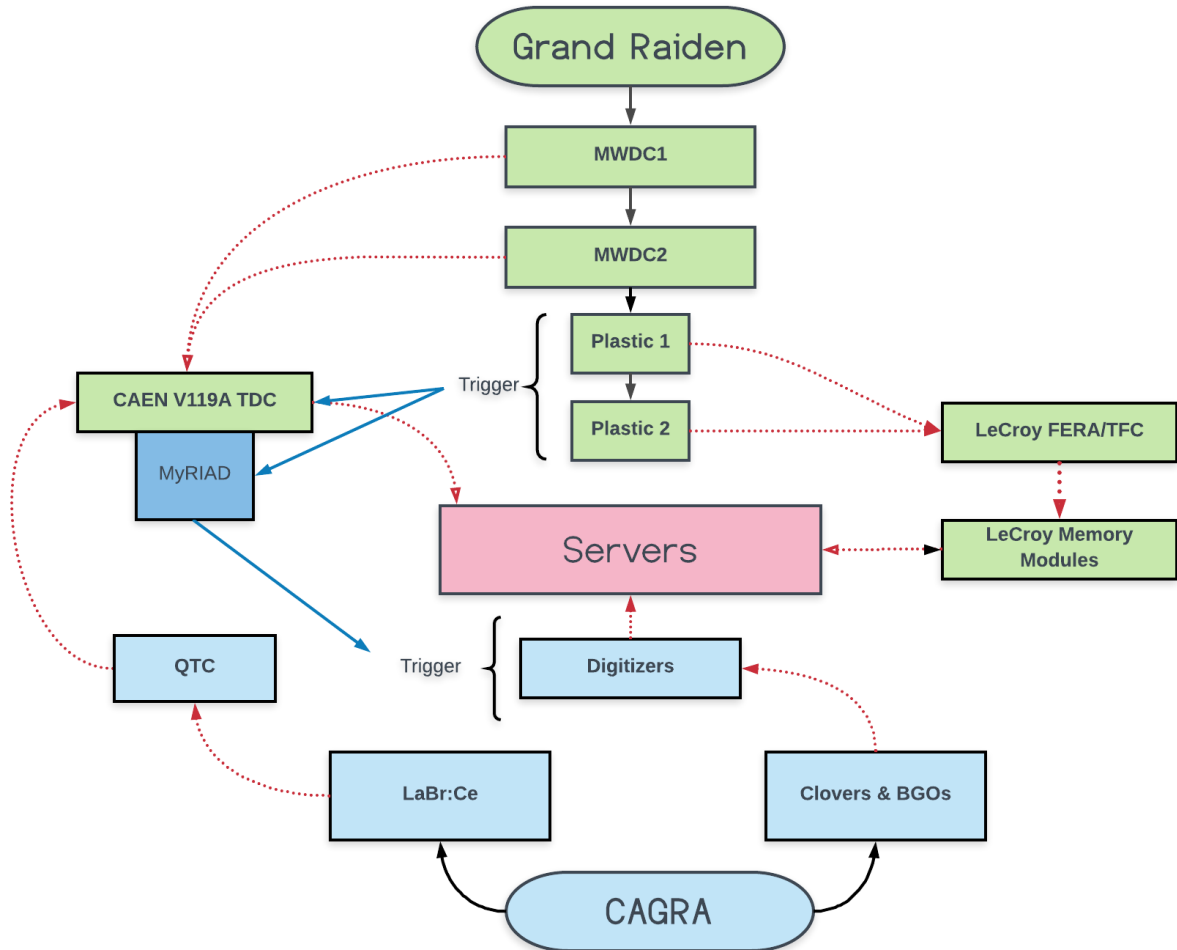


Figure 3.11: Flow Chart of the Data acquisition set-up for CAGRA and GR, black lines show connections to detectors, red dotted lines show the signals from detectors to acquisition hardware and blue lines show the direction of trigger signals.

The merging of three separate detector systems, Grand Raiden, Clovers and LaBr<sub>3</sub> was very challenging. Figure 3.11 shows the complexity of the electronic set-up in a flow diagram. The green boxes represent focal plane electronics which was in situ. The timing for the MWDC's was taken using CAEN V119A TDC's triggered by coincident plastic 1 and plastic 2 hits. The signal and timing from the plastic detectors were recorded using LeCroy FERA/TFC modules. CAGRA electronics are represented in blue. The digitizers

and trigger modules were originally developed for GRETINA with the firmware and DAQ repackaged from Gammasphere. This was achieved through the clover-share collaboration. MyRIAD was also added to the GR-DAQ. This made a common timestamp between both CAGRA and GR to synchronise the two set-ups. It also distributed the trigger from the plastic detectors to the CAGRA digitizers. Therefore, CAGRA only took data when in coincidence with the two plastic detectors. The GR readout was totally independent of CAGRA. This meant Raw focal plane data could be separately analysed. The GR set-up used trigger counters to reconstruct MWDC and scintillator events.

### 3.7 CAGRA Data Analysis

The GR-analyzer was the event processing and analysis framework developed by RCNP using the PAW analysis software. The CAGRA data was processed using the GRUTinzer analysis framework developed at NSCL. The raw events were time ordered via a data thread from GRUTinzer. The building loop then time-correlated events between GR and CAGRA. The next step was to unpack the data, transforming binary time to c++ objects, which made offline and online analysis more convenient. Since GRUTinzer is built on top of the ROOT data analysis framework, histograms and tree data could be filled both online and offline. It also has an extensive library of utilities built over many campaigns at ANL and NSCL. These include relativistic kinematics calculators, Doppler correction and peak fitting routines. However, some issues did arise with joining separately analysed runs together when utilising multi-threading capabilities. The hadd functionality in ROOT was not compatible with the GRUTinzer data types. Therefore this script had to be re-written for this purpose to join tree and histogram data from multiple analysed run files.

# Chapter 4

## Grand Raiden Corrections

This chapter focuses on the necessary steps to transform the raw focal plane data taken at RCNP into a high resolution excitation energy spectrum of  $^{28}\text{Si}$ . The time of flight (ToF) of  $\alpha$  particles from the AVF cyclotron to the focal plane is also an important parameter, as this is used for particle identification (PID). The PID is essential to ensuring background reduction in the excitation spectrum. The main sources of spectrometer background include re-scattered  $\alpha$  particles from the walls of the spectrometer and deuterons, in which have the same  $A/q$  ratio as  $\alpha$  particles.

### 4.1 VDC Drift Time Corrections

The multi-hit TDC as shown in Figure 3.11 records the time difference between each sense wire signal and plastic scintillator trigger. The fastest events from the multi-hit TDC from each sense wire was then recorded. The distribution of drift times as seen in Figure 4.1 have a characteristic feature that high TDC values, corresponding to shorter drift times are more probable. This is an artefact due to  $\alpha$  particles passing through the chamber near to the anode wires, in particular at less than the critical distance for a Townsend Avalanche to occur. As the drift velocity is accelerated in this region the drift time is therefore shortened. The Drift times recorded by the TDC are inverted, as it was operated

in common stop mode. Signals produced from tracks originating from the avalanche region thus have longer time periods to wait before the stop signal from the plastic detectors. This is with respect to signals originating in the uniform electric field region, where drift velocities are slower and therefore have less time to wait before the common stop.

The drift time distributions were then converted to a drift length distribution. The drift length is the distance between the track and the cathode plate in the MWDC, therefore will be between 0 to 10 mm as illustrated in Figure 3.8 and following convention they have been normalised between 0 and 1.

This was achieved by building a conversion look-up table between drift time and drift distance. The final spatial distribution should be uniform as the MWDC is designed that all distances are equally probable. To ensure a successful conversion, typically a White Spectrum is used, here there should be no dominant peaks or continuous background that can bias the calibration.  $^{28}\text{Si}$  run data was used as it met these requirements. Figure 4.2(left) shows the drift-length distribution for each wire plane before passing through the look-up table and Figure 4.2(right) is after. The particle trajectory is reconstructed from all of the drift distances, and thus more reliable after the calibration.

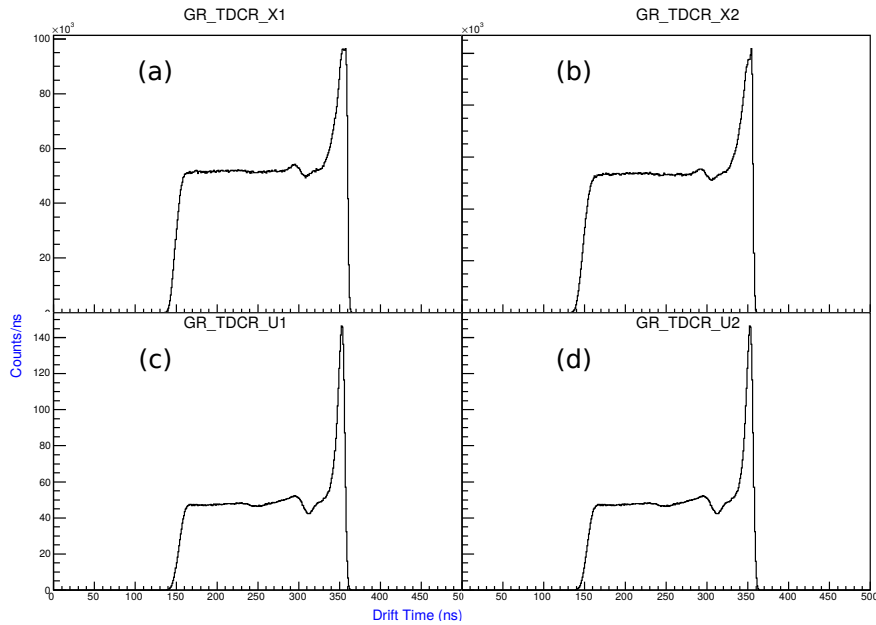


Figure 4.1: Time distributions between each of the 4 wire planes and the plastic detectors. They show the characteristic feature that higher TDC values, corresponding to shorter drift times are more probable.

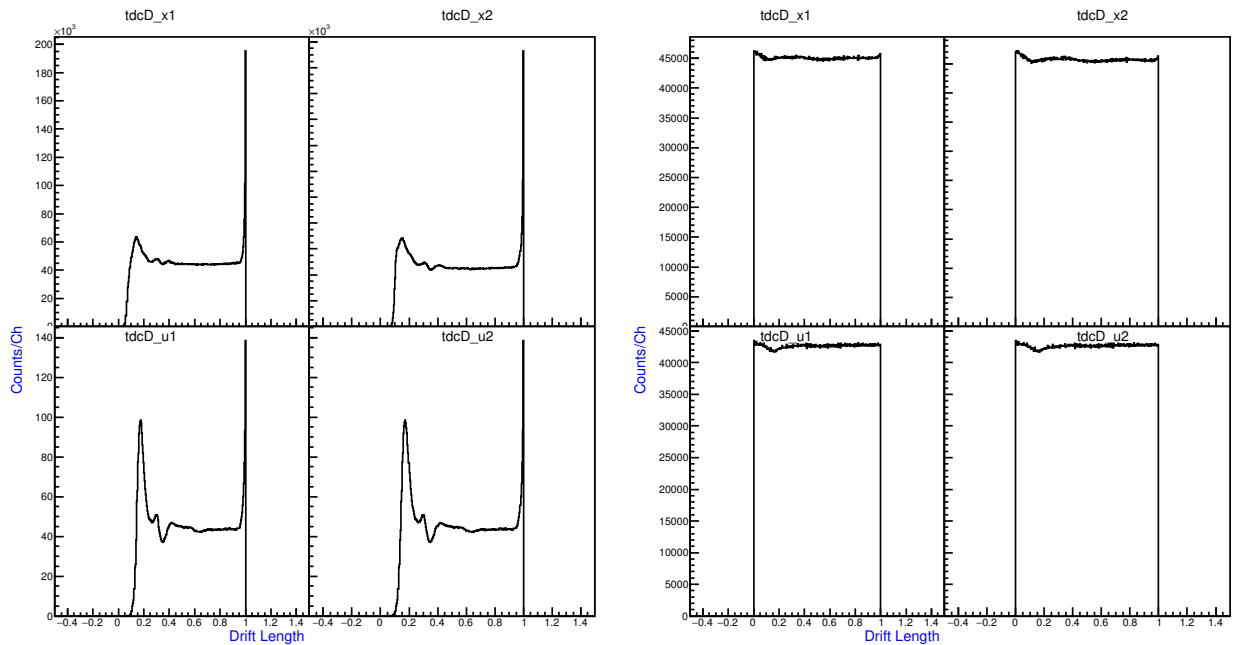


Figure 4.2: Converted drift time to drift length for each wire plane. All drift distances have been normalised between 0 to 1. The left figures show before the calibration, right figures showing the expected flat distribution after the calibration.

## 4.2 Time of Flight Corrections

The time of flight of the  $\alpha$  particles through GR should be independent of the horizontal, X, position and the horizontal entrance angle to the focal plane, Th. However, as described in the previous chapter ion-optical aberrations cause correlations between these parameters. It was important to correct for these correlations to improve the ToF distribution resolution, as it is needed for PID and LaBr<sub>3</sub> fast timing.

The Th correlation with ToF is illustrated in Figure 4.3(a), the right insert shows the projection onto the ToF axis. The ToF distribution is very broad with a FWHM of  $11.426 \pm 0.002$  ns. The Th dependence was fitted by placing a gate around the strongest distribution (state) as highlighted in red. The left insert here shows the average ToF as a function of Th taken from this gate. A linear function was then fitted to this profile yielding;  $\text{ToF}_{\text{th}}^{\text{fit}} = 538.006 - (1667.79\text{Th})$  (ns). The Th dependence was removed by an arbitrary alignment:

$$\text{ToF}_{\text{th}} = \text{ToF}_{\text{raw}}(\text{ns}) - \text{ToF}_{\text{th}}^{\text{fit}} + 400. \quad (4.1)$$

Figure 4.3(c) shows  $\text{ToF}_{\text{th}}$  Vs Th, here you can see clearly the Th correlation has been removed and each Th distribution is now independent of ToF. Then the X dependence on  $\text{ToF}_{\text{th}}$  was plotted in Figure 4.3(b), here a linear dependence is clearly visible. Again a graphical gate was placed around the main distribution as seen in red. The insert in this figure is the average  $\text{ToF}_{\text{th}}$  as a function of X position on the focal plane within this gate. A linear fit to this profile yielded;  $\text{ToF}_{\text{th}}^{\text{fit}} = 430.571 + (0.167\text{X})$ . Then the X dependence was removed by a second arbitrary alignment:

$$\text{ToF}_{\text{corr}} = \text{ToF}_{\text{th}} - \text{ToF}_{\text{X}}^{\text{fit}} + 400(\text{ns}). \quad (4.2)$$

Plotting  $\text{ToF}_{\text{corr}}$  against X in Figure 4.3(d) demonstrates these two parameters are no longer correlated. The insert in this figure again shows the projection onto the ToF axis, the ToF distribution is now narrower. After the removal of both TH and X correlations the ToF peak FWHM was reduced to  $2.192 \pm 0.001$  ns.

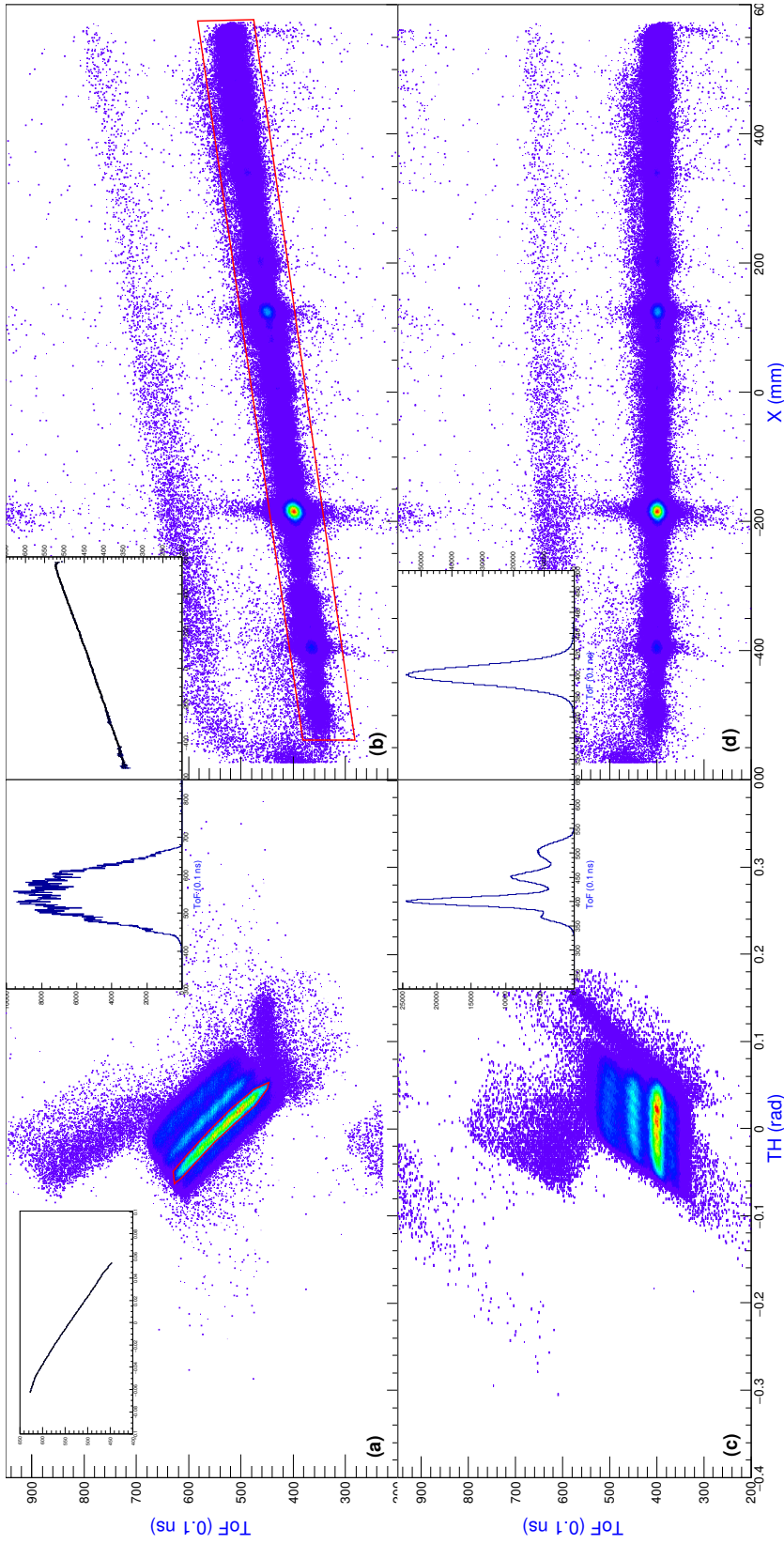


Figure 4.3: (a) ToF Vs Theta (horizontal entrance angle to focal plane), showing a clear correlation. Insert (1a) is the projection onto the time of flight axis showing a broad distribution. The left insert is the average ToF(Theta) which was linearly fitted. (c) Shows the corrected time of flight distribution, now independent of Th. The insert is the new corrected ToF projection, the peaks are due to a correlation with X. (b) This figure more clearly shows the ToF correlation with the X position on the focal plane. The insert here is the average ToF (corrected on Th) as a function of X, then linearly fitted. (d) Overall ToF corrected with removed Th and X correlations. The insert now shows a much finer ToF resolution.

### 4.3 Particle Identification

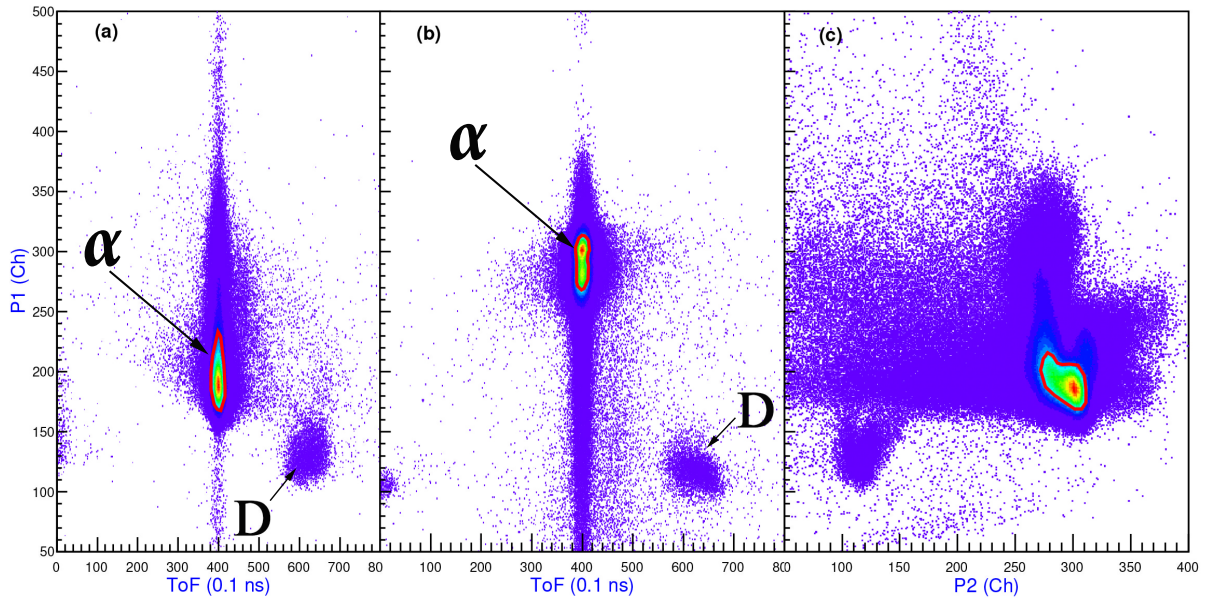


Figure 4.4: (a) Plastic 1 energy Vs ToF. (b) Plastic 2 energy Vs ToF and (c) Plastic 1 energy Vs Plastic 2 energy. The 3 main lobes are from the inelastic scattered  $\alpha$ -particles, labelled  $\alpha$ . The secondary lobes are caused by deuteron contamination, labelled D.

The corrected ToF can now be used for particle identification. The correlation between the energy loss in each plastic detectors and the corrected ToF can be seen in Figure 4.4(a) and (b) respectively. These show the importance of the ToF corrections, as the broad uncorrected ToF distributions would give a poor and unresolved particle ID plot.

The main lobes in these plots represent the  $\alpha$  particles, with the secondary lobe produced from deuterons. The separation is caused from two main factors. The larger stopping power of  $\alpha$  particles compared to deuterons in plastic leads to more energy lost by  $\alpha$  particles. Their ToF is separated due to differences in their momentum distributions and magnetic rigidity. The deuterons have larger radius of curvature within GR, therefore increasing its ToF.

The three graphical gates shown in red was then applied for all of the following analysis, to ensure deuterons and re-scattered  $\alpha$  particles were removed, along with any other background.

## 4.4 Kinematic Corrections

The next stage of the focal plane corrections was to remove the Th dependence from the X position of the focal plane. Figure 4.5(a) shows the correlation of these two parameters, in which a bowing effect is evident. This was an issue as the projection of this plot onto the X position axis represents the excitation energy of  $^{28}\text{Si}$ . Here, the bowing will cause states to overlap and so they can not be resolved, resulting in a poor resolution.

To remove this dependence a graphical cut was placed around the resolved states in the Th Vs X plot. The insert in Figure 4.5(a) shows the average X position as a function of Th for one example state at  $-200$  mm. Here, the correlation between Th and X is even more evident. A second order polynomial was fitted to this profile. Higher order polynomials did yield improved fits to this profile. However, when applied to the rest of the data, large deviations occurred, in particular at the extremities of Th. Therefore, the order of the polynomials used was kept low to reduce the number of turning points. This was repeated for all of the graphical cuts as shown in Figure 4.5.

There was a significant deviation of the polynomial coefficients as a function of X. Therefore it was not possible to have one correction for the entire range of the focal plane and so a multidimensional fit was required. The results of the multidimensional fit are as shown in Table 4.1. Again the order of this fit was kept low to reduce the number of turning points. Figure 4.5(b) shows the results of the TH Vs X plot with the multidimensional fit corrections applied, in which the bowing effect was removed.

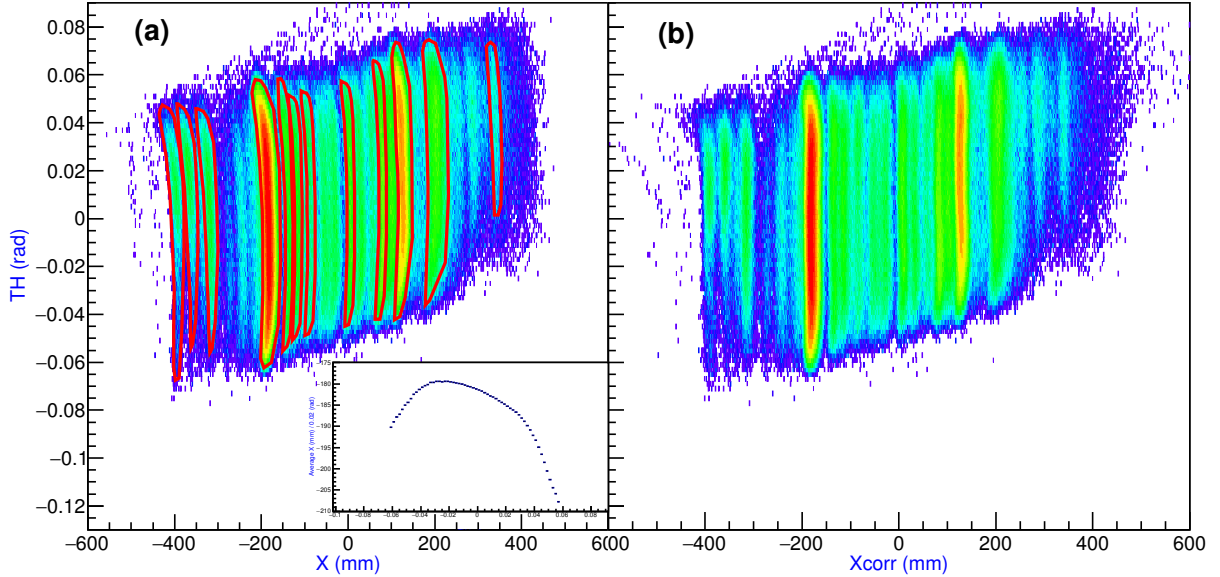


Figure 4.5: (a) TH scattering angle Vs X position of the focal plane detectors with a clear correlation, as seen in the insert. (b) The correlation was removed by making several gates on distinct states and creating a multidimensional fit.

## 4.5 Excitation Spectrum

With all of the necessary focal-plane corrections complete, it was then possible to plot the corrected X position of the focal plane with the following steps applied:

- VDC drift time to drift length calibration.
- ToF-corrected particle ID gates.
- Th dependence removed from X position.

The final focal-plane spectrum with all these corrections applied is as shown in Figure 4.6. To achieve energy calibration of this spectrum the excitation energy of known states

Table 4.1: Multidimensional fit for kinematic corrections

Coefficient	$X^0$	$X^1$	$X^2$	$X^3$	$X^4$
a	0.98	0.9971			
b	-9.58419	0.902	0.000629	-3.36e-6	-7.43e-9
c	-3904.629	-7.158	-0.0554	3.53e-4	1.52e-6

need to be used. The assignment of states to these peaks was not possible until coincidence data between CAGRA and GR was applied which will be discussed in Chapter 5. This was to ensure the correct states were assigned by using  $\gamma$ -spectroscopy and comparing to the well documented adopted level schemes.

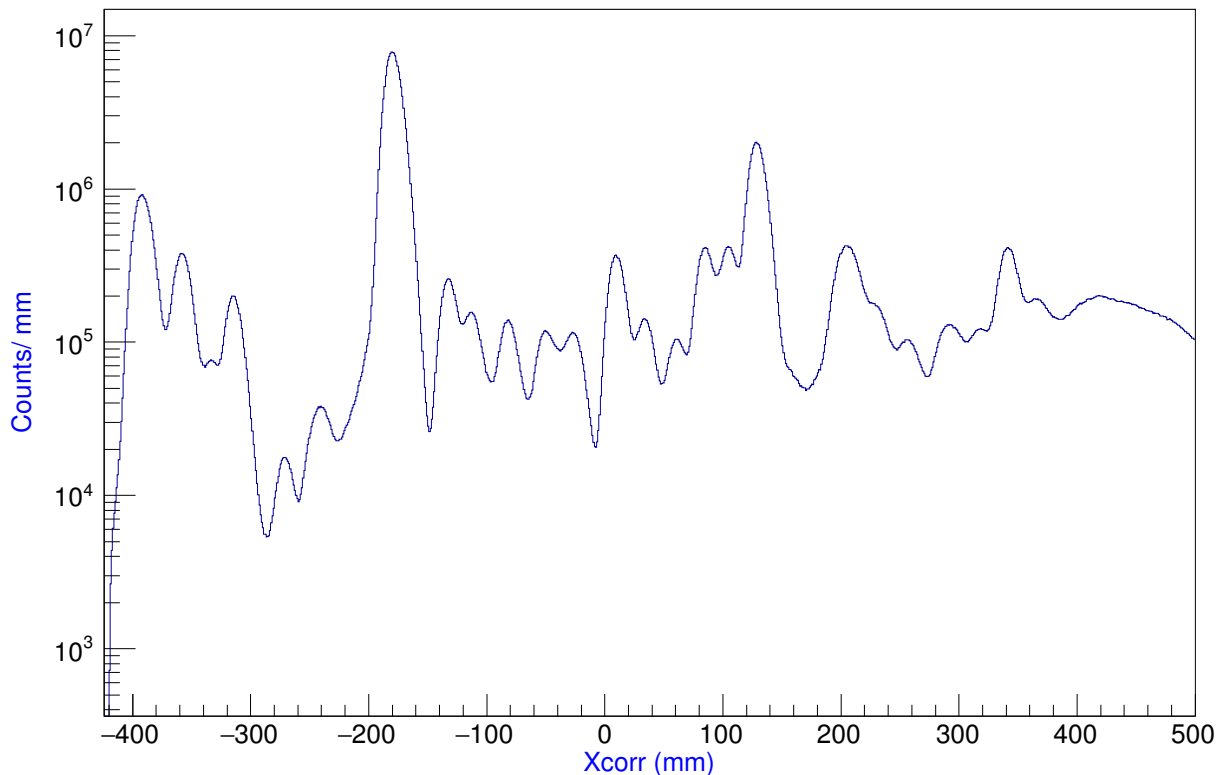


Figure 4.6: Final full corrected focal plane spectra, showing the uncalibrated excitation spectrum of  $^{28}\text{Si}$ .

To calibrate from position to excitation energy the peak position of known peaks covering a wide range of the focal plane was required. This was done by fitting multiple Gaussians over overlapping peaks. Figure 4.7 shows the results for 6 sample peak that were fitted. Their energies were plotted against their fitted centroids as illustrated in Figure 4.8. A linear polynomial was fitted to all of the data points yielding:

$$E_x = 8.7997 + 0.0107 X_{\text{Corr}} \quad (4.3)$$

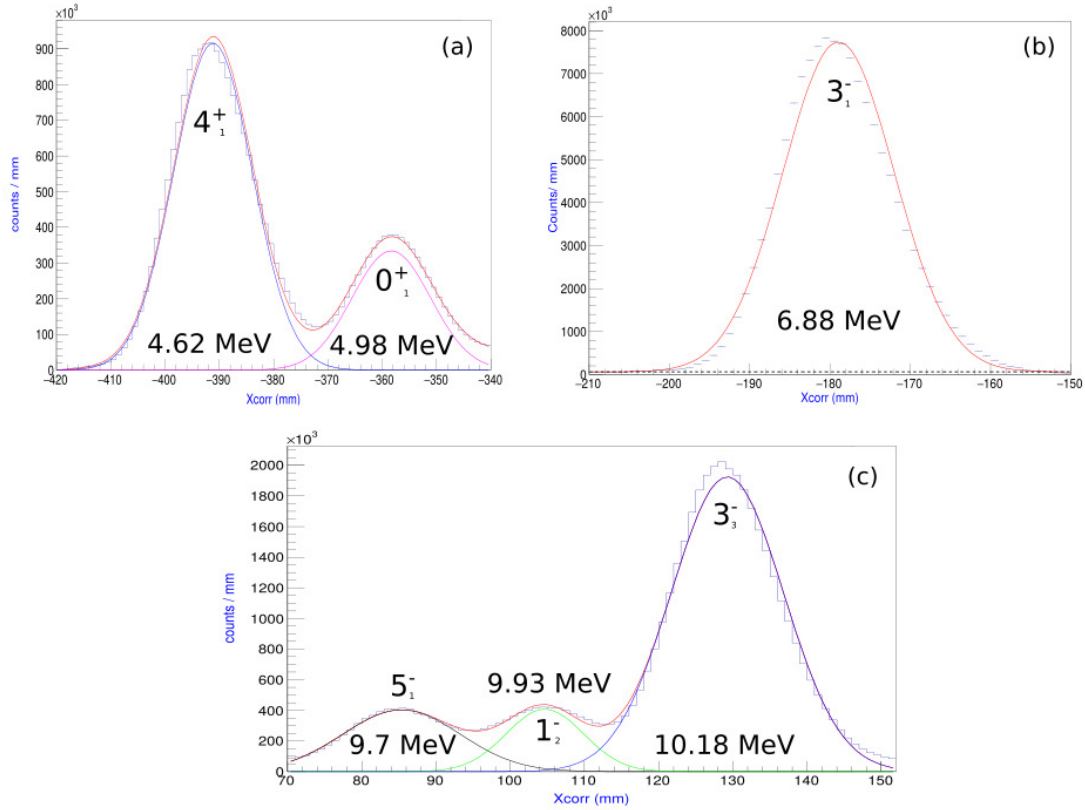


Figure 4.7: Focal plane peak fitting procedure. Multi-Gaussian fits were applied to partially overlapping states. The centroids of known states were then used for the focal plane calibration. (a) Low energy states (b) Medium energy (c) Higher energy states.

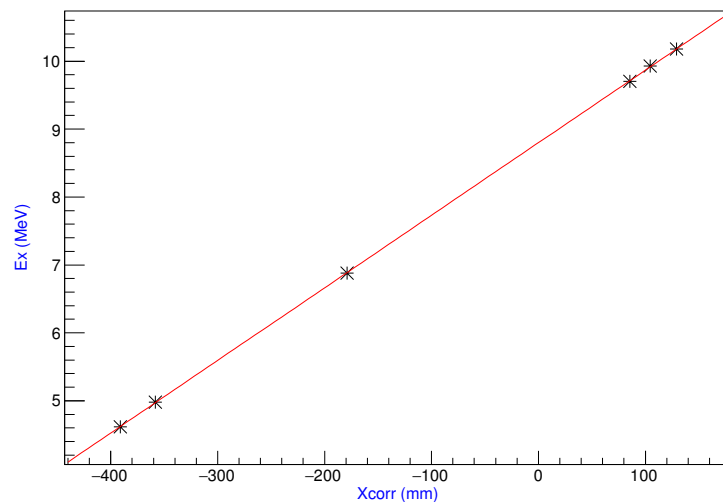


Figure 4.8: Linear calibration for the focal plane detector, converting from position to excitation energy using 6 data points over a wide range of the focal plane.

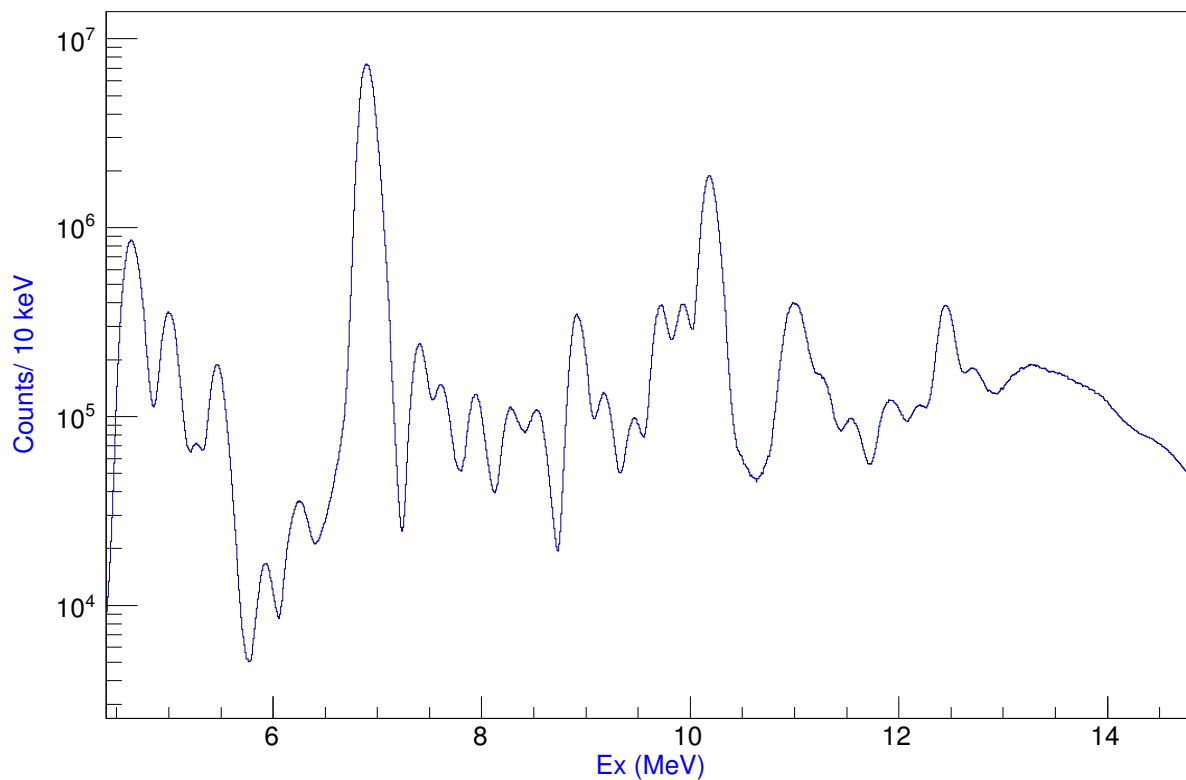


Figure 4.9: Calibration of focal plane spectrum, going from position in mm to excitation energy of  $^{28}\text{Si}$  in MeV

Equation 4.3 was then used to construct Figure 4.9, showing the calibrated focal plane spectrum which covered a range from 4 MeV to just over 14 MeV in excitation energy.

# Chapter 5

## CAGRA Analysis

The next stage of the analysis was to analyse data taken from the Cagra array. First, all 48 clover crystals needed to be energy calibrated before any  $\gamma$ -ray spectroscopy could be performed. Then, prompt timing between CAGRA and GR was characterised to ensure events analysed were in true coincidence. Addback was then implemented to increase efficiency of the Cagra array and its effectiveness will be detailed in this chapter. Once all these steps have been achieved, it's then possible to study the correlation between excitation energy in  $^{28}\text{Si}$  and its subsequent coincident  $\gamma$ -ray emission.

### 5.1 Energy Calibration: Clover Crystals

This research faced a difficulty that a very broad range of  $\gamma$ -ray energies were expected, that were of interest. The calibration sources used therefore needed to cover as much of this range as possible for a reliable calibration. The three calibration sources used were  $^{60}\text{Co}$ ,  $^{56}\text{Co}$  and  $^{152}\text{Eu}$  with  $\gamma$ -ray energies ranging from 344.3 to 3548.05 keV. Table 5.1 summarises the source activities used and each run's duration. Figure 5.1 gives the three uncalibrated spectra for each source for one example crystal (#4). Figure 5.2 shows the results from all 18 data points used, a quadratic polynomial was fitted which yielded Equation 5.1.

Table 5.1: Calibration and absolute efficiency source information.

Source	Activity (kBq)	Run Duration (s)
$^{60}\text{Co}$	$81.3 \pm 0.813$	1350.0
$^{56}\text{Co}$	$18.14 \pm 0.1814$	11807.0
$^{152}\text{Eu}$	$319.0 \pm 3.19$	1815.0

$$\text{Energy} = -1.0844 + 1.94799 \times \text{Ch} + 1.42294 \times 10^{-6} \times \text{Ch}^2 \text{ keV}. \quad (5.1)$$

This was repeated for all 48 crystals, in which all offsets, gains and quadratic coefficients are listed in Table 5.2. Here, values for crystals 7 and 34 are not given because these channels were broken during the experiment.

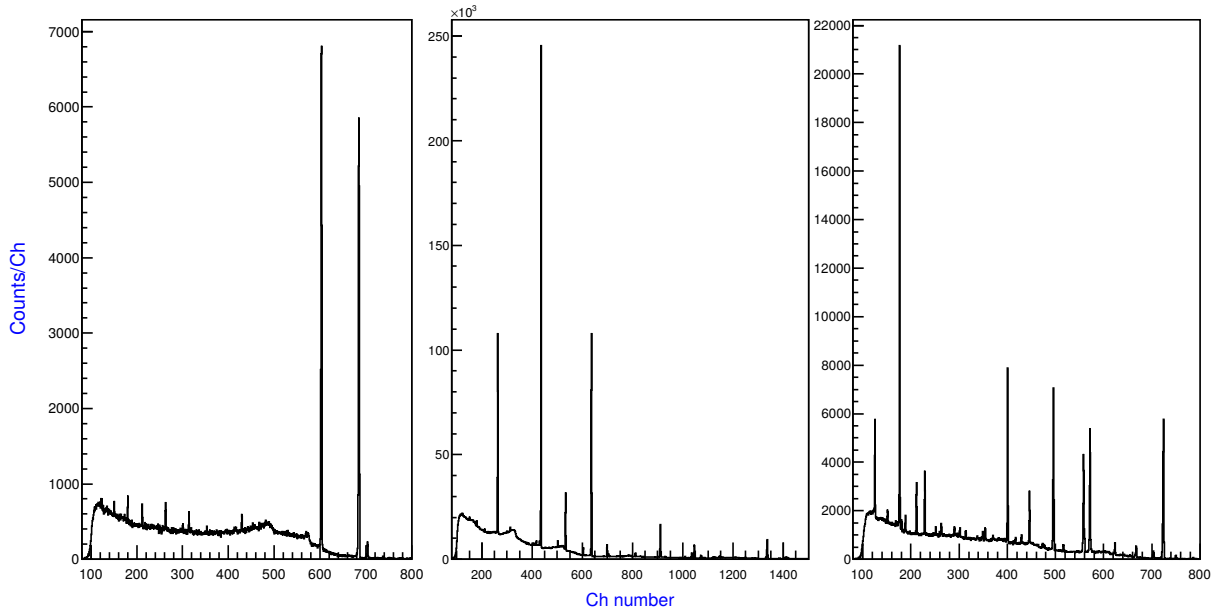


Figure 5.1: Calibration spectra for one example crystal 4 (left)  $^{60}\text{Co}$  main lines at 1173.2 & 1332.5 keV. (middle)  $^{56}\text{Co}$  with energies used from 847.0 to 3548.05 keV. (right)  $^{152}\text{Eu}$ , lowest data point at 344.3 keV up to 1408.0 keV.

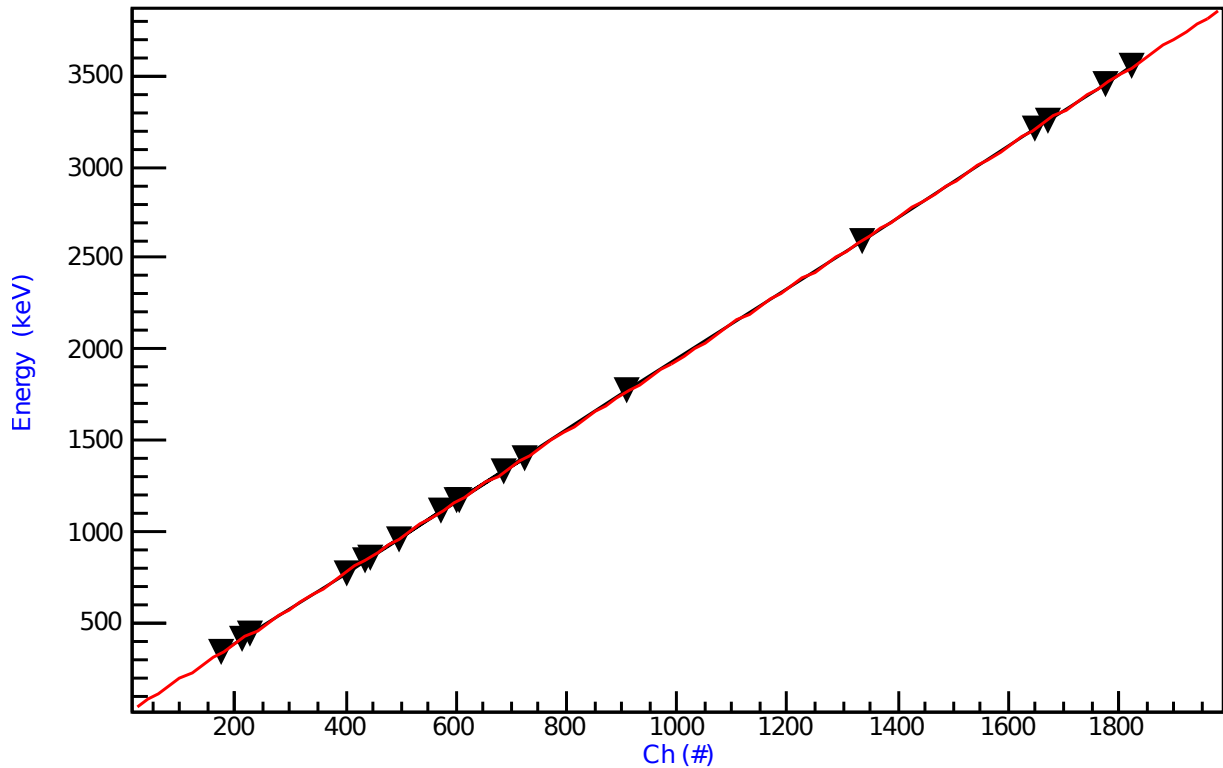


Figure 5.2: Quadratic calibration fitting procedure for one example crystal (#4), all data points were taken from the spectra in Figure 5.1 from  $^{60}\text{Co}$ ,  $^{56}\text{Co}$  and  $^{152}\text{Eu}$  calibration sources.

## 5.2 CAGRA Efficiency

The absolute efficiency of each clover crystal was then calculated. The same spectra were used as for the energy calibrations, as seen in Figure 5.1. The absolute efficiency is given by:

$$\epsilon_{Abs} = \frac{N}{AI_{\gamma}t}, \quad (5.2)$$

where, N is total number of counts for a single data point with background subtracted. A is the source activity and t is the duration of the source run as referenced in Table 5.1.  $I_{\gamma}$  is the relative intensity of each  $\gamma$ -branch.

A photopeak,  $P(E)$  was fitted with 8 parameters to each datapoint:

$$P(E) = Gauss(E_0, \sigma, H, R) + SkewedGauss(E_0, \sigma, H, R, \beta) \dots \\ + StepFunction(E_0, \sigma, H, step) + Bg(offset, slope) \quad (5.3)$$

Where  $E_0$ ,  $\sigma$  and  $H$  is the centroid, standard deviation and height of the Gaussian or Skewed Gaussian.  $R$  is the relative height between the Gaussian and Skewed Gaussian. The skewed Gaussian was needed to account for the asymmetry of the photopeaks. This is typical for Ge detectors that have received significant neutron damage, causing low energy tails. Here, the degree of skewness was controlled by  $\beta$ . If the low energy tail of a peak is sitting on top of a Compton edge, originating from another  $\gamma$ -ray, this can cause sudden step discontinuities. Therefore, a step function was also added to account for this if needed, the magnitude of which was quantified by the step parameter. Lastly, a linear background was applied with a slope and offset. Figure 5.3 shows an example application of this fitting procedure on the 1173.2-keV line in  $^{60}\text{Co}$  with each component drawn separately.

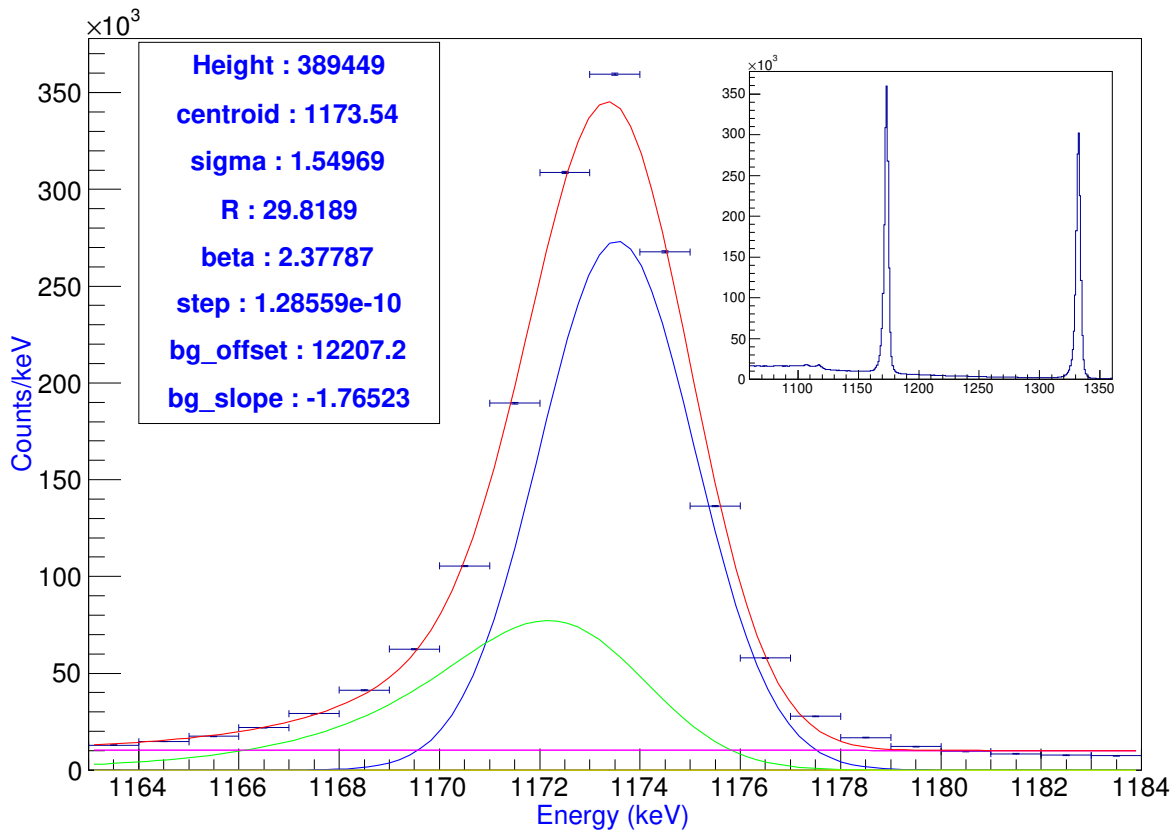


Figure 5.3: Example of peak fitting procedure on the 1173.2-keV transition from  $^{60}\text{Co}$ . The red line shows the combination of: A Gaussian drawn in blue, a Skewed Gaussian (green) and the magenta line shows a linear background. A step function was also included in this fit but had no contribution. The insert shows the fit region used on a  $^{60}\text{Co}$  run, showing the two main lines at 1173.2 and 1332.5 keV.

To get the background subtracted counts, the photopeak fit,  $P(E)$  was integrated over the full range of the fit region. Then, separately the step and linear components were both integrated and subtracted from the  $P(E)$  integral. Equation 5.2 was then used to determine the absolute efficiency for each data point. The relative intensities for  $^{152}\text{Eu}$  and  $^{56}\text{Co}$  was taken from a recent study on  $\gamma$ -ray intensity determination with precise summing corrections (Shima et al., 2016). For  $^{60}\text{Co}$ , values were taken from studies correcting for summing and angular correlations of the cascade decay (Courtine et al., 2014).

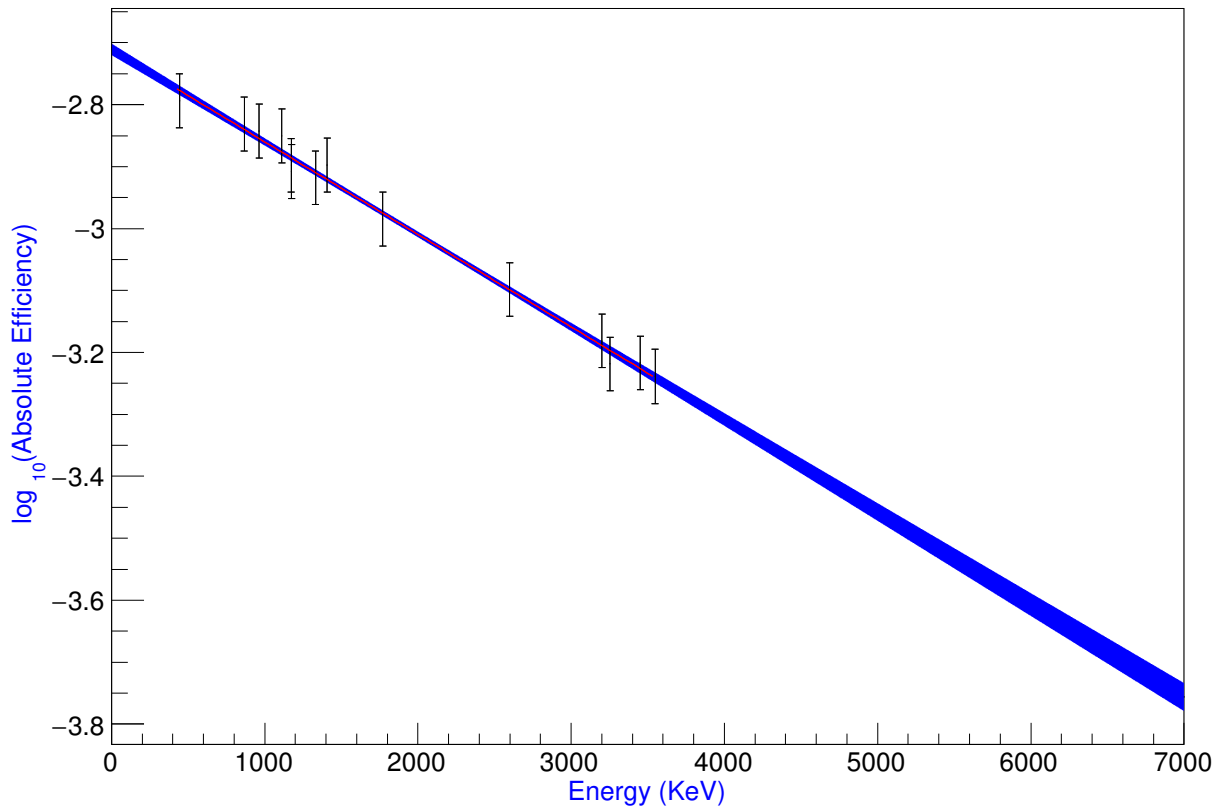


Figure 5.4: Logarithm in base 10 of absolute efficiency for one example clover detector (#5). The blue distribution shows the  $1\sigma$  confidence-interval.

Figure 5.4 shows the logarithm in base 10 of the absolute efficiency against  $\gamma$ -ray energy, with data points ranging from 444.0 to 3548.05 keV. Data points below 444.0 keV were available but were omitted due to poor efficiency fitting results. Full photopeak efficiency is maximum around 400.0 keV for HPGe detectors, introducing a turning point. After this turning point the absolute efficiency exponentially decreases with increasing energy. To accurately fit the detector response a polylogarithmic function such as:

$$\log(\epsilon_{Abs}) = \sum_{n=0}^N a_n \log^n(En), \quad (5.4)$$

is typically used to reproduce a single turning with smoother features compared to a normal polynomial function. Here,  $N$  is the order of the polylogarithmic function. However, this function yielded poor fit results when demanding the low energy turning point. No

---

$\gamma$ -rays below 444.0 keV were observed in this experiment and this justified the turn over region being omitted. Instead a linear function was fitted to data as seen in Figure 5.4. The red line shows the line of best fit and the blue region is the confidence interval drawn for  $1\sigma$ . As  $\gamma$ -ray energies of interest were significantly higher than that available from standard calibration sources, extrapolation of efficiency at energies greater than 3548.05 keV was necessary. The confidence interval in Figure 5.4 shows how the error grows significantly for larger extrapolations. This had adverse consequences on the precision to which branching ratios with high energy  $\gamma$ -transitions could be calculated. To obtain absolute efficiencies for either grouped clovers or the entire CAGRA array the efficiencies were appropriately summed.

Table 5.2: CAGRA crystal information. N.B. crystals 7 and 34 were not in use.

Crystal Number	Slot Number	Offset	Gain	Quadratic	Pole Zero
0	5	-0.0523702	2.31757	-2.13204e-7	0.8910
1	5	1.89506	2.38303	2.60466e-6	0.8906
2	5	0.793988	2.35783	8.39078e-7	0.8914
3	5	1.6807	2.29384	1.56288e-6	0.8915
4	6	-1.0844	1.94799	-1.42294e-6	0.8824
5	6	0.986484	2.30076	1.49099e-6	0.8904
6	6	0.74108	2.32272	7.87691e-7	0.8895
7	6	N/A	N/A	N/A	N/A
8	7	0.499724	2.25393	7.1286e-7	0.9083
9	7	1.65873	2.31119	2.2385e-6	0.911
10	7	1.10912	2.24816	1.74369e-6	0.9083
11	7	1.60912	2.23243	1.34427e-6	0.911
12	8	1.17377	2.25145	1.9781e-6	0.9061
13	8	-0.706015	2.30416	-7.74857e-7	0.9044
14	8	3.32617	2.32136	3.4749e-6	0.9049
15	8	1.47564	2.23966	2.07489e-6	0.9025
16	9	1.02634	2.27052	9.58707e-7	0.8956
17	9	-4.1345	2.46437	-8.35214e-7	0.884
18	9	-2.06478	2.46787	6.66307e-7	0.8905
19	9	1.23873	2.49222	1.80155e-6	0.8918
20	10	2.57612	2.37463	5.81553e-6	0.9102
21	10	0.756875	2.33279	6.27612e-7	0.9082
22	10	1.46211	2.48059	1.91665e-6	0.8902
23	10	1.8136	2.43794	1.74887e-6	0.899
24	11	-2.16897	2.35174	-3.98001e-6	0.8925
25	11	1.64852	2.38026	4.10886e-6	0.8927
26	11	0.963456	2.4184	1.75728e-6	0.8918
27	11	2.15586	2.28635	2.92783e-6	0.8917
28	12	-0.226019	2.20489	3.04067e-7	0.9076
29	12	0.519875	2.21189	2.51964e-7	0.9105
30	12	0.641008	2.24978	1.24507e-6	0.9096
31	12	1.74911	2.24244	1.48514e-6	0.9101
32	13	4.883	2.22017	9.68839e-7	0.9111
33	13	0.114371	2.2216	6.02555e-7	0.9101
34	13	N/A	N/A	N/A	N/A
35	13	0.787158	2.31964	1.73683e-6	0.9128
36	14	1.26719	2.25508	5.09543e-7	0.9103
37	14	-0.906536	2.24117	-4.75636e-8	0.9127
38	14	1.27347	2.28642	2.41191e-6	0.9082
39	14	-0.111823	2.30984	1.13172e-6	0.907
40	15	0.830961	2.29041	8.27326e-7	0.9106
41	15	1.43131	2.30357	5.09576e-7	0.9108
42	15	0.866554	2.2937	5.91296e-7	0.9115
43	15	1.92131	2.37581	5.55347e-6	0.9117
44	16	2.03507	2.37634	2.17294e-6	0.9115
45	16	1.46298	2.31454	1.6138e-6	0.9116
46	16	0.132266	2.44651	4.49092e-7	0.9081
47	16	0.922033	2.32033	1.43314e-6	0.9122

### 5.3 Prompt Timing

The cyclotron beam bunch frequency was 12.4 MHz, i.e. a beam bunch interval of 80.645 ns. Prompt  $\gamma$ -rays should be in synchronisation with the cyclotron. Therefore, the time difference between any CAGRA and GR plastic event will separate the true correlated GR- $\gamma$  coincidences from time random uncorrelated chance coincidence events.

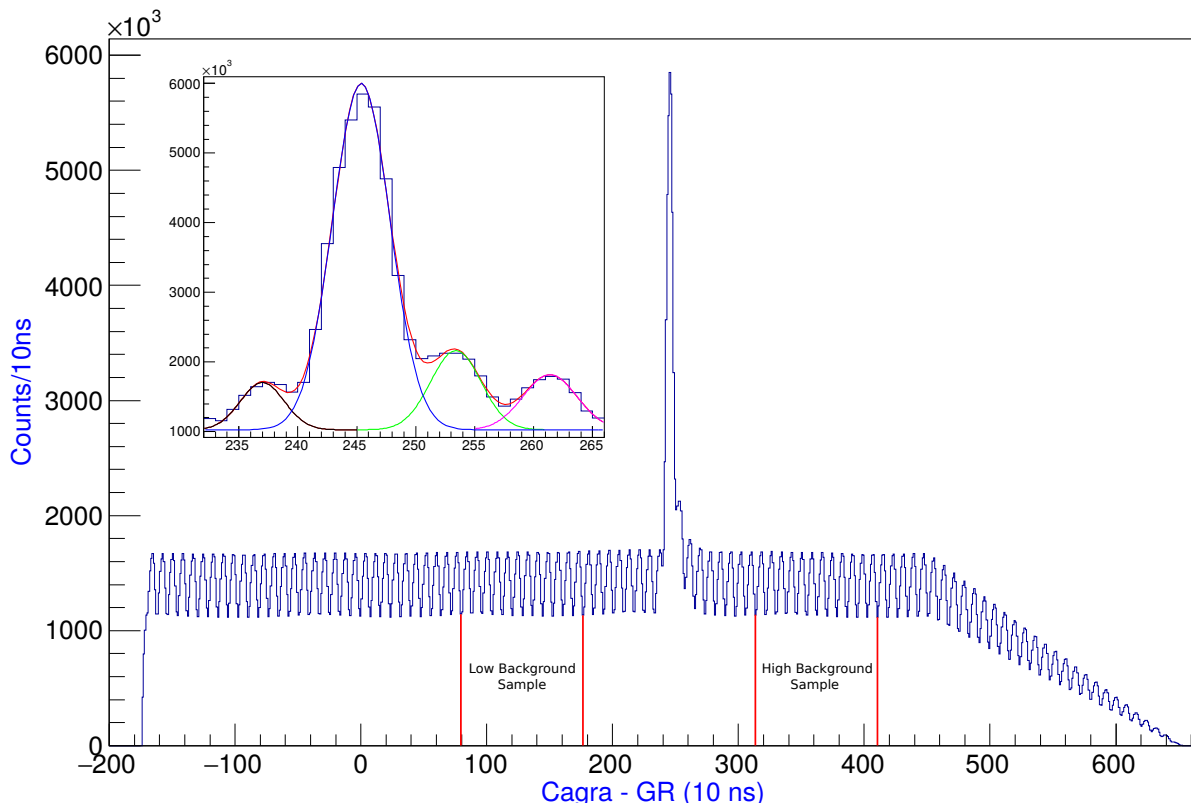


Figure 5.5: Prompt timing distribution between CAGRA timestamp and a coincident GR timestamp. The prompt peak is clearly visible. The satellite peaks are random coincidences from either time random background or beam induced events from non coincident GR-CAGRA timestamp correlation. The red lines show the limits for the background subtraction.

The timing of each clover crystal can differ, due to differences in length of wires or electrical resistance for each DAQ channel. Also, the different voltages applied to each clover detector will affect charge collection times and thus the trigger timing. Therefore, the fitting was repeated for each crystal. The prompt timing gate width was set to  $4\sigma$  centered around each crystals centroid, ensuring 99.99 % of the prompt events were inside of the gate but removing background.

## 5.4 Clover Energy Rate Dependence

Online analysis during the experiment shown unexpected double peaking in the clover detector  $\gamma$ -ray energy spectra. Further work offline attributed this to a rate dependence in the baseline signal. Plotting  $\gamma$  energy vs time over a run highlights the extent of the dependence as seen in Figure 5.6(a). Here, the energy is fluctuating with time due to a baseline shift. The baseline Vs time, Figure 5.6(b), shows the same correlation as Figure 5.6(a). If compared to the source runs, for example  $^{60}\text{Co}$ , there is no evident shift in energy, Figure 5.6(c), or baseline, Figure 5.6(d), with time. This is because the source activity is constant over the time scale of the source run. However, the rate of the cyclotron was changing significantly over time scale of a single run time ( $\approx 1\text{hr}$ ), causing a rate dependent shift in the run data.

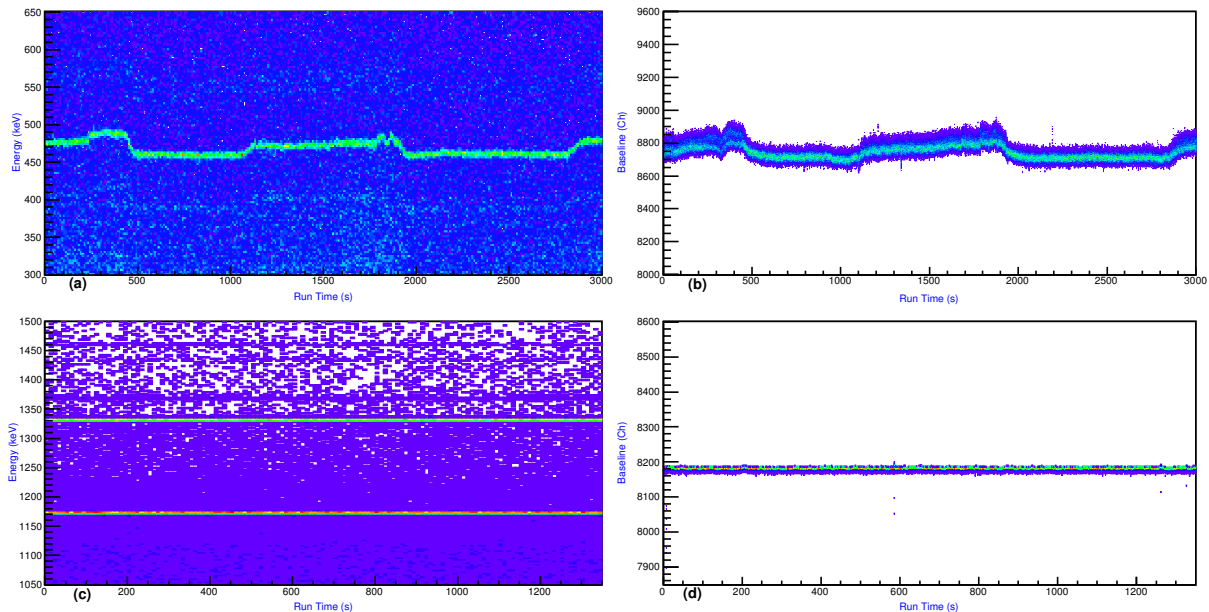


Figure 5.6: Rate dependent shift: (a) An in-continuous shift of the 511-keV energy, tracking over 3000 s. (b) This figure shows the baseline over the same period of time, with the same correlation as Figure (a). Figure (c) and (d) show the same but for the source run data, with no fluctuation in energy.

## 5.5 Kalman Filter Baseline

The comparison between source and beam runs also shows how the distribution of baseline values broaden (even accounting for rate dependence) during beam runs due to large statistical fluctuations. Therefore, it was necessary to perform some post pulse-shape analysis (PSA) to acquire a more reliable baseline estimate. Here, a moving average was applied based on the Kalman filter method:

$$B_{kal} = B_{kal} + kal_{gain}(B_{sample} - B_{kal}). \quad (5.5)$$

The Kalman Baseline,  $B_{kal}$ , was given an initial starting value equal to the mean Baseline sample. This initial estimate is updated recursively based upon the statistical weight  $kal_{gain}$ , known as the Kalman Gain. This was set to 0.005, which yielded the best performance overall. However, this differs from the standard Kalman filter which gives more weight to observables with lower uncertainty. As here only one experimental observable was used, this was not needed. The results of the application of the filter can be seen in Figure 5.7(b), here the width has been significantly reduced. The insert in Figure 5.7(a) shows the projection of baseline sample between 2100 and 2400 s, where the rate was relatively constant. A Gaussian was fitted, as shown in red, yielding a FWHM of  $48.155 \pm 0.121$  Channels. The same is shown for the Kalman filtered baseline, insert in Figure 5.7(b), which gave a FWHM of  $13.014 \pm 0.036$  Channels. The Kalman filter, therefore significantly improved the accuracy of the baseline signal determination.

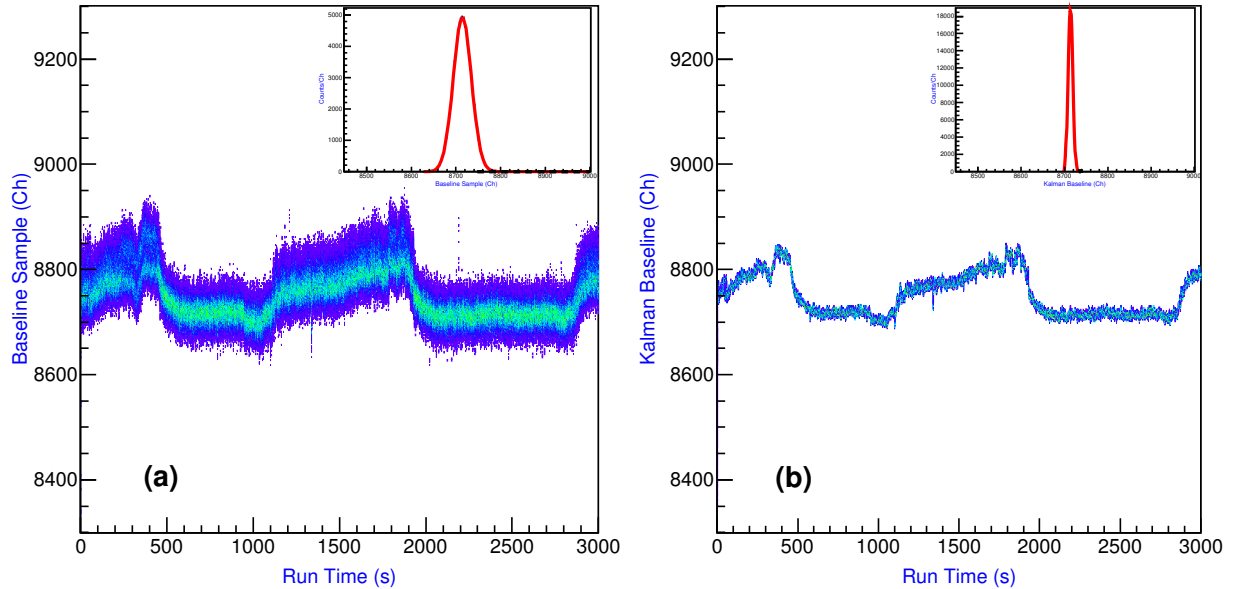


Figure 5.7: (a) Raw baseline sample over one beam run, showing a broad distribution (b) Baseline sample after the Kalman filter application, showing a more accurate estimate and narrower distribution of the baseline.

## 5.6 Clover Energy Determination

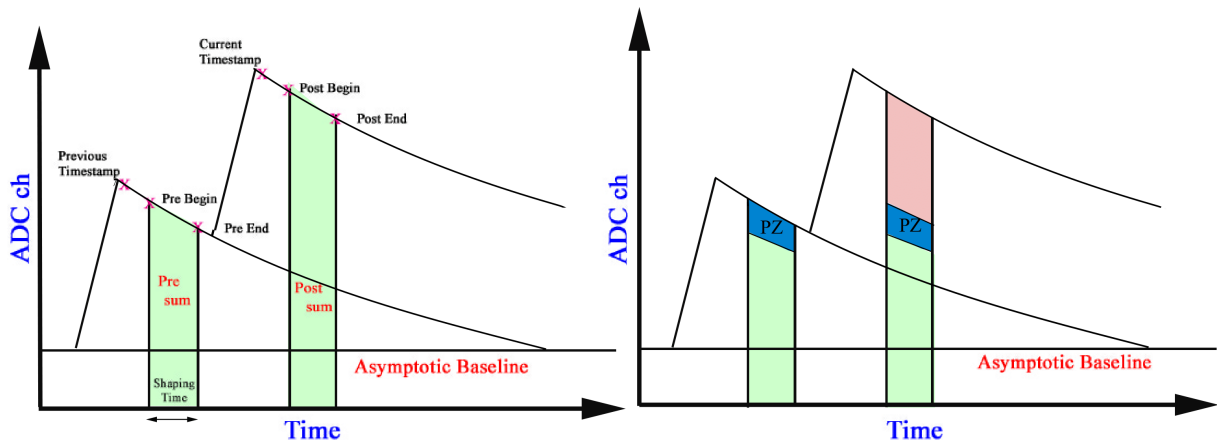


Figure 5.8: Schematic diagram of  $\gamma$ -ray energy determination using the sum method. The DAQ subtracts a pre-sum from a post-sum integral (left). The right figure shows a pole-zero correction to account for pulse pile up. Adapted from (Weinert, 2019).

Due to memory restrictions, the entire signal trace of every event could not be stored. Instead, only sample points of interest were stored. Figure 5.8(a) illustrates a typical raw

signal trace from a clover crystal and demonstrates a typical pulse pile up event. The Current TimeStamp is produced from the LED trigger point. This timestamp is then associated with a post trigger integration region,  $Post_{sum}$ , marked between Post Begin & Post End. Also stored, is a Pre-rise integration region,  $Pre_{sum}$ , between Pre Begin & Pre End. The width of these integration regions was set by a Shaping Time of 350 samples i.e  $3.5 \mu s$ . The energy of the each event was determined from:

$$Energy = \frac{(Post_{sum} - pzPre_{sum})}{Shaping Time}. \quad (5.6)$$

This gives the difference in area between the two green regions in Figure 5.8(a). Dividing by Shaping time simply gives the height, which is proportional to the energy of the  $\gamma$ -ray. However, a Pole-Zero correction term,  $pz$ , was necessary to correct for the overestimation of the  $Pre_{sum}$ . This was being caused by pulses sitting on top of the exponential decay of previous pulses. This parameter then scales down the  $Pre_{sum}$  area as shown in blue on Figure 5.8(b). Figure 5.9 shows the effect of the Pole-Zero parameter on the detector resolution of crystal 46, here the FWHM of the 511-keV peak was used a standard reference. Too high Pole-Zero values did not account for the overestimation, yielding low energy tails in the 511 peak. Too low Pole-Zero values over-corrected, causing high energy tails. These tails worsened energy resolution and therefore the Pole-Zero was chosen which achieved the optimum resolution. For crystal 46 this corresponded to a value of 0.9081 achieving a FWHM of  $7.519 \pm 0.122$  keV, in which the tails were removed. This was repeated for all crystals and the optimum pole-zero values for each crystal are given in Table 5.2.

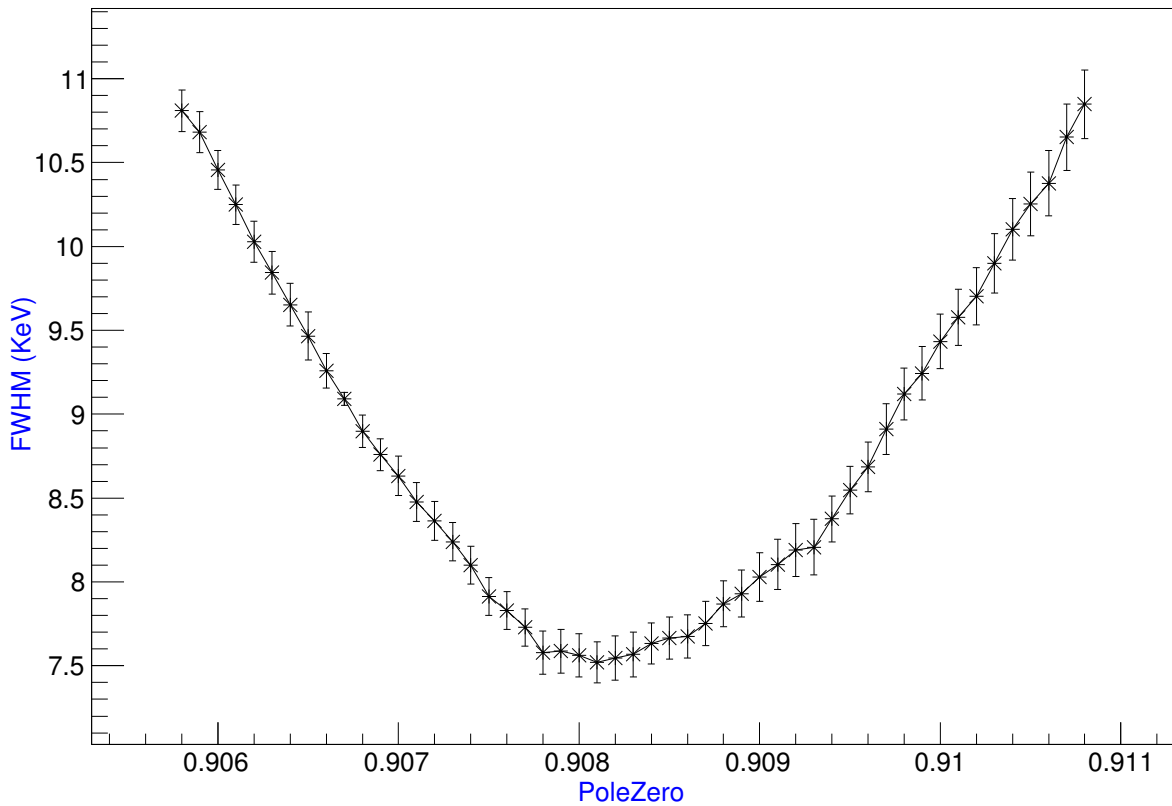


Figure 5.9: Pole-zero optimisation needed due to pulse pile up. Resulting in a much better energy resolution.

In the case of a no pile up event, the height of the  $Pre_{sum}$  should simply be at asymptotic baseline. However, the Pole-Zero would still be applied and therefore a correcting factor:

$$Energy = Energy + Asym(1 - pz), \quad (5.7)$$

was included to compensate for this issue.

To further improve resolution, the rate dependence of the baseline had to be removed. There were several attempts to achieve this: One method was a fitting procedure. Using the same pulse samples marked out in Figure 5.8(a), an exponential was fitted to the decay of each pulse. An optimum decay constant for each crystal & pre-amplifier was determined. The fit was used to extrapolate the asymptotic baseline instead of obtaining it from the Kalman filter procedure. The sum method was then applied using the fit to determine the

energy. This method was independent of rate. However, this suffered from poor resolution due to the inherent error in the fitting procedure. Another disadvantage was the increased sorting time due to each pulse having to be fitted.

Another method tested was to fit the energy shift as a function of rate. This was achieved by gating on different points in time corresponding to a distinct rate. The fit was then used to shift the energy depending on the rate. This method also suffered from poor resolution. In which was most likely due to the difficulty in fitting the true dependence of rate on the baseline shift.

In the end an algorithm was created to track the 511-keV peak centroid position. It was fitted every 30 seconds for every run and for each crystal. Each peaks measured centroid shift relative to 511 keV was tabulated. Then in the sorting process depending on the timestamp and crystal the appropriate shift was applied. This was more robust than the other methods, being more sensitive to discontinuities and large sudden changes in baseline. These features are evident in Figure 5.10(a), the insert is the projection onto the energy axis and shows a triple peak caused by the rate dependence. Fitting a triple Gaussian yielded centroids at 461.16, 475.4 and 489.12 keV. However, this is not physical as only a single peak is expected from a unique  $\gamma$ -ray transition from a stationary source.

After applying the energy shifts these features were removed, in which can be seen in Figure 5.10(b). The insert here shows that the triple peaking was removed and the energy resolution was significantly improved to  $7.304 \pm 0.086$  keV.

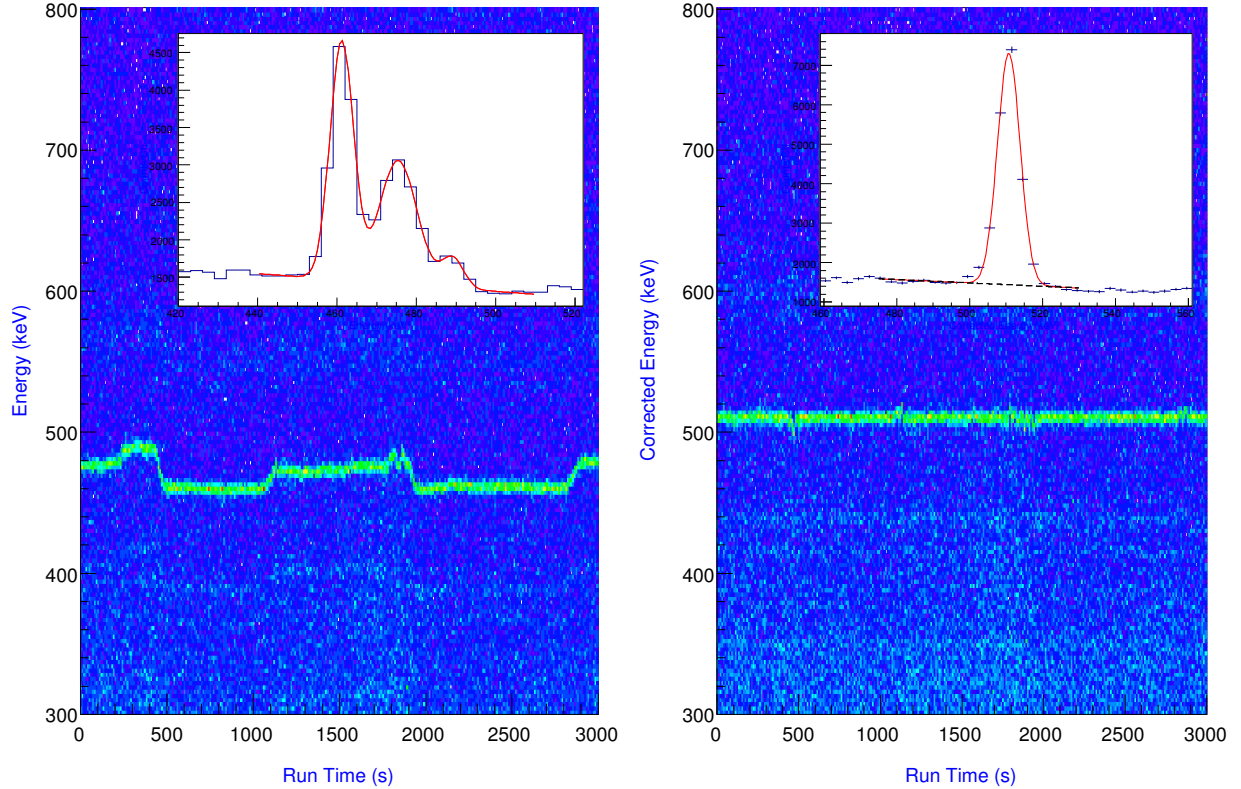


Figure 5.10: (a) Energy Vs Time for one example crystal 45 showing a strong fluctuation in energy determination, insert shows the projection onto the energy axis with deteriorated energy resolution and triple peaking. (b) After the rate dependent shift correction. Insert showing the superior energy resolution and triple peaking removed.

## 5.7 Doppler Energy Corrections

The energy measured by the CAGRA array is in the laboratory frame of reference. Due to the kinematics of the inelastic scattering reaction,  $^{28}\text{Si}(\alpha, \alpha')^{28}\text{Si}^*$ , the excited  $^{28}\text{Si}^*$  nucleus recoils at a significant fraction of the speed of light,  $\beta(\text{Ex}) = \frac{v(\text{Ex})}{c}$ . The polar scattering angle of the alpha particle (ejectile) is fixed around  $9.1^\circ \pm 1.5^\circ$  due to the opening angle of the GR spectrometer. The initial beam kinetic energy is also fixed at 130 MeV. Therefore, conservation of momentum and energy constrains the possible  $\beta$  and recoil scattering angles possible, depending on the excitation energy of the recoil. As the excitation energy is reconstructed from the focal plane, this allows  $\beta$  and the recoil scattering angle to be reconstructed event by event. To convert the  $\gamma$ -ray energy measured

in the laboratory frame,  $E_{\text{lab}}$ , to the recoil rest frame,  $E_{\text{rest}}$ , the Doppler shift must be taken into account using:

$$E_{\text{rest}} = E_{\text{lab}} \frac{1 - \beta \cos(\theta)}{\sqrt{1 - \beta^2}}, \quad (5.8)$$

where  $\theta$  is the detection angle with respect to the recoil velocity,  $\hat{\mathbf{v}}$  or position vector,  $\hat{\mathbf{r}}$ . These vectors were calculated from the reconstructed recoil scattering angle. The position vector of each clover crystal,  $\hat{\mathbf{a}}$ , is known and fixed from the experimental set-up. For addback events the crystal position corresponded to the crystal with the highest recorded energy. The detection angle was then calculated for each  $\gamma$ -ray event by:

$$\theta = \arccos\left(\frac{\hat{\mathbf{v}} \cdot \hat{\mathbf{a}}}{|\mathbf{v}| |\mathbf{a}|}\right). \quad (5.9)$$

The recoil travelled through a thick 11 mg/cm<sup>2</sup> <sup>nat</sup>Si target and so significant energy loss occurred depending on the lifetime of the state. To quantify this a simple model was created to calculate the average time taken to slow the recoil down from an initial  $\beta_i$  to a final  $\beta_f$ . Here,  $\beta_f$  corresponded to the average velocity of the recoil after one lifetime. This required the stopping power,  $\frac{dE(E_{\text{kin}})}{dx}$ , of <sup>28</sup>Si in <sup>nat</sup>Si to be known as a function of its kinetic energy,  $E_{\text{kin}}$ . Which was taken from the Stopping and Range of Ions in Matter toolkit (SRIM) (Ziegler et al., 2010). With the following assumptions:

$$\frac{\Delta E}{P(E_{\text{kin}})} = \Delta t, \quad (5.10)$$

$$\lim_{\Delta E \rightarrow 0} \frac{dE}{P(E_{\text{kin}})} = dt, \quad (5.11)$$

$$P(E_{\text{kin}}) = \frac{dE(E_{\text{kin}})}{dx} |\hat{\mathbf{v}}| \quad \text{and} \quad (5.12)$$

$$t = \int_{E_i}^{E_f} \left[ \frac{dE(E_{\text{kin}})}{dx} \sqrt{\frac{2E_{\text{kin}}}{m}} \right]^{-1} dE. \quad (5.13)$$

The stopping time,  $t$ , was estimated.  $P(E_{\text{kin}})$  is the rate of energy loss. As no analytical function existed for the total stopping power, the integral was numerically computed using a cubic spline interpolation method (Lamnii et al., 2016). To estimate  $E_f$ , the data was re-analysed for varying fractions of effective  $\beta_i$ , ranging from 0 to 1 in steps of 0.2. A value of 1 equates to a recoil with zero energy loss, conversely, a value of 0 represents a fully stopped recoil within the target. The analysed  $\beta$  with the optimum energy resolution was then used to calculate  $E_f = \frac{1}{2}m(\beta_f)^2$ . This was first tested on the 6877.0-keV  $J^\pi = 3_1^- \rightarrow g.s.$   $\gamma$ -ray transition, which has a 2.74-ps lifetime. Figure 5.11 shows this transition Doppler corrected for each fraction of  $\beta$ . The blue line tracks the FWHM and is minimum for  $\beta_f = 0$  i.e. is expected on average to be fully stopped before decaying. This is in agreement with the stopping time model, as integrating from its initial energy,  $E_i = 478$  keV, to its final energy,  $E_f = 0$  keV, yields 711.59 fs. This is approximately a quarter of the  $J^\pi = 3_1^-$  states lifetime, so would be expected to be fully stopped.

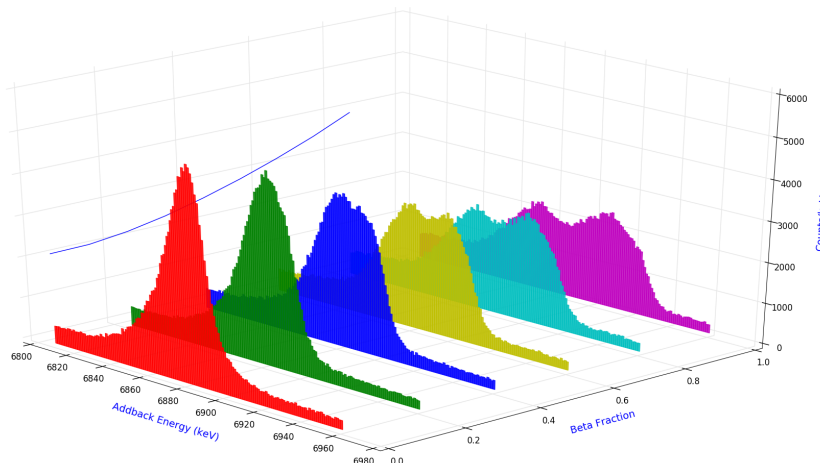


Figure 5.11: 3-D representation of the  $\beta$  distribution for a short lived state, in particular for the 6877.0-keV  $J^\pi = 3_1^- \rightarrow g.s.$   $\gamma$ -ray transition in which has a 2.74 ps lifetime. The blue line tracks the FWHM and is minimum for  $\beta=0$ .

Next, the method was tested on a state with a relatively short lifetime. Therefore, the 2838.29-keV  $J^\pi = 4_1^+ \rightarrow 2_1^+$   $\gamma$ -ray transition with a lifetime of 53.38 fs was chosen. A  $\beta_f$

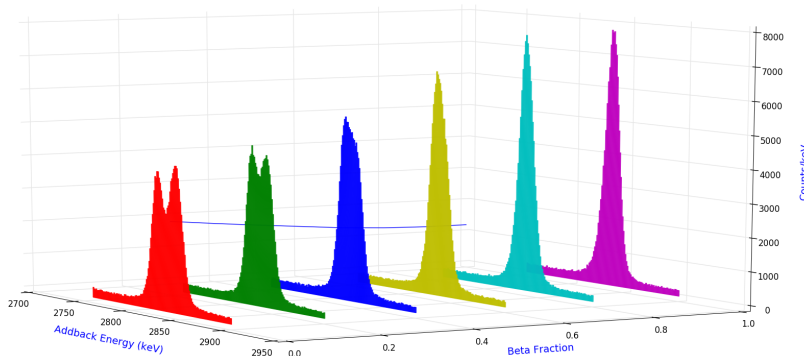


Figure 5.12: 3-D representation of the  $\beta$  distribution for the 2838.29-keV  $J^\pi = 4_1^+ \rightarrow 2_1^+$   $\gamma$ -ray transition with a lifetime of 53.38 fs. The blue line tracks the FWHM and plateaus around  $\beta=0.8$ .

value of 0.924 was required to get a slowing time equal to the lifetime of this state. This is confirmed in Figure 5.12, where the optimum resolution starts to plateau after a  $\beta$  fraction of 0.8. The  $J^\pi = 3_1^+ \rightarrow 2_1^+$   $\gamma$ -ray transition with 1.13 ps lifetime was tested and Figure 5.13 shows the beta fraction optimisation for this state, here a minimum around  $0.2\beta_i$  is observed. The stopping time model for this transition yielded 0.66 ps, the discrepancy clearly shows the weakness in this primitive model.

There is limited lifetime sensitivity for decays with intermediate lifetimes. One reason is that this model ignores the more realistic exponential decay, since after one lifetime 63.21% on average will have already decayed. However, the stopping time model assumes all nuclei have decayed exactly after one lifetime. Also there will have been significant energy straggling through the stochastic collisions of the recoil with the target. Precision lifetime measurements such as Recoil Distance Doppler-Shift (Dewald et al., 2012) and Doppler-Shift attenuation Methods (Brandolini & Ribas, 1998) would offer greater lifetime measurement sensitivity. However, these methods require detailed Monte-Carlo simulations to model the stochastic processes previously mentioned. Great effort also has to be undertaken before the experiment and requires optimisation of beam parameters,

choice of degrader material and thickness. As the aim of this experiment was not lifetime measurements, this was not undertaken.

The sensitivity achieved is enough to acquire the magnitude of a particular states lifetime. This turned out to be a powerful tool when assigning  $\gamma$ -decays to possible states. Particularly at higher excitation where level density increased.

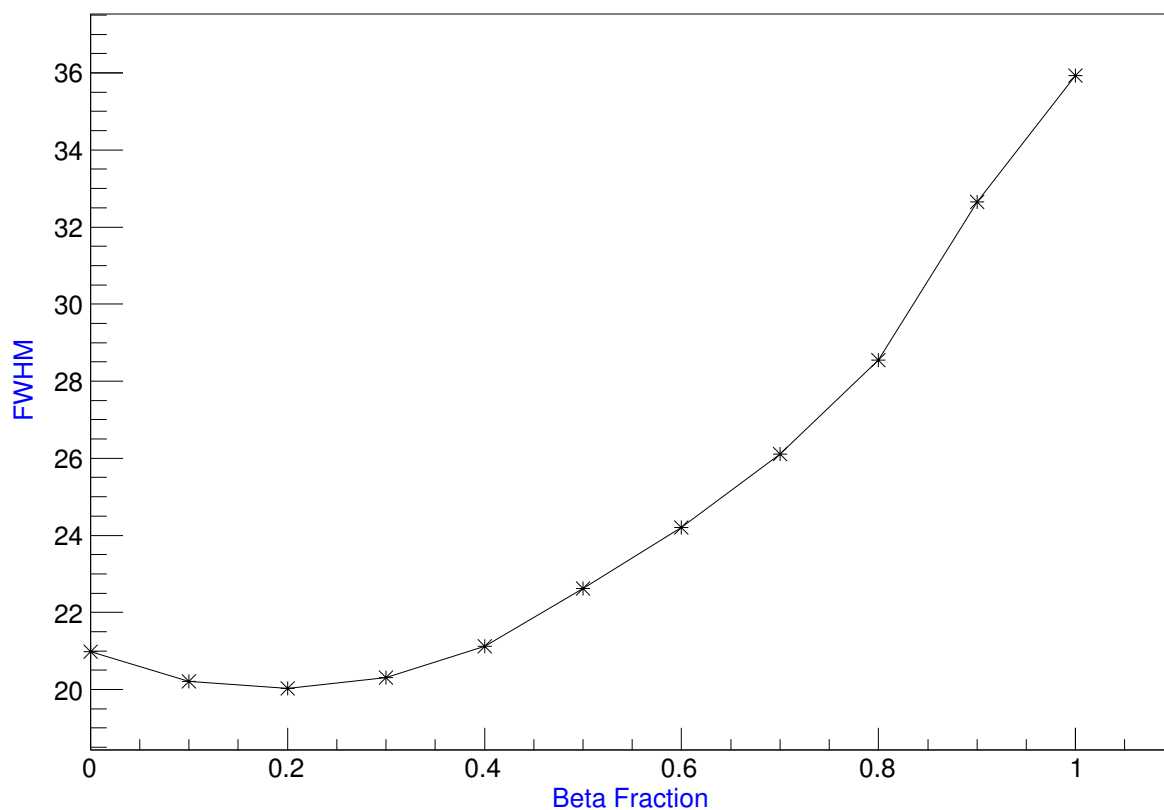


Figure 5.13:  $J^\pi = 3_1^+ \rightarrow 2_1^+$   $\gamma$ -ray transition with 1.13 ps  $\beta$  optimisation, minimum at  $\beta = 0.2$ .

## 5.8 Addback Implementation

The effectiveness of addback is controlled by the ability to separate true addback events from background chance coincidences and coincidence summing. The extent of these is largely dependent on the geometry of the detector array, the distance to target and crystal spacing. The design of the clover detector as previously discussed is also a major factor.

One of the ways to reduce background contamination is to restrict which combinations of clover segments contribute to addback. In particular at intermediate energies where Compton scattering is dominant, only adjacent crystals should be used. As the segment readout was unavailable during this campaign this was not possible to implement due to a shortage in DAQ-channels.

Only three possible modes to operate addback were available: Adding all energies of events from a single clover detector, adding up all event energies from a clover and its nearest neighbours, or summing over all events in the entire clover array. To confidently choose the best operating mode a detailed and comprehensive Monte-Carlo simulation should be performed, for example using the Geant4 toolkit. Due to time constraints this analysis was not performed and existing simulations of CAGRA were not available. However, similar analysis has been performed by M.A. Schumaker and C.E. Svensson for the TIGRESS array located at TRIUMF. They simulated  $\gamma$ -rays with multiplicities up to 40 with energies between 40 to 10,000 keV. Then using the following as a Figure of Merit,  $\zeta$ , to quantify the effectiveness of each addback method:

$$\zeta = \frac{\epsilon_{abs} P}{\delta E_{\gamma} T}, \quad (5.14)$$

where  $\epsilon_{abs}$  and  $\delta E_{\gamma}$  are the absolute efficiency and energy resolution respectively and  $\frac{P}{T}$  is the peak to total ratio. They found the optimal mode was sensitive to the multiplicity of the addback event and its energy. For all multiplicities no addback is most effective at low energies where photoelectric effect is dominant, as here addback only increases the probability of adding noise or background to the full energy photopeak. At intermediate energies the probability of Compton scattering increases and so the selective mode be-

comes most effective. Then, at higher energies the nearest neighbour mode becomes more favourable. This is due to the increasing probability of pair production, in which deposits full energy over multiple combinations of Compton scattering and photoelectric absorption interactions. This increases the chance of  $\gamma$ -rays escaping and entering neighbouring clover detectors. Overall they found no improvement by summing over the entire array. Most importantly summing over more crystals becomes less effective as multiplicity increases. The crystal multiplicity of CAGRA for all events inside the prompt window is plotted with its average marked in Figure 5.14. Therefore, due to the relatively high crystal multiplicity, the possibility of summing over multiple clovers was unreliable. Also, as selective mode was not available, the only option left was to sum over single clover detectors.

The next step was to optimise the chosen addback method, here timing is an important parameter. The first problem here is that multiple timestamps are associated with each addback event. Therefore, ambiguities can arise in deciding if the event truly lies within the prompt peak. A few techniques were tested. Firstly, as the timestamps were sorted time ordered, simply the last event was taken to be the trigger. The second method tested was to take the average of all the timestamps that contributed to the addback event. However, these two methods were not based on anything physical. Therefore, it was more reliable to assume the highest single energy event within the addback conditions was the trigger. Now, only if the timestamp of this event fell within the GR-CAGRA prompt peak was the addback deemed a true prompt coincidence. Although, the addback algorithm was performed for all events including outside of the prompt peak, which then could then be used for background subtraction.

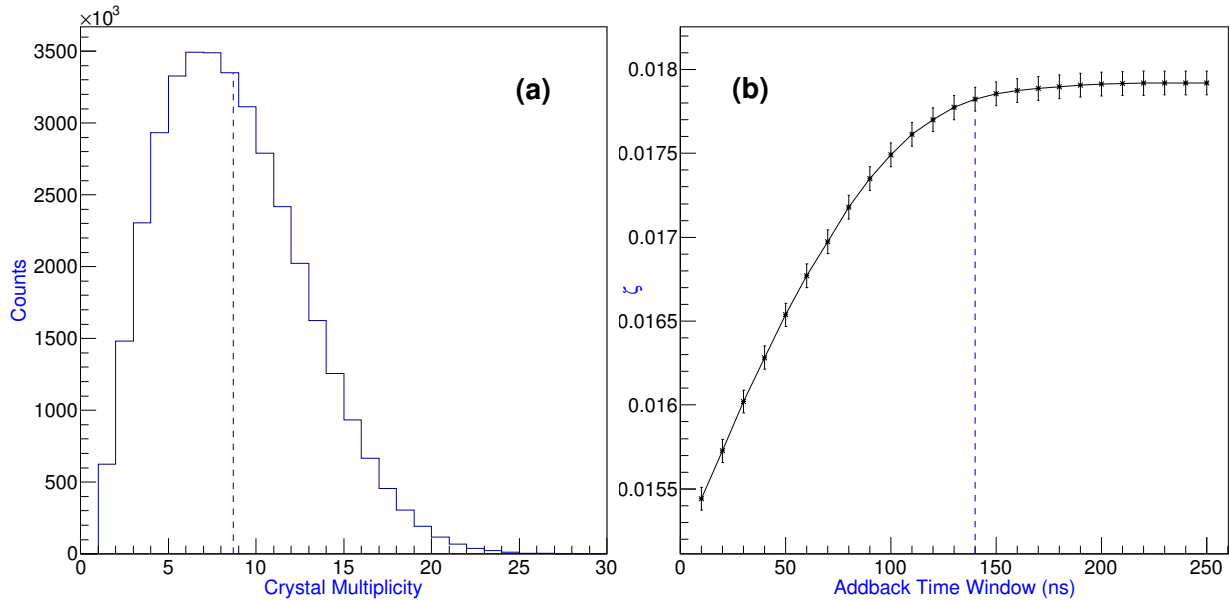


Figure 5.14: (a) Crystal multiplicity of CAGRA, only events within the prompt peak are included in Figure 5.5. The blue line shows the average multiplicity = 8.7 (b) Plotted  $\zeta$  vs time gate width. The blue dashed line here shows the chosen time gate for addback algorithm.

The time difference between each  $\gamma$ -event was taken, then only events within a specified time window were summed. To determine which addback time window was optimum, the Figure of Merit from Equation 5.14 was used. Figure 5.14(b) shows the Figure of Merit calculated from the 1173.2-keV peak in  $^{60}\text{Co}$  as a function of the addback time window. There are 3 distinct regions, initially  $\zeta$  increases with an increase in the time window. Then there is a cross over region where addback becomes less probable and random coincidences start to play an increasing role. At large time windows,  $\zeta$  plateaus. In this region further increase of the time window only increases the probability of adding random coincidences to the addback sum. Therefore, to maximise complete addback summation but reducing contribution from background, the optimum time window was chosen to lay inside the midpoint of the crossover region. This was at 140 ns and is illustrated by the blue dashed line in Figure 5.14(b).

Further characterisation of the addback performance was achieved by plotting the percentage increase of counts as a function of  $\gamma$ -ray energy. This is shown in Figure 5.15(b),

again using data points from  $^{60}\text{Co}$ ,  $^{56}\text{Co}$  and  $^{152}\text{Eu}$ . The trend shown in this figure is consistent with the physical description in comparison with the TIGRESS simulations. The number of crystals that contribute to each addback event, referred to here as addback fold, was also investigated. This is plotted in Figure 5.15(a), in which shows lower addback folds are more probable. Physically this represents the larger probability of  $\gamma$  rays escaping the clover detector vs depositing its full energy over multiple interactions.

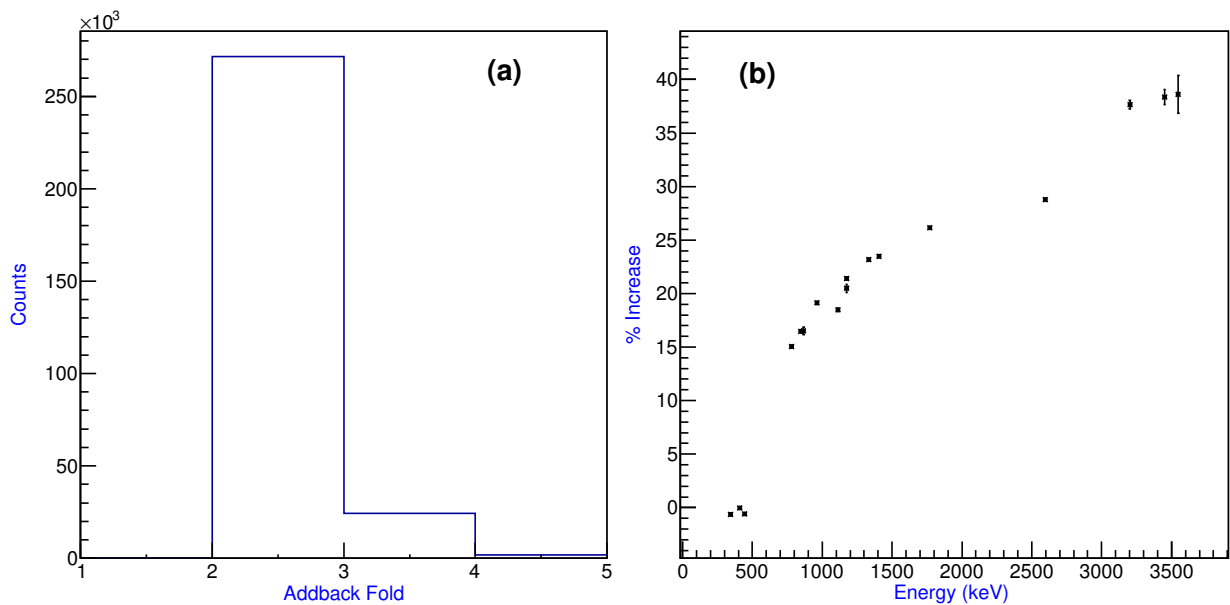


Figure 5.15: (a) The addback fold, i.e. the number of crystals triggered per addback event, showing that majority of addback events require the sum of only two crystals. (b) Shows the percentage increase of counts with addback implemented compared to without. Addback starts to become more efficient as energy increases, due to increase in Compton scattering and pair production.

## 5.9 BGO Suppression

This section details the testing and implementation results for the BGO suppression capabilities of CAGRA.

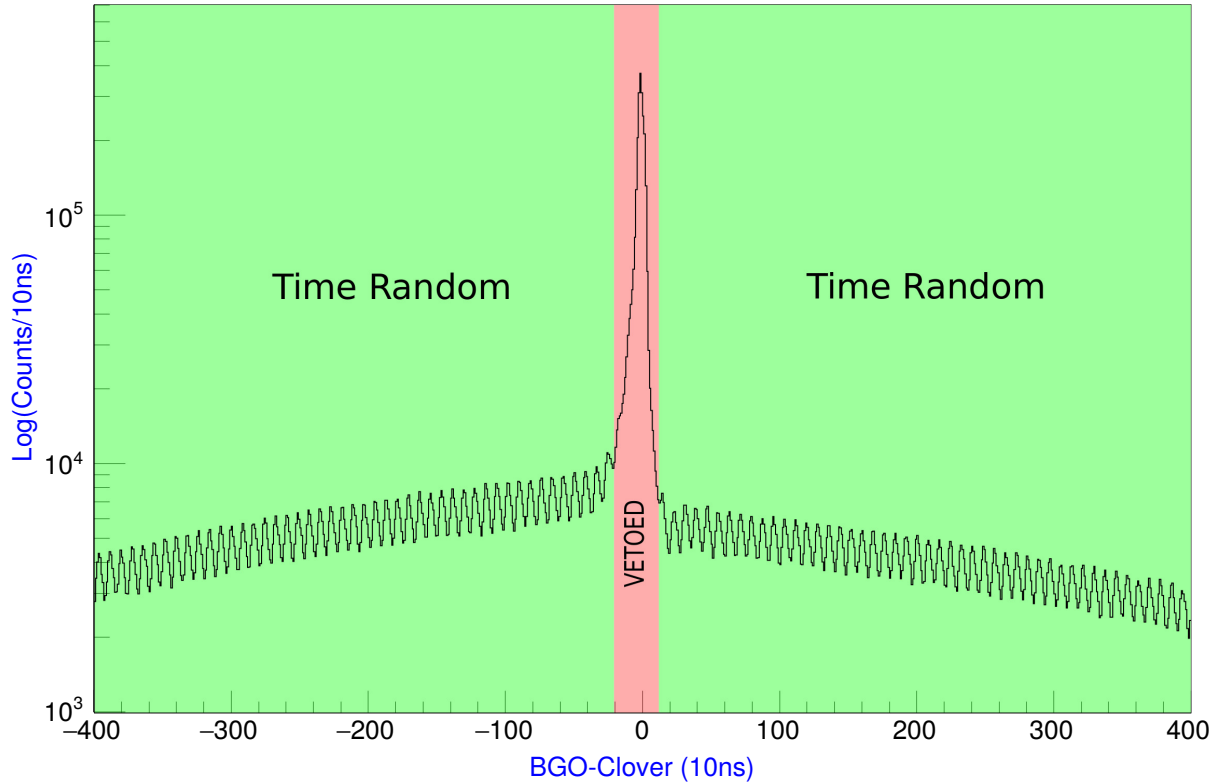


Figure 5.16: Timestamp difference between any clover crystal and its corresponding BGO suppressor. The green region shows time random coincidences. The red region shows the true prompt coincidence, these are events with incomplete energy deposition within a clover detector. These events were therefore vetoed.

First, the timing between any clover crystal and its corresponding BGO was characterised. This is shown in Figure 5.16, here the green region shows time random coincidences between any clover crystal and its BGO suppressor. These events coincide with either full energy deposition within a clover detector, or a Compton scattered event which escaped both the clover and BGO detector. These two cases can't be distinguished, therefore all green events are accepted. The red region shows how the true prompt coincidence sits on top of a time random background. Again, the two cases can't be distinguished on an event by event basis. Therefore, all these events were vetoed in the analysis of the BGO suppression.

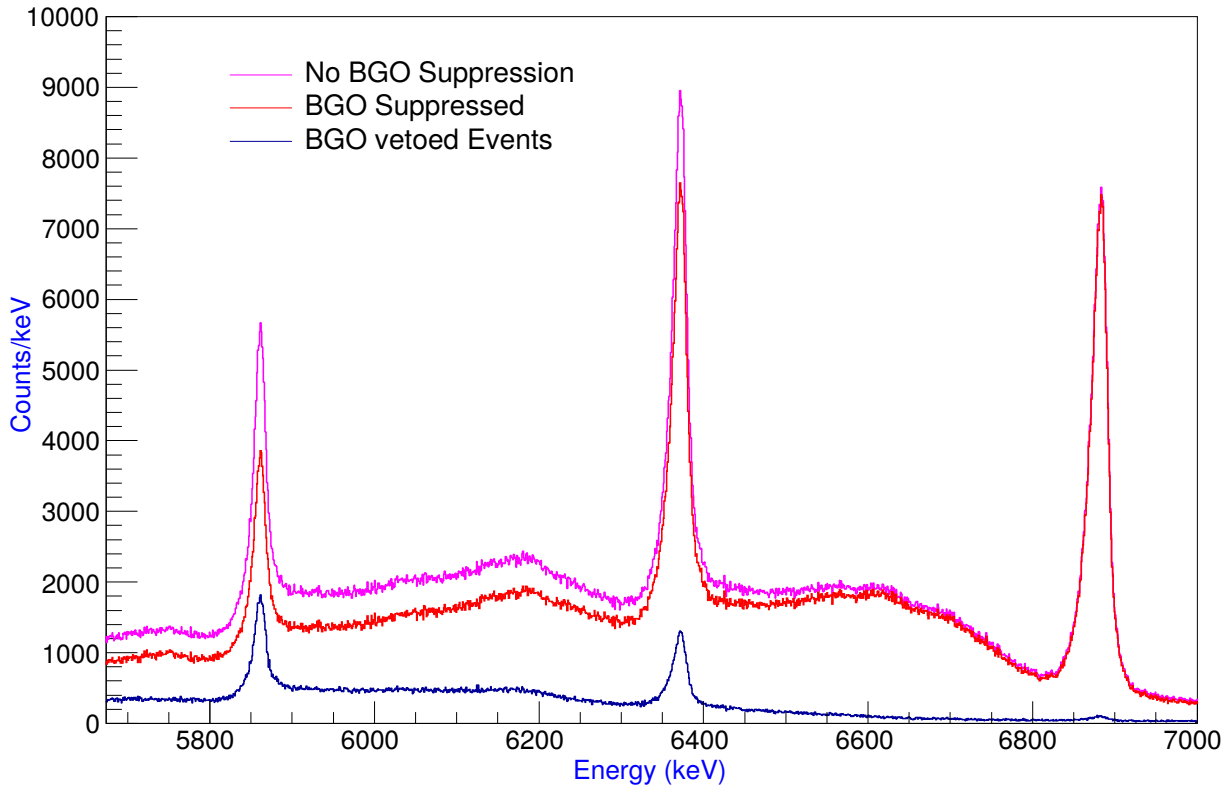


Figure 5.17: Comparison of BGO suppression implementation. The raw and calibrated HPGe  $\gamma$ -ray spectrum is drawn in magenta, BGO vetoed spectrum in red and the events that were vetoed are in blue. The photopeak is not suppressed which is promising, however there is limited success in suppressing the Compton distribution.

The results of the BGO suppression implementation can be seen in Figure 5.17. This was for the  $J^\pi=3^-$  to  $J^\pi=0^+$  ground-state decay in  $^{28}\text{Si}$ . This did show some promising signs, since the first and second escape peaks are preferentially vetoed. This is shown by the distribution in blue, which are only BGO vetoed events. The magenta distribution represents the raw  $\gamma$ -ray spectra. Comparing this to the BGO suppressed distribution in red, there is insignificant BGO suppression at the full energy photo-peak. This is the desired response for BGO suppression. However, this is also the case for the Compton distribution down to the first escape peak. If the BGO suppression was working as desired these events should be suppressed. Events below the first escape peak have a significant BGO suppression, which again shown some effectiveness of its implementation.

These performance issues may be explained by the quality of the charge collection seen in the BGO spectrum. Figure 5.18 shows one example spectrum from a clover detector. The events shown in this BGO spectrum was in coincidence with prompt HPGe crystals events of the same clover detector, i.e. events inside the BGO veto gate in Figure 5.16. Even though the resolution of HPGe is far superior to the typical resolution of BGO detectors, there should still be a visible spectrum. However, the results from Figure 5.18 seems to be noise or a spectrum with very bad energy resolution. The reason for this detector behaviour is still unknown and the same response was seen for all the other BGO crystals. For this reason the BGO suppression was unfortunately not reliable enough to be used for the final analysis.

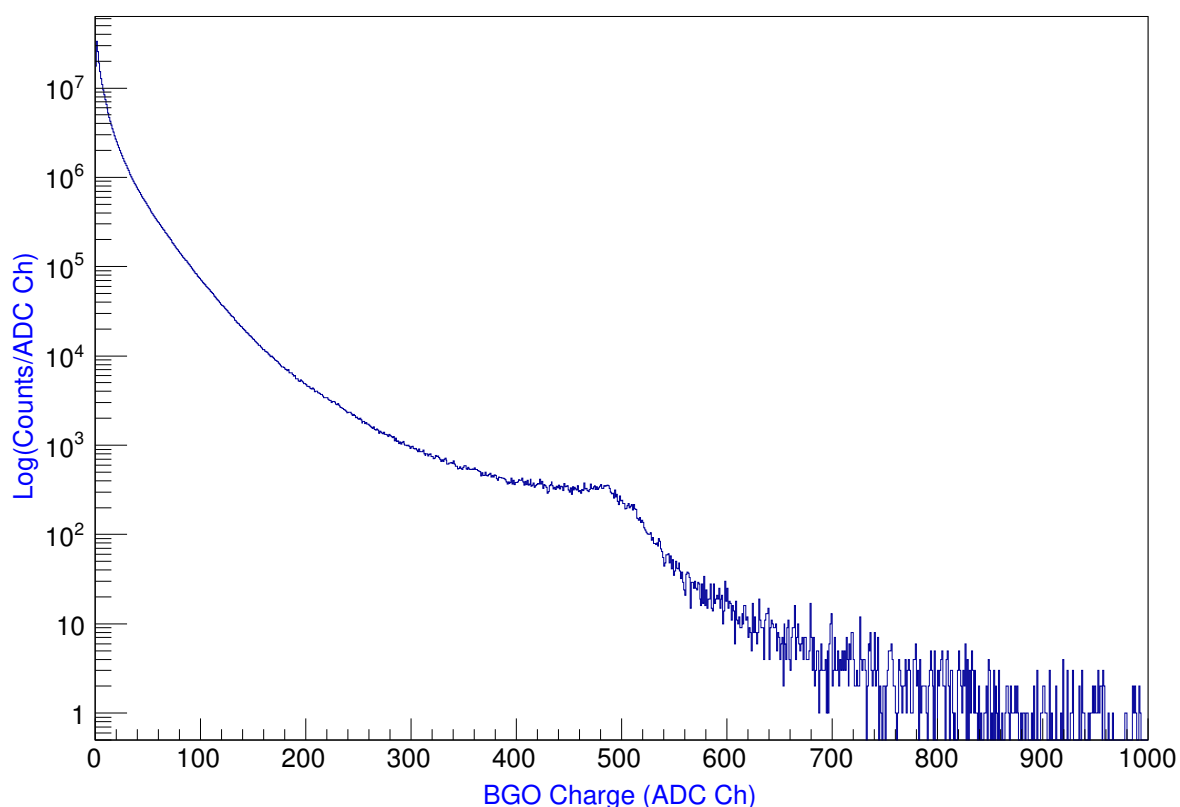


Figure 5.18: Example charge spectrum from one BGO detector showing atypical response. For this reason the BGO suppression capabilities of CAGRA was not utilised.

## 5.10 $\gamma$ -Ex Background Subtraction

The prompt CAGRA-GR coincident events sit on top of background as previously detailed and so a background subtraction was necessary. This was achieved by producing a  $\gamma$ -Ex coincidence spectra via gating either side of the prompt peak in Figure 5.5 as marked between the red limits. The high and low background spectra were summed and scaled down to the width of the prompt peak gate. This was then subtracted from the true prompt  $\gamma$ -Ex coincidence spectrum. Figure 5.19 shows an example of the effectiveness of this technique. This was produced by gating on the  $J^\pi=3_1^-$  state on the  $\gamma$ -Ex background subtracted spectrum and taking the projection onto the  $\gamma$ -ray energy axis.

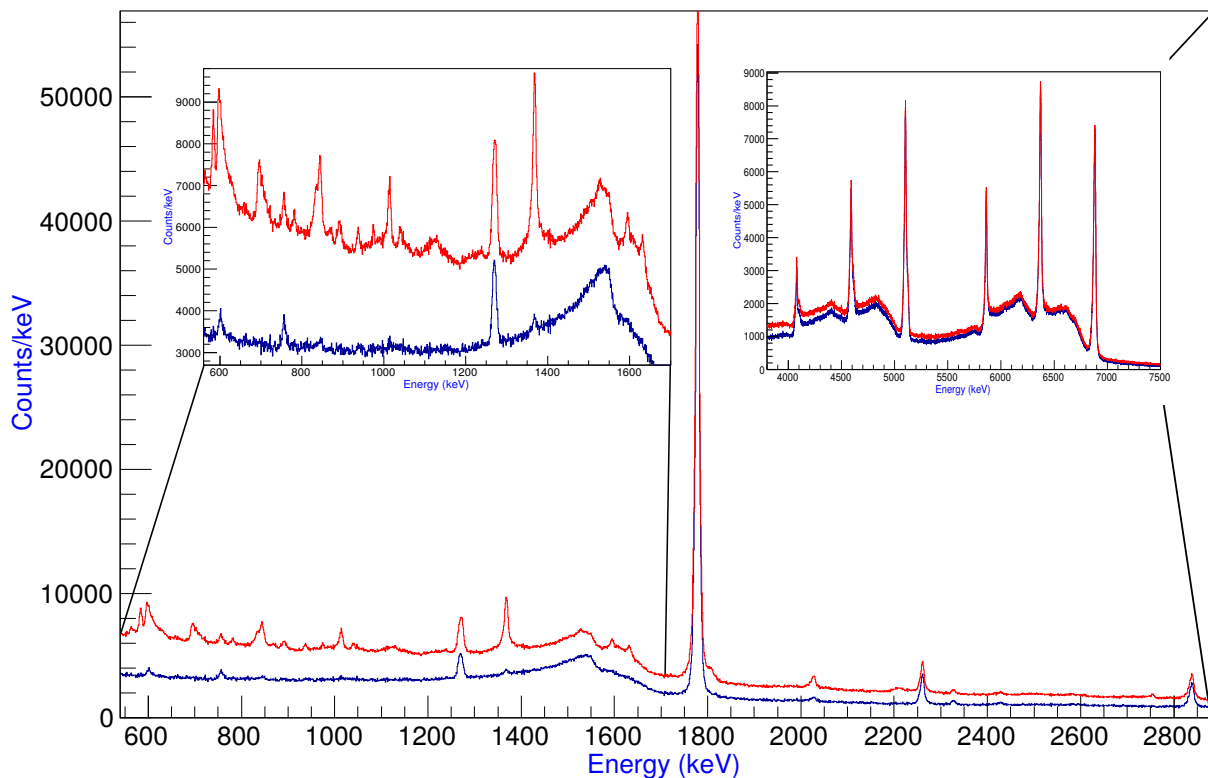


Figure 5.19: Background subtraction: Inserts shows zoomed in spectrum at low energy where the background has been effectively removed. The high energy insert shows minimal background, showing background is focused to lower energy.

The left insert in Figure 5.19 highlights the low energy component, here the background has been effectively removed. The remaining peaks are all accounted for from known  $\gamma$ -ray transitions. The source of the background is not fully understood. However, the most likely sources are neutron related, either from activation of the Al reaction chamber or reactions with the Ge inside of the clover crystals themselves. The  $\text{LaBr}_3$  also have a significant internal activity which could have been incident on the clover detectors. All these possibilities are from time random background events and since the effectiveness of the background subtraction was proven, it was not necessary to fully characterise the precise details of their origin.

From here on, any  $\gamma$ -ray spectrum shown will be background subtracted through this method, unless stated otherwise.

## 5.11 CAGRA $\gamma - \gamma$ Analysis

This section focuses on the results from the  $\gamma$ - $\gamma$  analysis implementation of CAGRA. The time ordered CAGRA events that met the  $\gamma$ - $\gamma$  criteria were filled to a dedicated vector associated to each successful focal plane event. The criteria were as follows:

- All events were inside the prompt peak
- Two correlated  $\gamma$  events can not be from the same clover
- If conditions for addback were met, the timestamp was associated with the event with the highest energy
- Inside the excitation energy gate of interest

This allowed a symmetrical  $\gamma$ - $\gamma$  coincidence spectra to be created. Only  $\gamma$ - $\gamma$  events with multiplicity of two was investigated. Figure 5.20 shows an example case gated on the  $J^\pi = 3_1^-$  state in  $^{28}\text{Si}$ . A gate was applied to the 1778-keV  $J^\pi = 2_1^+$   $\gamma$ -ray transition to the g.s on one axis, events in coincidence should be from the  $J^\pi = 3_1^-$  to the  $J^\pi = 2_1^+$  transition. By projecting onto the opposite axis of the energy gate yields the correlated  $\gamma$  spectrum,

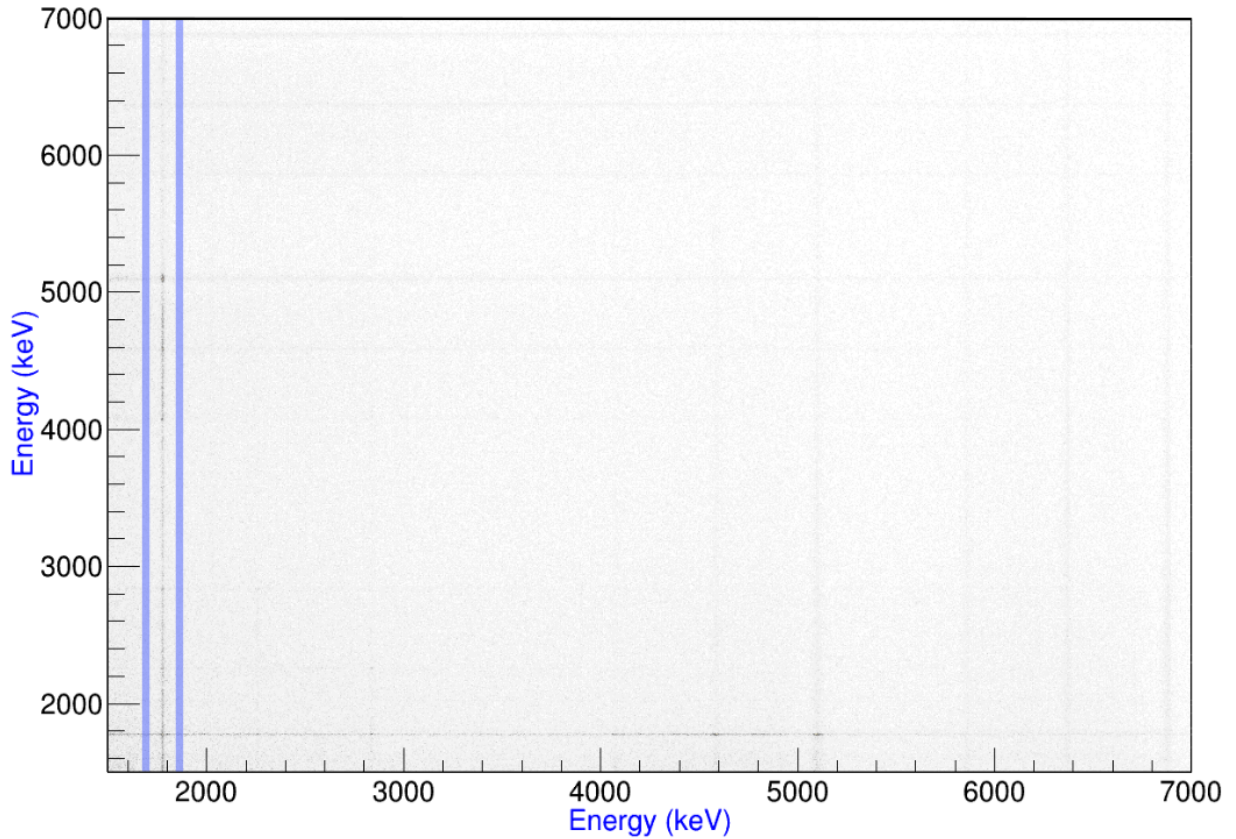


Figure 5.20: Symmetrical  $\gamma$ - $\gamma$  spectrum with multiplicity of two gated on the  $3_1^-$ . The region in blue were the limits used for the background subtraction.

as seen in Figure 5.21(right). Before background subtraction there were significant counts in the 1778-keV peak. This can not be in coincidence with itself and is caused by random background correlations, therefore, a background subtraction was required. This was achieved by placing a background gate either side of the original gate, which are drawn in blue in Figure 5.20. The subtraction of the normalised background spectrum from the main 1778-keV gate can be seen in Figure 5.21(left). The counts of the of the 5098.8-keV peak which feeds the  $2_1^+$  state decreased by 10 % and 50 % for the 1778-keV transition after subtraction. This shows the background subtraction was preferentially subtracting true background.

This was performed on a state with the largest statistics, order of magnitude higher

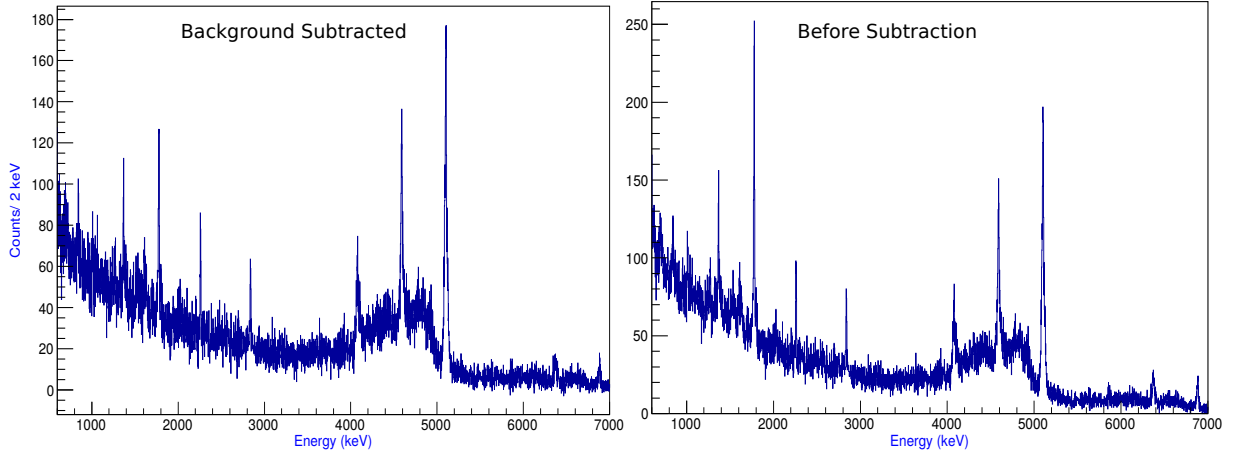


Figure 5.21:  $\gamma$ - $\gamma$  background subtraction gated on the  $J^\pi = 3_1^-$  state and then on the 1778-keV transition. Right figure shows before subtraction and left shows after. After subtraction the 1778-keV transition was significantly subtracted where as the 5098.8-keV was preserved.

than most states in the focal plane. You can see that the  $\gamma - \gamma$  spectra produced still have relatively low statistics. It was still enough conclude the implementation was successful, however when similar analysis was performed on other states no further information could be required because of the significantly low statistics. Therefore, no further  $\gamma - \gamma$  analysis was performed during this research.

## 5.12 LaBr<sub>3</sub> Analysis

The timing of the LaBr<sub>3</sub> detectors were taken via the time difference between the leading edge trigger of the LeCroy FREA module respect to the plastic stop signal at the focal plane. The time of flight of the  $\alpha$ -particles from the cyclotron to the plastic detector is dependent on the path length taken around Grand Raiden. Due to the superior timing capabilities of the LaBr<sub>3</sub> detectors this time dependent path is measurable and will deteriorate the optimum time resolution. The time difference between the rf signal of the cyclotron and the plastic detector triggers were also recorded. This had the same systematic error associated with the path dependent ToF. Therefore, subtracting one from the

other removes this systematic error. This is now essentially the time difference between the rf signal and the LaBr<sub>3</sub> trigger. The subtraction improved the prompt peak resolution from FWHM = 14.2 ns to less than 2 ns.

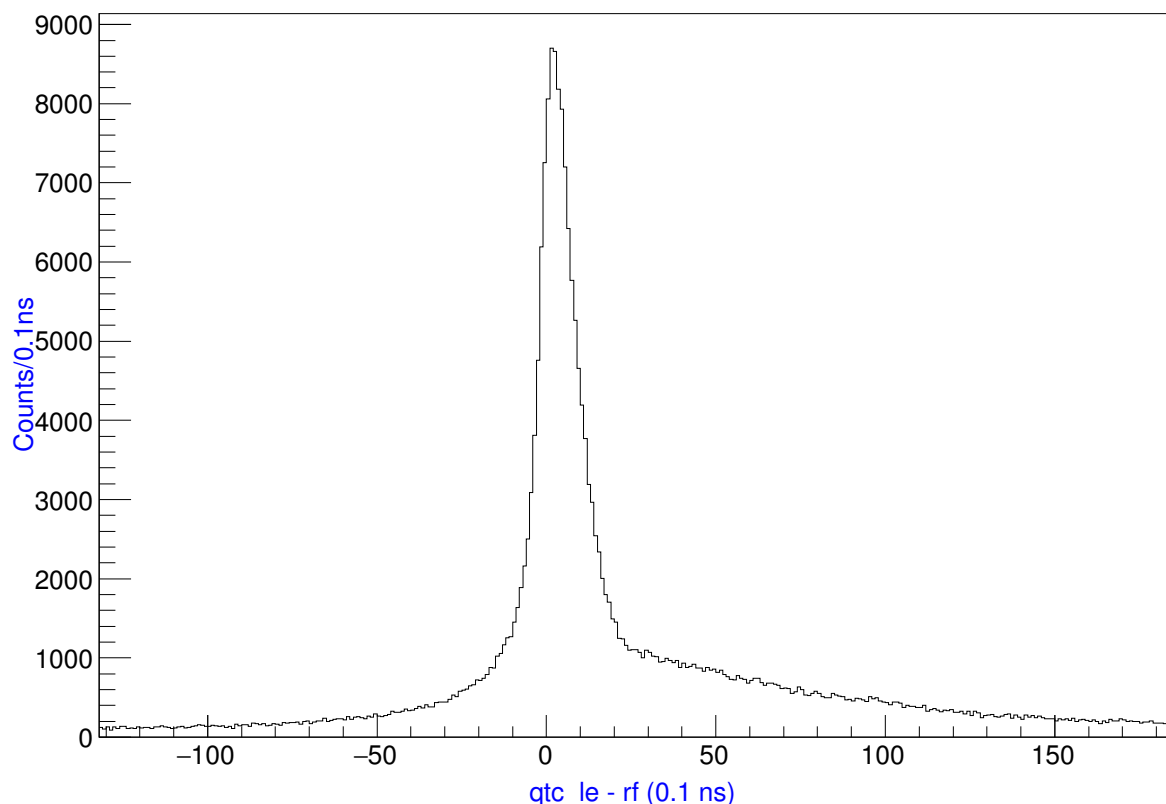


Figure 5.22: LaBr<sub>3</sub> prompt timing spectrum with removed ToF component from Grand Raiden and corrected for time walk. Here, each bin corresponds to approximately 0.1 ns. The fitted FWHM yielded a prompt time resolution of  $1.278 \pm 0.01$  ns.

Next, the time walk corrections had to be implemented. The time taken to reach the maximum pulse height is time independent. Therefore, since leading edge timing uses a fixed trigger point, the timing is dependent on the  $\gamma$ -ray energy or pulse height. This also has an added effect of smearing out the prompt timing resolution. This can be removed simply by fitting the time-energy dependence, then shifting the timing on an event by event basis depending on the energy detected. An exponential fit was applied and implemented into the sort code.

All of this analysis was achieved by gating on a tight window on  $\gamma$ -ray energy from the 1778-keV transition, which reduced the contribution of time random events. Figure 5.22

shows the prompt timing after all of these corrections implemented and without a gate on the  $\gamma$ -ray energy. This yielded a fitted FWHM =  $12.78 \pm 0.10$  (adc Ch). Each adc channel corresponded to approximately 0.1 ns, therefore a time resolution of  $1.278 \pm 0.01$  ns was achieved. Similar to the clover analysis this was used to create a gated LaBr<sub>3</sub>  $\gamma$ -Energy Vs Ex plot as seen in Figure 5.23.

As expected from the increased efficiency of LaBr<sub>3</sub> compared to clover detectors there are many clear transitions observed in the coincidence spectra. Particularly, at higher energy compared to the clover detectors. However, what is clear is that there is a significant non-linearity issue with the calibration.

Due to the integration method of the four LaBr<sub>3</sub> detectors with the acquisition set-up, which was integrated into the GR-DAQ, there were no source runs available for the energy calibration. Instead, they were calibrated using known transition in <sup>28</sup>Si. This also meant that no absolute efficiency curves could be fitted.

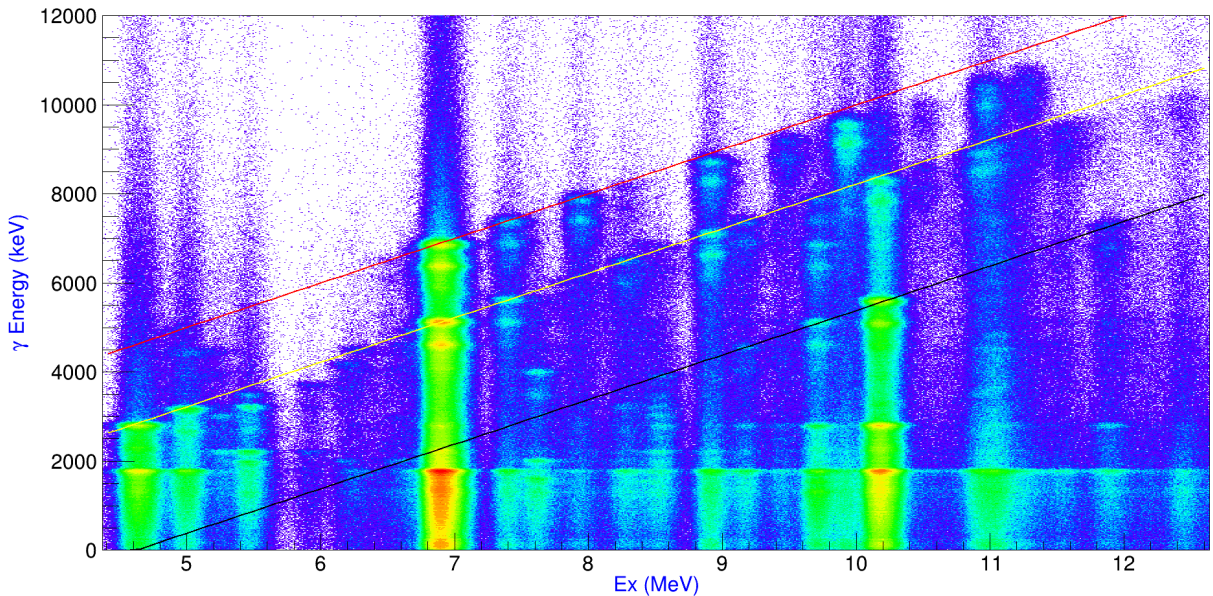


Figure 5.23: Coincident LaBr<sub>3</sub> (Doppler Corrected)  $\gamma$ -Ex spectra created by gating on the prompt peak as seen in Figure 5.22. This spectra shows clear comparisons to the clover coincidence spectra, although there are greater statistics for higher energy transitions due to the increase efficiency.

Projecting Figure 5.23 onto the  $\gamma$ -ray energy axis and then gating on the first  $J^\pi = 4^+$  state at 4.618 MeV yielded Figure 5.24. A very poor resolution was achieved, e.g. fitting

the 2838.29-keV peak yielded a  $\text{FWHM} = 108.17 \pm 0.55$  keV. This was much greater than that achieved by the clover detectors.

It's clear from the energy resolution obtained, precision  $\gamma$ -ray spectroscopy is not practical from these detectors. However, because of the increased efficiency and timing of the LaBr<sub>3</sub>, clover spectra could be produced by gating on LaBr<sub>3</sub>. For example, by placing gates on the LaBr<sub>3</sub> prompt peak and on the 1778-keV transition then looking at the coincident clover spectra, transitions feeding the first  $J^\pi = 2^+$  should be preferentially selected. However, this simply yielded an attenuated clover spectra. This is mostly likely due to the large  $\gamma$ -multiplicity experienced during the CAGRA campaign combined with the poor energy resolution of the LaBr<sub>3</sub> detectors. Therefore, for these reasons no further analysis of the LaBr<sub>3</sub> detectors were undertaken in this research.

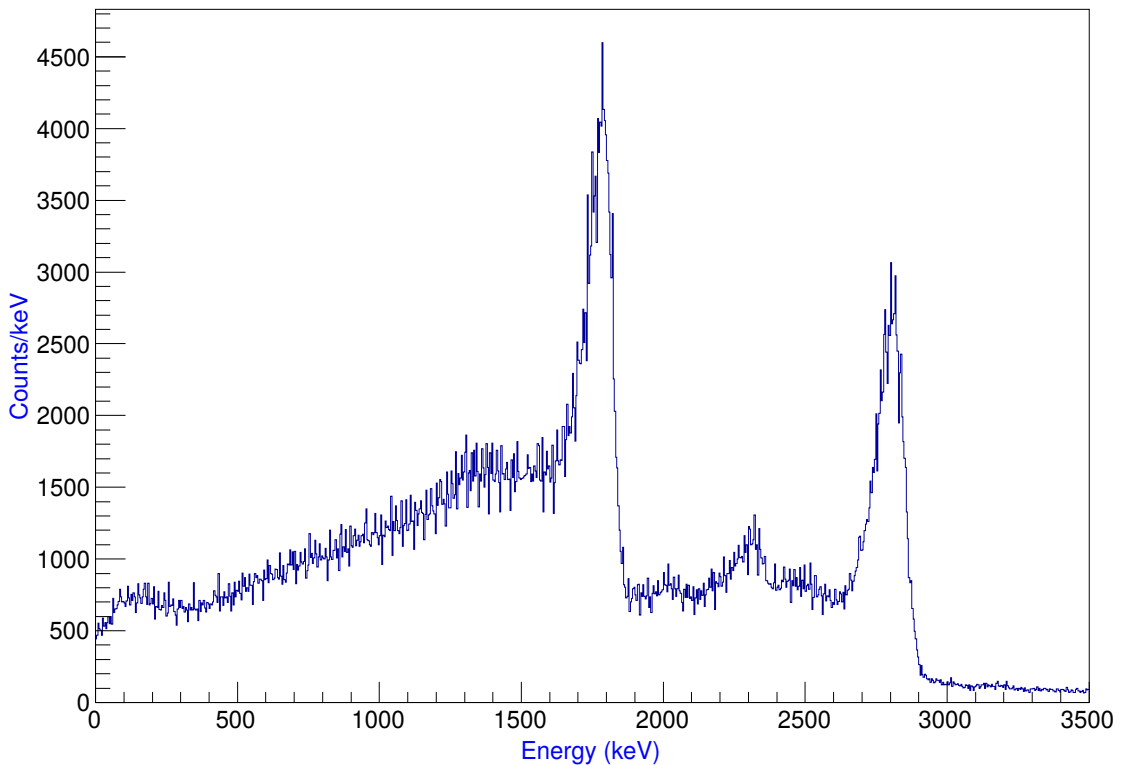


Figure 5.24: LaBr<sub>3</sub>  $\gamma$ -ray energy spectrum produced by gating on the first  $J^\pi = 4^+$  state at  $E_x = 4.618$  MeV in Figure 5.23 and projecting on the y-axis. The spectrum did yield the expected transitions from this state. However, a very poor resolution was achieved,  $\text{FWHM} = 108.17 \pm 0.55$  keV fitted on the 2838.29-keV transition.

# Chapter 6

## Results

This chapter summarises the major findings from this research, detailing all of the states in  $^{28}\text{Si}$  that were populated and their subsequent electromagnetic transitions. Furthermore, all of the relevant analysis for the upper limit of the,  $J^\pi = 4^+$  to the  $J^\pi = 2^+$ , in-band transition strength from the proposed SD band will be discussed.

### 6.1 $\gamma$ -Ex coincidence

Figure 6.1 shows the  $\gamma$ -Ex coincidence spectrum, here the  $\gamma$ -ray energy is with addback and is Doppler corrected. This spectra was also background subtracted, as discussed in the previous chapter. The red line shows transitions to the g.s, yellow to the  $J^\pi = 2_1^+$  state and black to the  $J^\pi = 4_1^+$  in  $^{28}\text{Si}$ . By placing gates on excitation energy and projecting onto the  $\gamma$ -energy axis, direct  $\gamma$ -decay from that state and subsequent cascades could be studied.

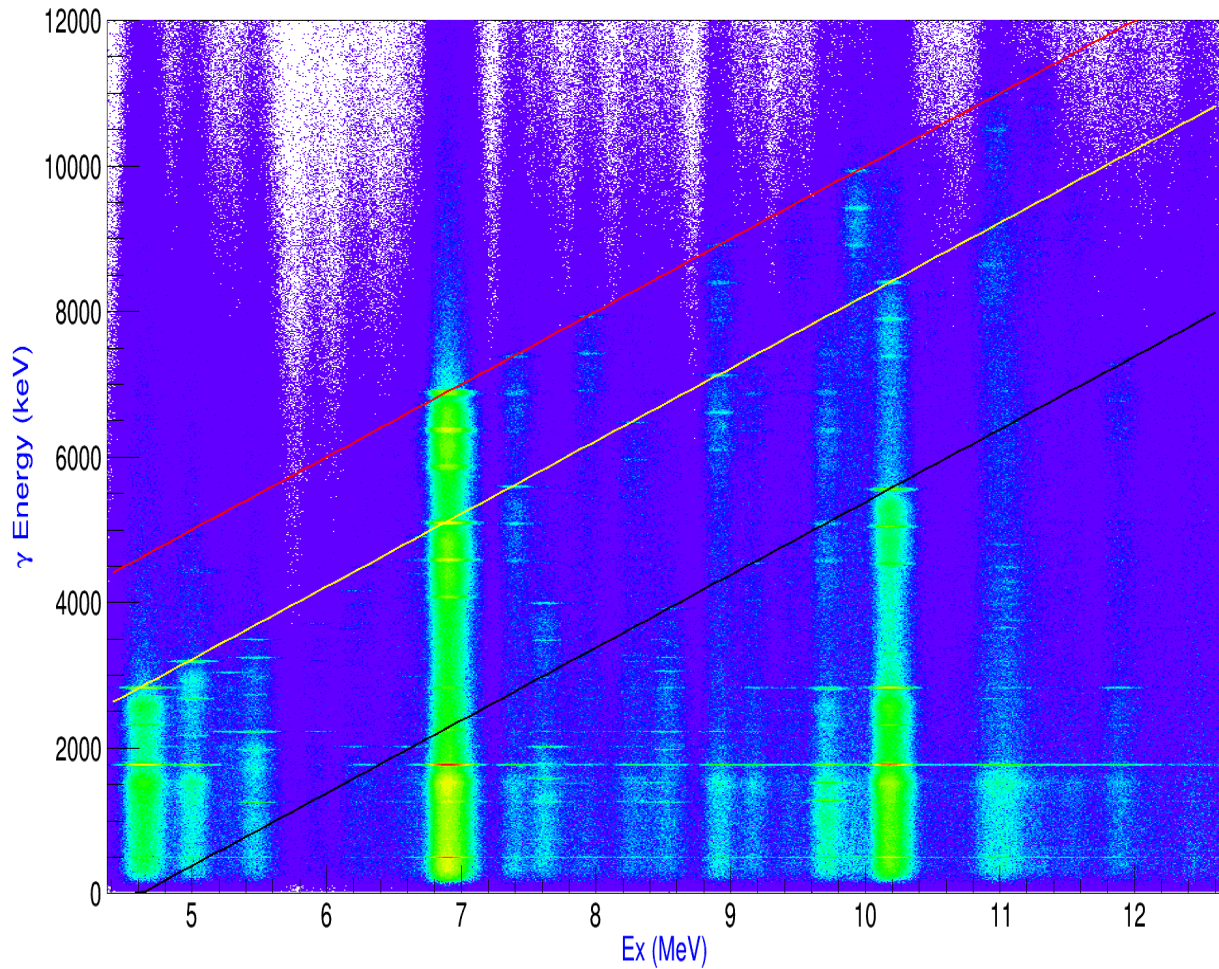


Figure 6.1:  $\gamma$ -Ex coincidence spectrum. The  $\gamma$ -ray energy is with addback and Doppler corrected. This spectra was also background subtracted as discussed in the previous chapter. The red line shows transitions to the g.s, the yellow to the  $2_1^+$  state and black is to the  $4_1^+$  state in  $^{28}\text{Si}$ . By placing gates on excitation energy and projecting onto  $\gamma$ -energy, direct  $\gamma$ -decay from that state and subsequent cascades could be studied.

The projection of the  $\gamma$ -Ex coincidence spectrum, Figure 6.1, onto the excitation energy axis then yields a coincident focal plane spectrum, as seen in Figure 6.2. In the proceeding analysis, each state was then identified and labelled alphabetically, as summarised in Table 6.1.

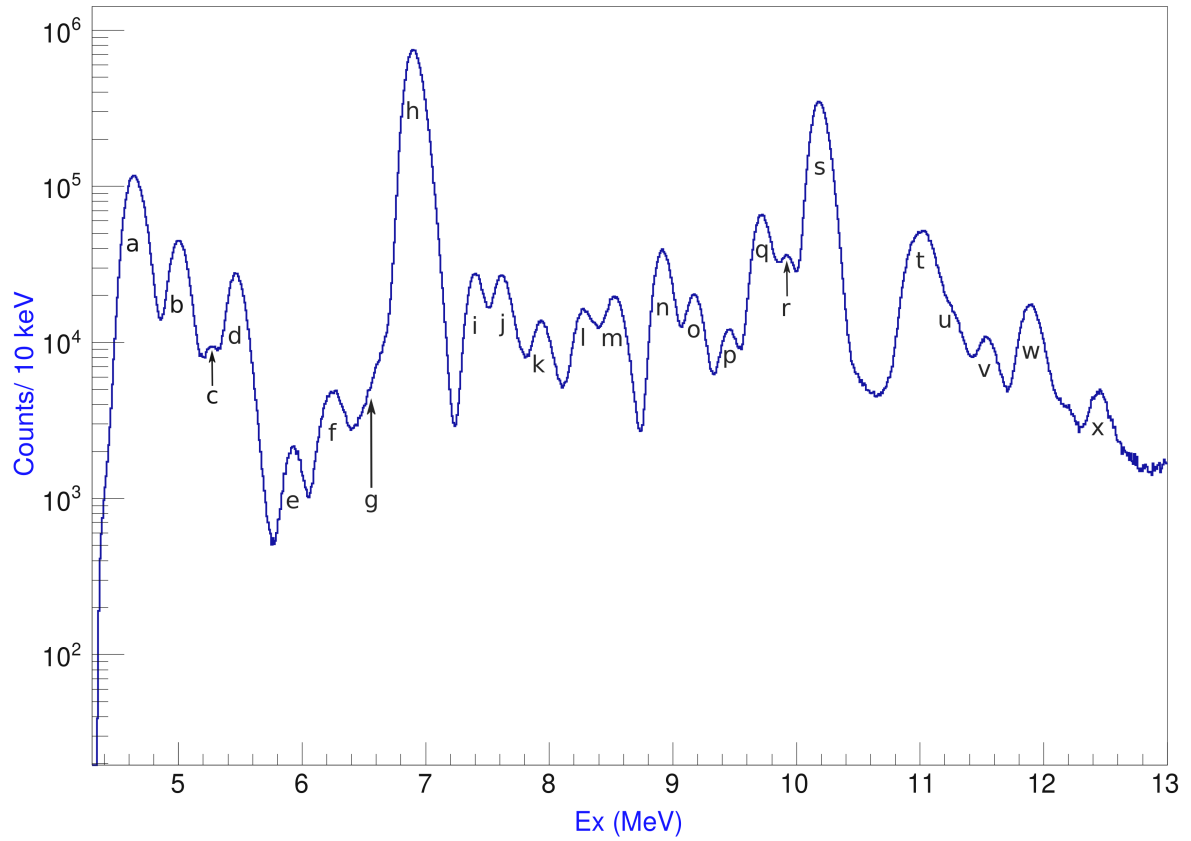


Figure 6.2: Coincident focal plane spectrum, produced by projecting onto the excitation axis on Figure 6.1. See Table 6.1 for information of each state labelled.

The states with known assignments to rotational bands have been summarised in Figure 6.3 (Brenneisen et al., 1995) and (Glatz et al., 1981b). Here, states labelled in blue were directly populated and observed in this research.

Table 6.1: All experimentally observed states, labels correspond to peaks in Figure 6.2.

Label	Si-Isotope	Spin	Parity	Ex (MeV)
a	28	4	+	4.61786
b	28	0	+	4.97992
c	30	4	+	5.27937
d	30	3	-	5.4875
e	30	4	+	5.95073
f	28	3	+	6.27620
	29	$\frac{7}{2}$	-	6.19287
g	28	0	+	6.69074
h	28	3	-	6.87879
	28	4	+	6.88765
i	28	2	+	7.38059
	28	2	+	7.41626
j	29	$(\frac{5}{2}, \frac{7}{2})$	(-)	7.6221
k	28	2	+	7.93345
l	28	2	(+)	8.25874
m	28	6	+	8.54356
	30	3	-	8.5540
n	28	1	-	8.9048
o	28	(4)	(+)	9.16468
p	28	4	+	9.41717
q	28	(5)	(-)	9.70234
r	28	1	-	9.9292
s	28	(3)	(-)	10.1816
	28	(5,3)	(-)	10.1896
t	28	(3)	(-)	10.9156
	28	(4)	(+)	10.944
u	28	(3)	(-)	11.178
v	28	(6)	(-)	11.576

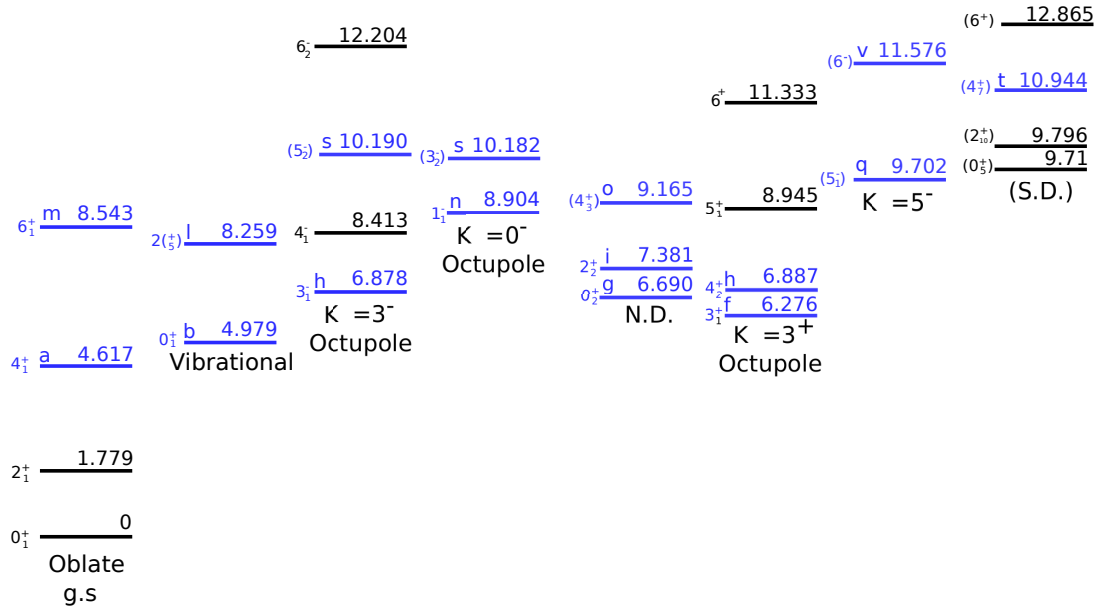


Figure 6.3: Observed rotational bands level scheme. The states coloured in blue were directly observed in this research and their labels correspond to the peaks in Figure 6.2.

## 6.2 Ground-state & $\beta$ band

The excitation of the oblate ground-state band was expected as the reaction mechanism should preference collective rotational excitations. The first and second excited states in  $^{28}\text{Si}$ ,  $J^\pi=2_1^+$  and  $J^\pi=4_1^+$ , belong to the g.s band and will be strongly coupled to the ground state. The  $J^\pi=2_1^+$  state at 1.779 MeV was outside of the focal plane acceptance and therefore was not observed. This was done to ensure the focal plane was completely blind to the elastic channel, which would have destroyed the focal plane detectors. The  $J^\pi=4_1^+$  state at 4.618 MeV was just inside of the focal plane acceptance and was directly observed.

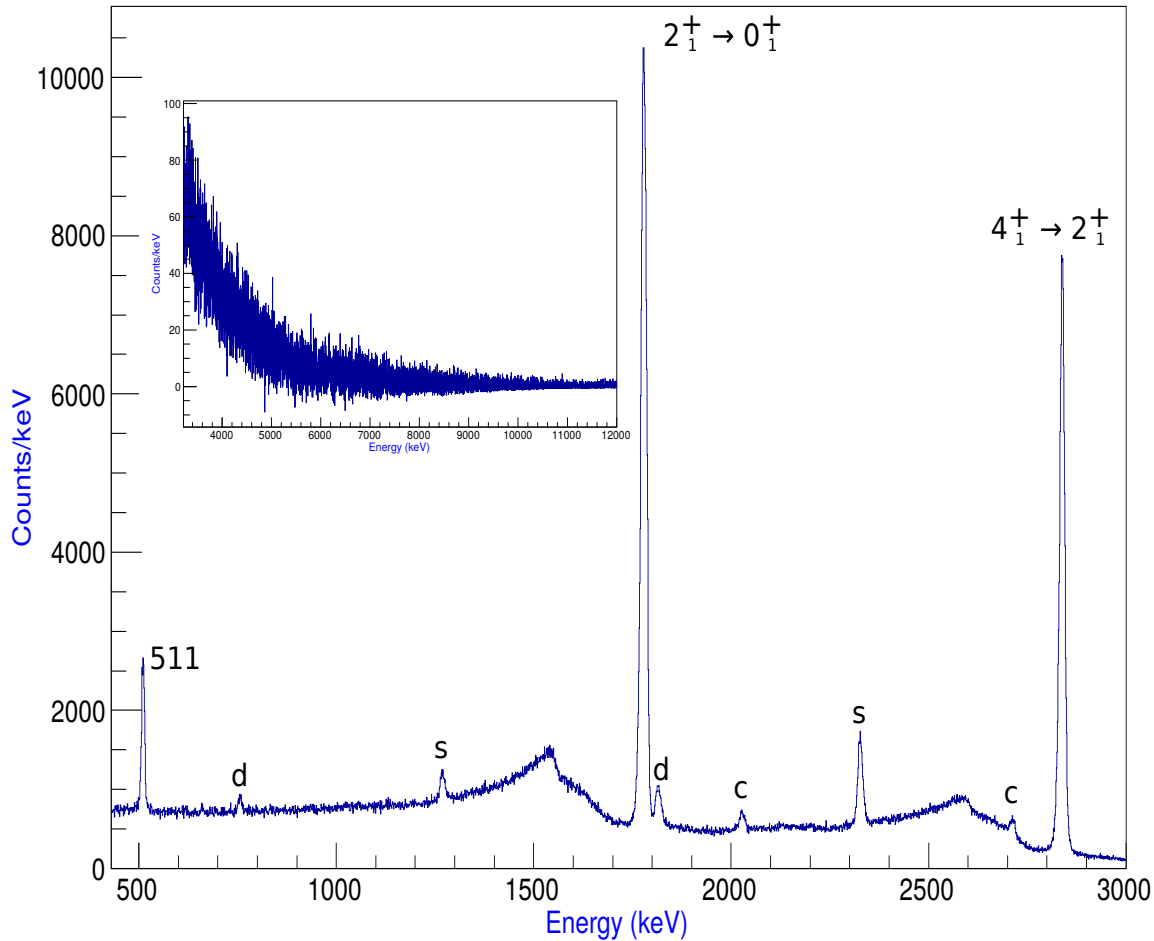


Figure 6.4:  $\gamma$ -ray spectrum for the  $J^\pi=4_1^+$  state, at 4617.86 keV, belonging to the g.s oblate rotational band. The  $J^\pi=4_1^+$  to  $J^\pi=2_1^+$ , at 1779.030 keV, in-band transition is well resolved. The subsequent cascade decay from the  $J^\pi=2_1^+$  to the ground-state is also seen. The single escape are identified by s, double escape by d and contaminants are labelled c.

The  $\gamma$ -ray spectrum for the  $J^\pi=4_1^+$  state is shown in Figure 6.4. The in-band 2838.29-keV transition to the  $J^\pi=2_1^+$  state of the oblate ground-state band can be clearly seen. This spectrum was produced by gating on state, a, in Figure 6.2 and projecting onto the  $\gamma$ -ray energy axis. Where, the in-band  $J^\pi=4_1^+$  to  $J^\pi=2_1^+$  transition with expected energy of 2838.29 keV was observed at  $2838.10 \pm 0.02$  keV. The small discrepancy is due to the performance of the rate dependent shift correction and the Doppler correction accuracy, as previously discussed. The fitted FWHM was 15.68 keV ( 0.56 %) which is significantly large for this energy, but still can be easily identified and resolved. The

subsequent cascade decay from the gated  $J^\pi=4_1^+$  was also measured, which was the  $J^\pi=2_1^+$  to the ground-state transition at 1778.97 keV. The  $J^\pi = 4^+$  and the  $J^\pi = 2^+$  have  $T_{\frac{1}{2}}$  of 37 and 475 fs respectively. These timescales are well within the prompt time resolution of the  $\alpha$ - $\gamma$  coincidence timing. Furthermore, the longest known half-life in  $^{28}\text{Si}$  is 4 ps, which is still well within its time resolution. Therefore, in general all measured cascades were expected to be in coincidence, if detected. The insert in Figure 6.4 shows the high energy region of the same spectrum, where an exponentially decaying background is evident. This demonstrates the success of the particle- $\gamma$  coincident technique implementation, proving that there is no significant background from outside of the excitation energy gate. It is also further evidence for the effectiveness of the prompt timing background subtraction which was used.

There was a minor contaminant observed in this spectrum from  $^{29}\text{Si}$ , which has 4.7% natural abundance. The  $J^\pi=(\frac{9}{2}^+)$  state at 4741.1 keV was also populated within this gate. The known transitions originating from this state of 2712.8-keV and 2028.09-keV accounted for the two observed contaminant peaks.

### 6.3 Octupole Collectivity

The first and most obvious unexpected result of this experiment was the enhanced excitation of octupole degrees of freedom. The two strongest peaks in Figure 6.2 both belong to known octupole deformed rotational bands. Firstly, the peak labelled h was identified as the band head of the  $K^\pi=3^-$  rotational band.

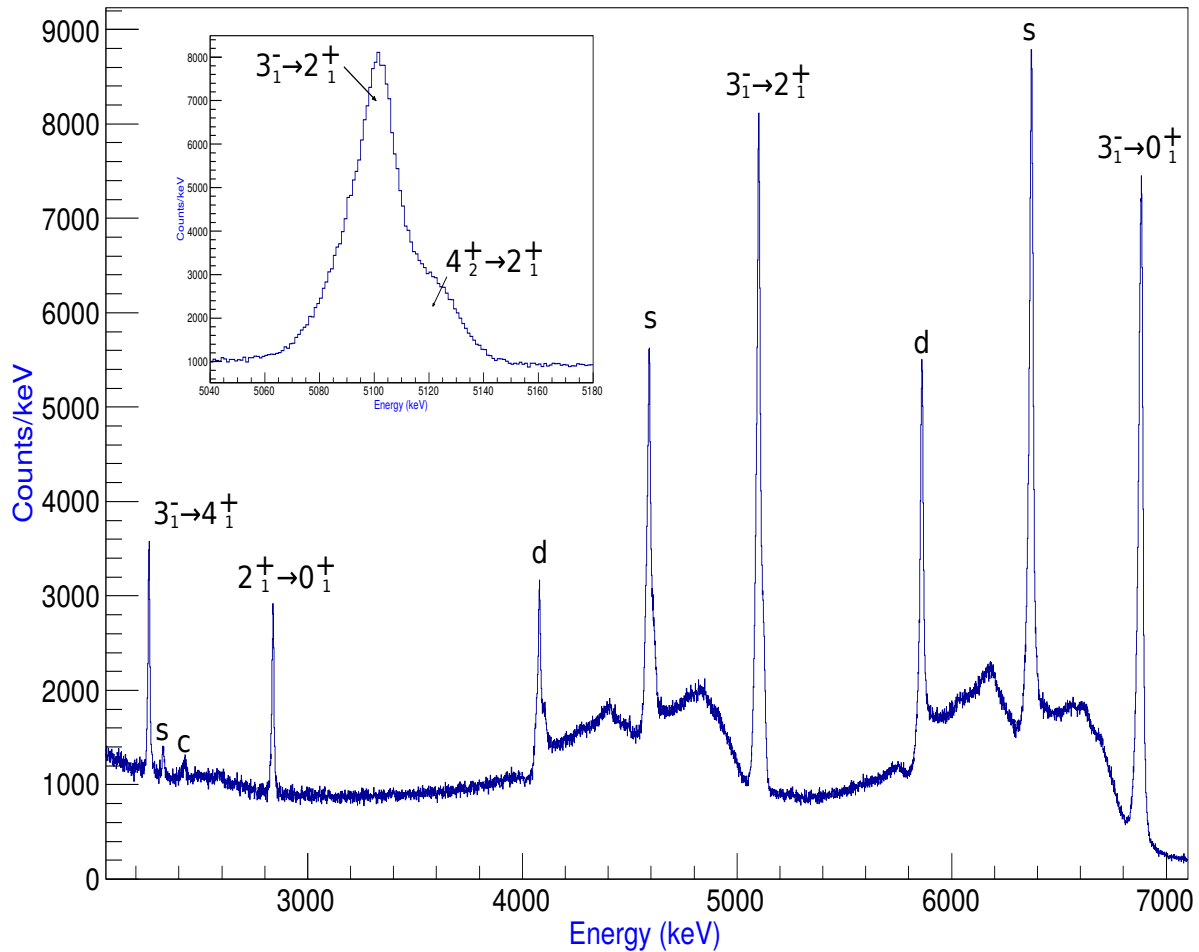


Figure 6.5:  $\gamma$ -ray spectrum for the  $J^\pi=3_1^-$  band head of the  $K^\pi=3_1^-$  octupole rotational band at 6878.79 keV. A closely lying state,  $J^\pi=4_2^+$ , at 6887.65 keV was also populated. The insert shows two overlapping transitions from each of the states to the  $J^\pi=2_1^+$  state at 1779.030 keV.

Figure 6.5 shows the  $\gamma$ -ray spectrum for this gate. The  $J^\pi=3_1^-$  to g.s  $\gamma$  transition of 6877.0 keV was observed and was a unique identifier of the  $K^\pi=3_1^-$  band-head with  $I_\gamma = 100$ . The next most probable transition was the  $J^\pi=3_1^-$  to  $J^\pi=2_1^+$  transition at 5098.8 keV. However, on closer inspection it is clear that there are two overlapping transitions in this region, as shown in the insert. This higher energy peak was assigned to a  $J^\pi=4_2^+$  state at 6887.65 keV. This state also has a  $\gamma$ -ray transition to the  $J^\pi=2_1^+$  state. The energy difference between the two overlapping transitions is only 8.8 keV, which is narrower than CAGRA's energy resolution at this energy, therefore one peak should be present. This

can be explained by the significantly different half-lives of the two populated states. The  $J^\pi=3_1^-$  state has  $T_{1/2} = 1.9$  ps and the  $J^\pi=4_2^+$  has  $T_{1/2} = 33$  fs. This spectrum was not Doppler corrected because of the long 1.9 ps half-life, as discussed in the Doppler correction section. Therefore, the fast transition from the  $J^\pi=4_2^+$  will be significantly Doppler shifted and Doppler broadened.

The  $J^\pi=3_1^-$  to  $J^\pi=2_1^+$  transition was also observed at 2260.7 keV, further confirming the observation of the  $K^\pi=3_1^-$  band-head.

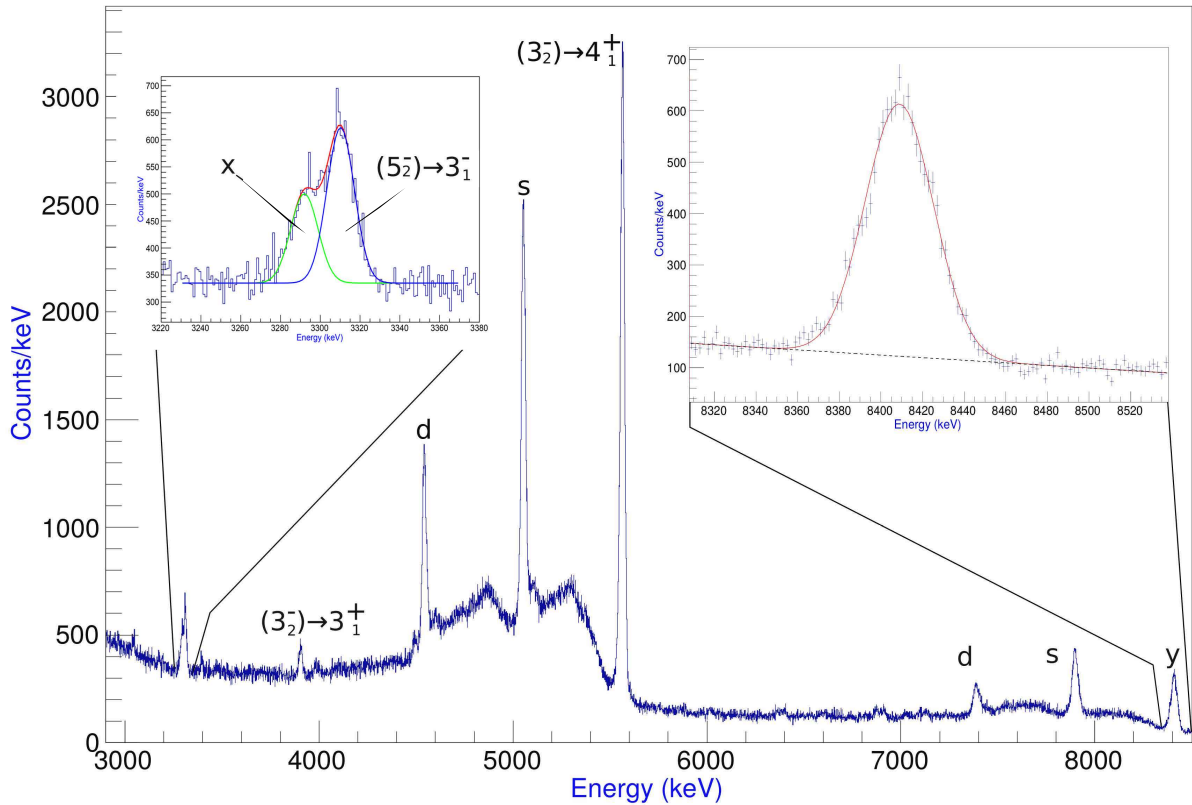


Figure 6.6:  $\gamma$ -ray spectrum for the  $J^\pi=3_2^-$  and  $J^\pi=(5_2^-, 3_3^-)$  states at 10181.60 and 10189.59 keV respectively. The highest energy transition shown in the right insert is a new transition and was assigned to be from the  $J^\pi=3_2^-$  to  $J^\pi=2_1^+$  state at 1779.030 keV. The left insert shows a double peak fitting, yielding centroids at  $3292.0 \pm 0.5$  and  $3310.24 \pm 0.28$  keV. The latter, is a known transition from the,  $J^\pi=3_2^-$  state, at 10189.59 keV. However, the lower energy peak, labelled x, best matches to a new transition from the  $J^\pi=(3_2^-)$  state at 10181.60 keV to the  $J^\pi=4_2^+$  at 6887.65 keV in  $^{28}\text{Si}$ .

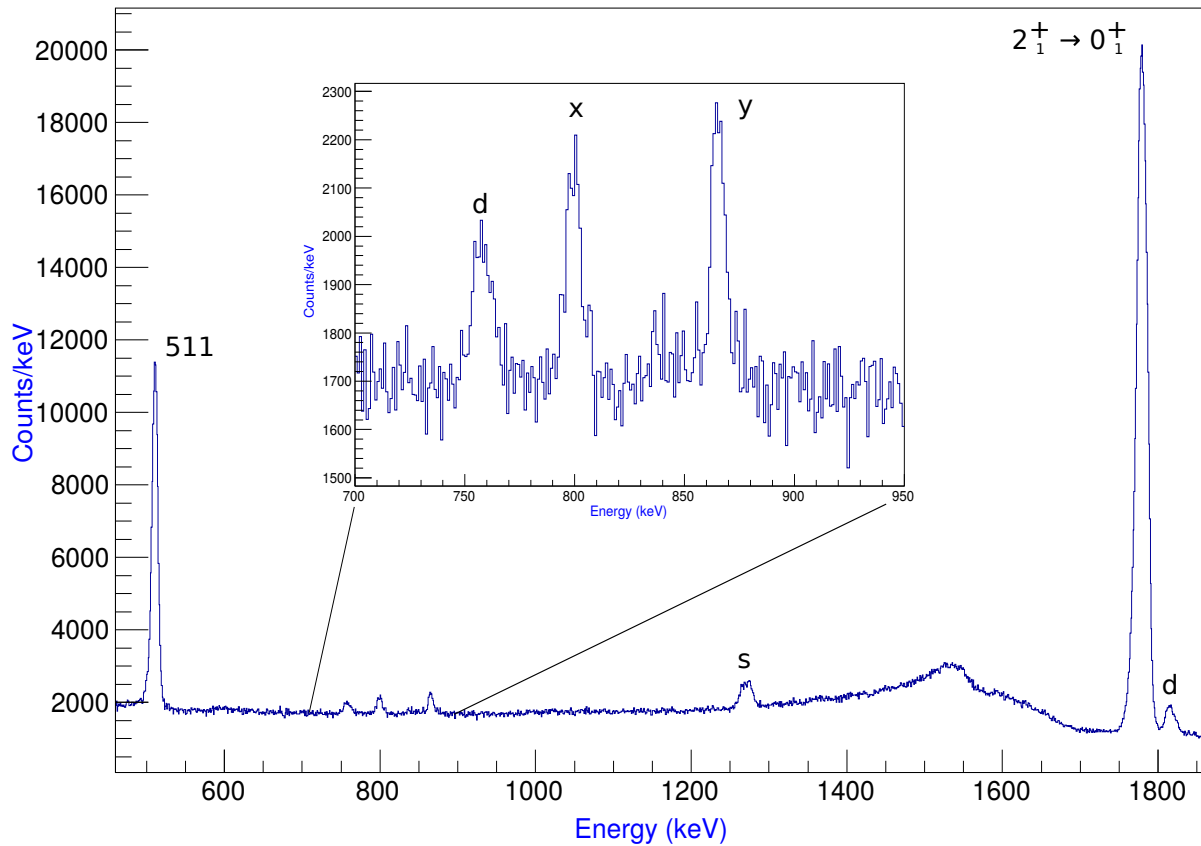


Figure 6.7: Low energy  $\gamma$ -ray spectrum for the  $J^\pi=3_2^-$  and  $J^\pi=(5_2^-, 3_3^-)$  states at 10181.60 and 10189.59 keV respectively. The two peaks labelled x and y, in the insert, are new transitions and were assigned to  $J^\pi=3_2^-$  to  $J^\pi=2_5^+$  at 9381.55 keV and  $J^\pi=3_2^-$  to the  $J^\pi=3_4^+$  at 9315.92 keV, respectively.

The next most populated state in the focal plane spectrum was the peak labelled s in Figure 6.2. The  $\gamma$ -ray spectrum for this gate can be seen in Figure 6.6. The unique 5562.6-keV transition in this spectrum identified a  $J^\pi=(3_2^-)$  state at  $10181.60 \pm 0.12$  keV, decaying to  $J^\pi=4_1^+$  at 4617.86 keV. The next known transition is the 3904.8-keV  $J^\pi=3_2^-$  to  $J^\pi=3_1^+$ , which was also identified. The last known transition is the 1016.9-keV  $J^\pi=3_2^-$  to  $J^\pi=(4_3^+)$  at 9164.68 keV. As can be seen from the low energy region of the spectrum, Figure 6.7, this transition could not be identified. Even though, the tabulated branching ratio for the 1016.9-keV transition was  $I_\gamma = 31.0$  and  $I_\gamma = 10$  for the 3904.8-keV transition. CAGRA's efficiency is greater at lower energy, therefore you expect greater statistics for the 1016.9-keV transition, compared to the 3904.8-keV transition. This either means the

transition was an incorrect assignment, considering that the state it decays to is still a tentative spin assignment. The other possibility is a blind spot around this energy due to the detector response. The latter, would have drastic consequences on the ability to detect the in-band transition from the proposed SD band of interest.

The  $J^\pi=(3_2^-)$  state was assigned to the  $K^\pi=0^-$  octupole rotational band. There were observed transitions within this gate, that are currently unassigned. Firstly, the high energy insert of Figure 6.6 shows a high energy  $\gamma$ -ray. The fitted centroid yielded  $8408.82 \pm 0.23$  keV. Taking into account the recoil energy:

$$E_\gamma = Mc^2 \left( 1 - \sqrt{1 - \frac{2E_\gamma^m}{Mc^2}} \right), \quad (6.1)$$

where,  $M$  is the mass of  $^{28}\text{Si}$  and  $E_\gamma^m$  is the measured  $\gamma$ -ray energy, here  $E_\gamma$  would be the full energy of the  $\gamma$ -ray without any energy loss from the  $^{28}\text{Si}$  recoil. The value of  $E_\gamma$  therefore corresponds to the true transition energy difference. The 8408.82-keV measured  $\gamma$ -ray energy therefore corresponds to a  $8410.16 \pm 0.23$  keV transition. The closest possible transition to this energy was the  $J^\pi=(3_2^-)$  to  $J^\pi=2_1^+$ . The energy difference between the measured and expected transition energy is  $8.410.56 \pm 0.12$  keV. The small discrepancy is well within the energy resolution of CAGRA at this energy. This would also be an E1 transition, which is also a strong characteristic of octupole deformation and could add further information to the characterisation of this band.

Two more new  $\gamma$ -ray transitions were also identified within this gate. This is shown in Figure 6.7, which corresponds to the low energy region of the same spectrum shown in Figure 6.6. The insert shows a zoomed in region which clearly identifies three distinct peaks. The lowest energy peak is simply the double escape from the 1778-keV transition and is seen in all focal plane gates. The other two peaks are however unique to this gate.

Fitting the peaks yielded centroids at  $799.48 \pm 0.20$  keV for peak labelled x, and  $865.36 \pm 0.15$  keV for the peak labelled y. For the x transition, the closest matching transition was from the  $J^\pi=(3_2^-)$  to the  $J^\pi=2_5^+$  state at  $9381.55 \pm 0.12$  keV. The level energy difference here is  $\Delta E = 800.05 \pm 0.17$  keV. This is very close to the measured transition energy and

again well within the energy resolution. The transition labelled y was best matched to  $J^\pi=(3_2^-)$  to the  $J^\pi=3_4^+$  state at  $9315.92 \pm 0.10$  keV. This has a transition energy of  $\Delta E = 865.68 \pm 0.16$  keV and again very close to the measured energy. Both the new x and y transitions would therefore be E1 transitions and again be consistent with a octupole rotational band.

Another state which was attributed to the state s in the focal plane was a  $J^\pi = (5^-, 3^-)$  state at  $10189.59 \pm 0.20$  keV attributed to the  $K^\pi = 3^-$  octupole rotational band. This has only one known  $\gamma$ -ray transition at 3310.4 keV. This is the in-band transition to the  $J^\pi = 3_1^-$  at 6878.79 keV. The low energy insert in Figure 6.6 shows the zoomed in region around this transition. It's clear there are two peaks located in the region of interest. Fitting a double peak to this yielded centroids at  $3292.0 \pm 0.5$  and  $3310.24 \pm 0.28$  keV. The higher energy peak is consistent with the known transition energy from the  $J^\pi = (5^-, 3^-)$  state. The lower energy peak however is best matched to a new transition, from  $J^\pi = (3_2^-)$  at  $10181.60 \pm 0.12$  to  $J^\pi = 4_2^+$  at  $6887.65 \pm 0.1$  keV. The level energy difference here is  $3293.95 \pm 0.16$  keV again close to the measured energy. Therefore, a further transition can be assigned to the  $J^\pi = (3_2^-)$  state, making a total of four new assignments from this one state.

## 6.4 Unnatural parity state

The  $^{28}\text{Si}(\alpha, \alpha')^{28}\text{Si}^*$  reaction should not excite unnatural parity states. However, the population of the  $J^\pi=3_1^+$  at  $6276.20 \pm 0.07$  keV was observed within the gate labelled f, in Figure 6.2. The two known transitions from this state are at  $4496.92 \pm 0.25$  keV ( $J^\pi=3_1^+ \rightarrow J^\pi=2_1^+$ ) and 1658.2 keV ( $J^\pi=3_1^+ \rightarrow J^\pi=2_1^+$ ), in which can be identified from the spectrum in Figure 6.8. The major contaminant in this spectrum is from the  $J^\pi = \frac{7^-}{2}$  state at 6192.8 keV with known transitions, labelled c in Figure 6.8.

The direct population of unnatural parity states were very unexpected from the understanding of the reaction mechanism. However, this has been observed and explained in an analogous situation for the  $J^\pi=3_1^+$  state in  $^{24}\text{Mg}$  (Borg et al., 1979). They used  $^{24}\text{Mg}(\alpha, \alpha')^{24}\text{Mg}^*$  inelastic scattering at 120 MeV. They could only explain the excitation

of the  $J^\pi=3_1^+$  by a multi-step excitation coupled to the  $J^\pi=2_1^+$  of the  $^{24}\text{Mg}$  ground-state band. They confirmed this with coupled-channel calculations. This also required the  $J^\pi=3_1^+$  state to be a member of a strong  $\gamma$ -band. This could be exciting if the same calculation could be done for  $^{28}\text{Si}$  to see if similar characteristics emerge.

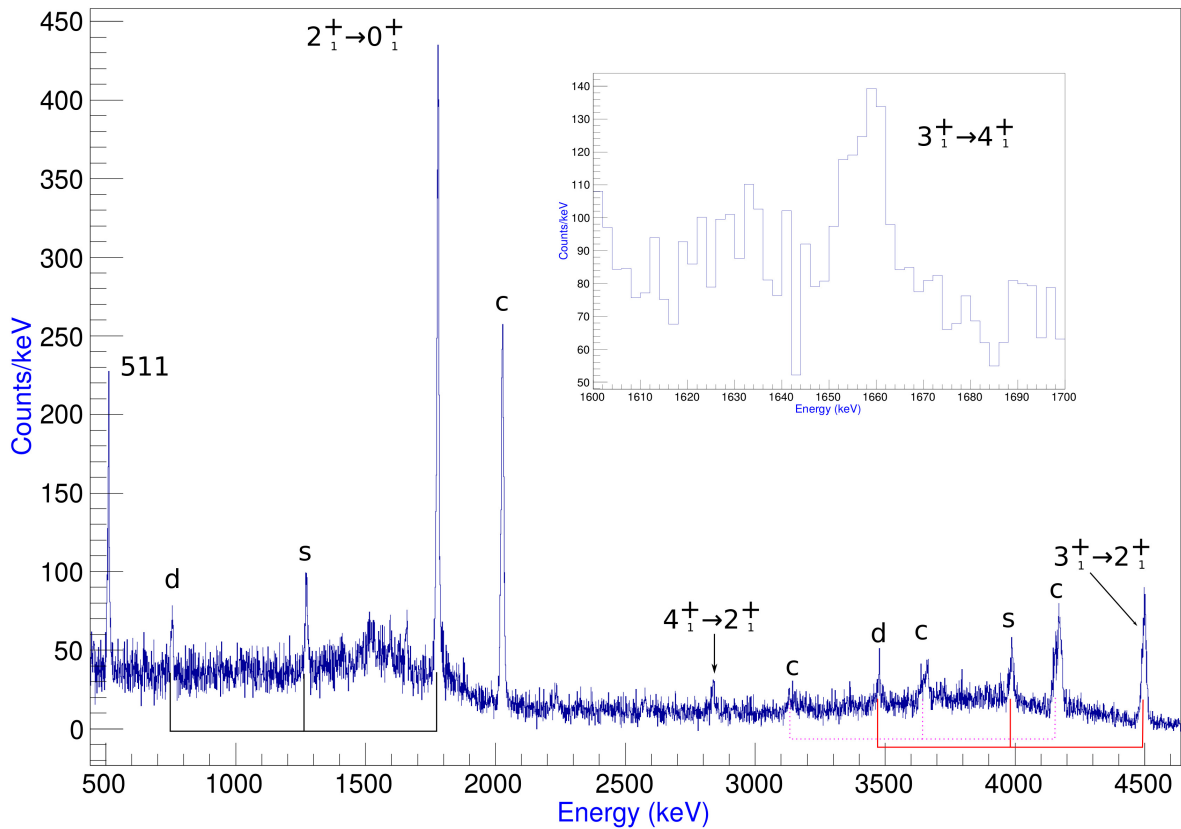


Figure 6.8:  $\gamma$ -ray spectrum for the  $J^\pi=3_1^+$  state at 6276.20 keV. The main transition from this state at 4496.92 keV can be easily identified. The insert shows the other transition from this state at 1658.2 keV. The single and double escape peaks are labelled s and d respectively. The peaks labelled c are known transitions from contaminant Si isotopes.

## 6.5 Unassigned states

The lack of tabulated, detailed  $\gamma$ -ray spectroscopy and increased level density at high excitation makes it very difficult to assign some of the observed transitions to states in  $^{28}\text{Si}$ . The peak labelled w, in Figure 6.2 centered around 11.8 MeV is one such an example. The coincident  $\gamma$ -ray spectrum in Figure 6.9 shows distinct transitions at:  $3309.607 \pm 0.8092$ ,  $3379.123 \pm 1.286$ ,  $5013.292 \pm 0.977$ ,  $5105.487 \pm 0.846$ ,  $7283.338 \pm 0.514$  and  $7360.351 \pm 1.130$  keV. The  $5105.487 \pm 0.846$ -keV transition is most likely a cascade decay from the  $J^\pi = 4_1^+$  at 6887.65 keV and the  $3309.607 \pm 0.8092$  keV transition from the  $J^\pi = (5^-, 3^-)$  state at 10189.59 keV. These are closest tabulated transition energies available, however it's not sure how these states are being fed. The double-humped structure was thought initially to be caused by an incorrect Doppler correction. However, once the Doppler correction was removed, 3 peaks emerged showing that these double peaks were in fact two separate transitions.

The coincident  $\gamma$ -ray spectrum for the state labelled x, in Figure 6.2 was very low in statistics. However, only two distinct peaks were visible, the 1778.97-keV and a  $10704.126 \pm 3.766$ -keV transition. Therefore, this state must be preferentially decaying to the  $J^\pi = 2_1^+$  state, but again it's very difficult to make an assignment.

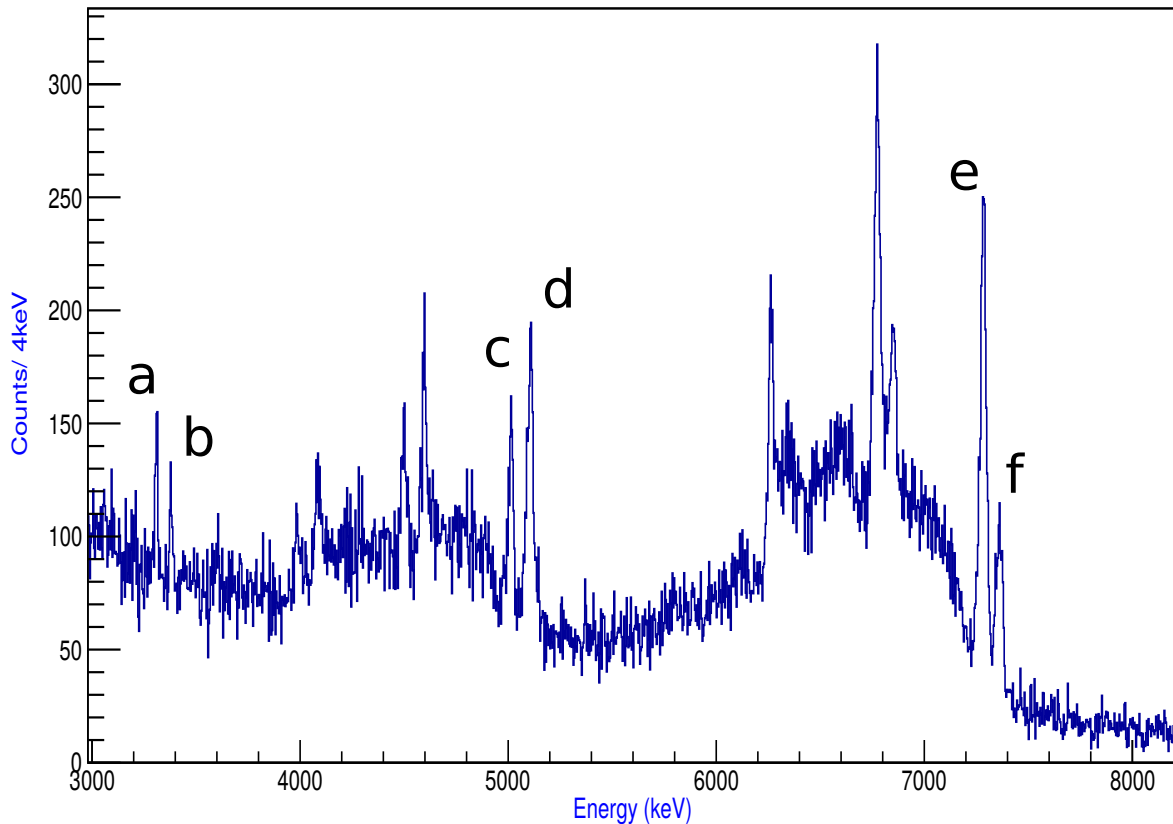


Figure 6.9:  $\gamma$ -ray spectrum for the unassigned state labelled w in Figure 6.2. Showing clear transitions at shows distinct transitions at:  $3309.607 \pm 0.8092$ ,  $3379.123 \pm 1.286$ ,  $5013.292 \pm 0.977$ ,  $5105.487 \pm 0.846$ ,  $7283.338 \pm 0.514$  and  $7360.351 \pm 1.130$  keV, labelled from a to f respectively.

## 6.6 Search for the SD in-band transition

The  $J^\pi=(4_7^+)$  state at 10.944 MeV was identified by gating on the peak labelled t in Figure 6.2. All of the known transitions from the  $J^\pi=(4_7^+)$  state are summarised in Table 6.2. All of these transitions were observed and are shown in Figures 6.10-6.12 for low, intermediate and high energy ranges respectively. There is a high photopeak and escape peak density, particularly in the intermediate energy range. The dotted lines track each photopeaks associated single and double escape peak for them to be more easily identified.

Other transitions, that could not be associated to the  $J^\pi=(4_7^+)$  state can be attributed to the  $J^\pi=(3_7^-)$  at 11078.52 keV. All of the direct transitions from this state are summarised in Table 6.2

Table 6.2: Data from ENSDF evaluated data tables on relevant electromagnetic transitions in  $^{28}\text{Si}$  (Shamsuzzoha Basunia, 2013).

$\text{Ex}_i$ (keV)	$\text{J}_i^\pi$	$\text{T}_{1/2}$	$\text{E}_\gamma$ (keV)	$\text{I}_\gamma$	$\text{J}_f^\pi$	$\text{Ex}_f$ (keV)
10944.0	$(4^+)$	15 fs	2685.0	26	$2^{(+)}$	8258.74
			3527.3	42	$2^+$	7416.26
			3562.9	21	$2^+$	7380.59
			9161.8	100	$2^+$	1779.030
10994	$(1,2^+)$	-	9212	100	$2^+$	1779.030
11078.52	$(3^-)$	-	1696.9	20	$2^+$	9381.55
			1762.5	34	$3^+$	9315.92
			3661.8	49	$2^+$	7416.26
			4801.4	83	$3^+$	6276.20
			9296.2	100	$2^+$	1779.030

Figure 6.10 shows the gated spectrum at intermediate energies, the known transitions from the proposed SD band state are all identified at this energy range. The 2881.13-keV peak labelled, a, has the closest known matching energy from the  $\text{J}^\pi=(4^+)$  state at 9164.68 keV. Unfortunately, the transition energy between the 10944.0 keV state and the 9164.68 keV state is 1779.32 keV. This directly overlaps with the  $\text{J}^\pi=2_1^+$  to ground state transition and therefore would not be resolved. Therefore the origin of the 2881.13-keV peak is still unknown.

The 3202.37 keV peak labelled, b, is most likely from the  $\text{J}^\pi=0^+$  state at 4979.92 keV. This state could be fed from the 10944.0 keV state via its cascade to the  $\text{J}^\pi=2^{(+)}$  state at 8258.74 keV. The peak labelled c at 2236.35 keV is a contaminant transition from  $^{30}\text{Si}$ ,  $\text{J}^\pi=2_1^+$  to the ground state.

One of the highest energy  $\gamma$ -ray transitions measured in this experiment was at  $11007.17 \pm 0.65$  keV, as seen in Figure 6.11, labelled x. There are no known transitions at this energy, the best candidate is the  $\text{J}^\pi=(1^+,2^+)$  at  $10994.0 \pm 2$  keV. These assignments are very tentative at this stage and require  $\gamma$ - $\gamma$  analysis for confirmation.

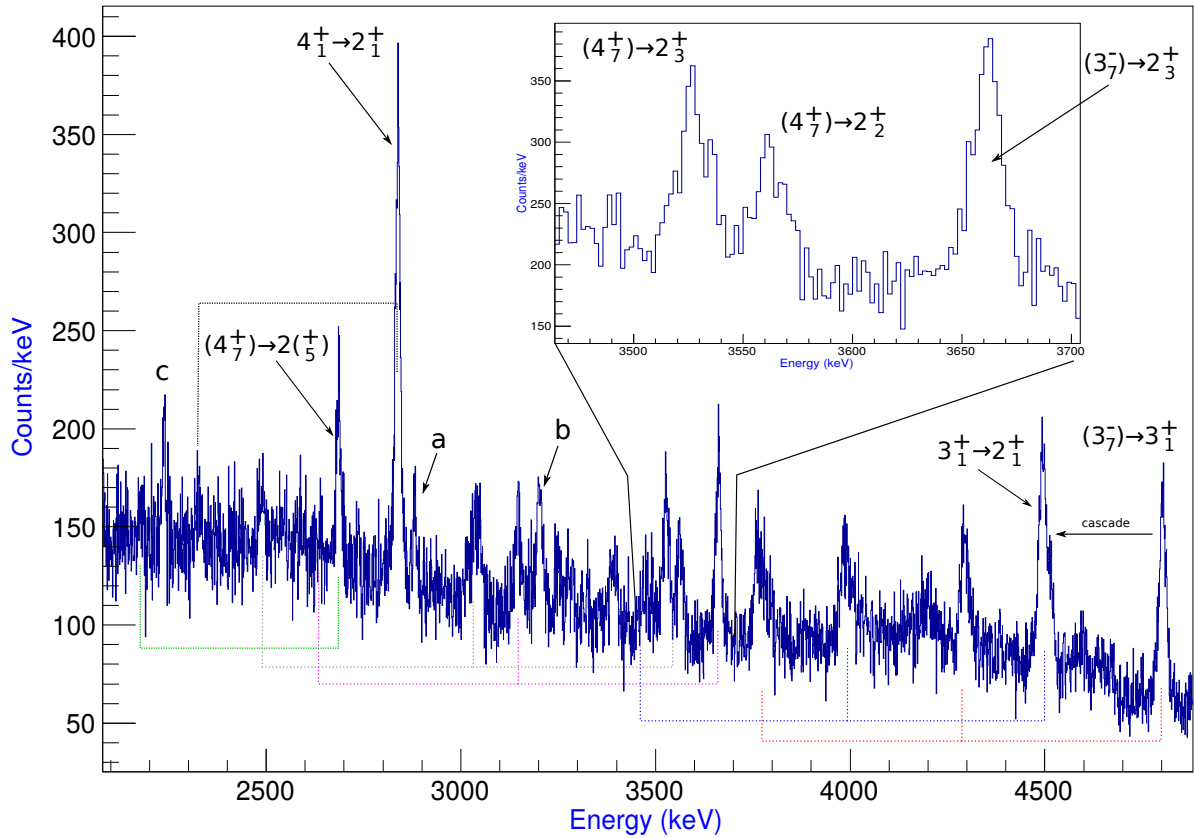


Figure 6.10:  $\gamma$ -ray spectrum for the proposed superdeformed band at intermediate energy range. The transitions from the  $J^\pi=(4_7^+)$  at  $10944.0 \pm 2$  keV of the proposed SD band are all labelled. These can be seen at 2685.0, 3527.3 and 3562.9 keV. The insert, is a close up around the 3527.3 and 3562.9 keV transitions showing they can be resolved. Peak labelled a at 2881.13 keV could be from the  $J^\pi=(3^-)$  state at 9164.68 keV. The peak labelled b at 3202.37 keV is most likely from the  $J^\pi=0^+$  at 4979.92 keV, which has a transition at 3200.7 keV. The peak labelled c is a contaminant line from  $^{30}\text{Si}$ .

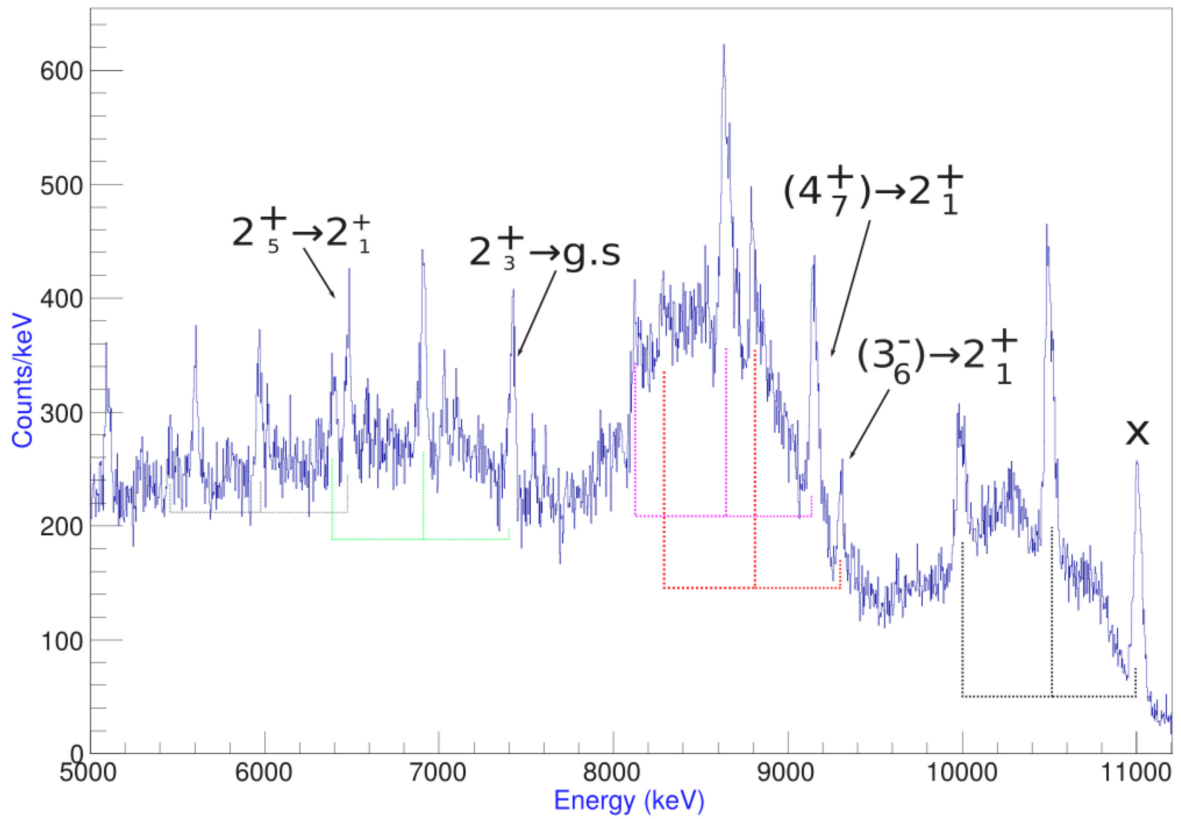


Figure 6.11:  $\gamma$ -ray spectrum for the proposed superdeformed band at high energy. The  $11007.17 \pm 0.65$  keV peak, labelled x, is an unknown transition. It's most likely from the  $J^\pi=(1^+, 2^+)$  state at  $10994.0 \pm 2$  keV. The other visible peaks are from known transitions from  $^{28}\text{Si}$ . Most importantly is the peak at around 9161.0 keV, identified as the  $J^\pi=(4_7^+)$  at 10944.0 keV to the  $J^\pi=2_1^+$  state at 1779.030 keV.

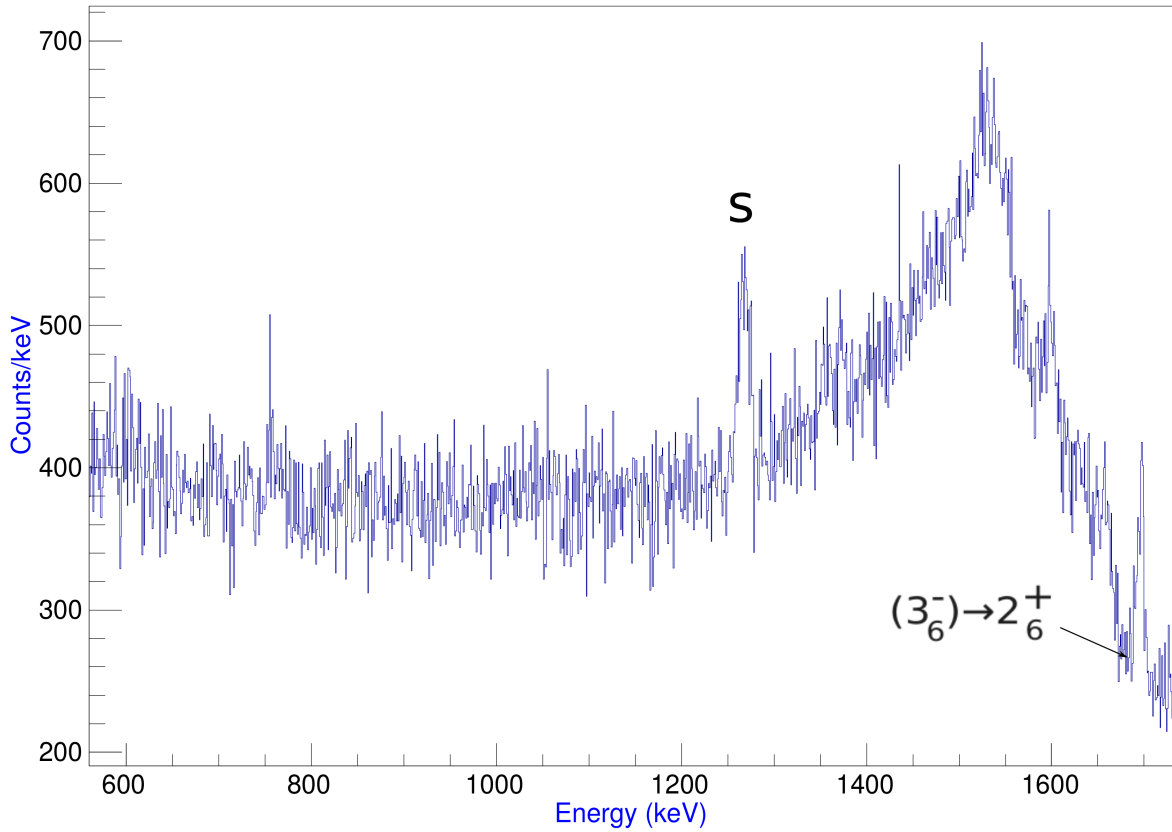


Figure 6.12:  $\gamma$ -ray spectrum for the proposed superdeformed band at low energy. There are no clear transitions in the expected region around 1150 keV. The only transition visible, labelled s, is the single escape from the  $J^\pi=2_1^+$  to g.s transition.

The  $J^\pi=(4_7^+)$  was identified as the best candidate member state of the proposed SD band. The in-band transition from the  $J^\pi=(4_7^+)$  to the  $J^\pi=(2^+)$  of the same proposed band is expected at around 1150 keV. Figure 6.12 shows the low energy region of the  $J^\pi=(4_7^+)$  gate. Unfortunately, there is no clear transition around this region. This meant, no direct calculation of the in-band transition strength could be made.

## 6.7 $\gamma$ -branching ratios

The procedure for the  $\gamma$ -decay branching ratio,  $BR_\gamma$  calculations were as follows:

- Gate on the state of interest, as seen in Figure 6.2.
- The  $\beta$  used for Doppler correction depended on the lifetime as detailed in Chapter 5.
- Project onto the  $\gamma$ -ray energy axis.
- Only direct transitions were then considered.
- Fit the  $\gamma$  peak of interest using the fitting procedure, as previously detailed during the discussion of the CAGRA efficiency calculations to obtain the area (raw counts).

Table 6.3 is a detailed example of how the  $BR_\gamma$  values were obtained for the  $J^\pi=(4_7^+)$  state. First the raw counts of each  $\gamma$ -ray transition of the state was scaled by the absolute efficiency  $\epsilon_{\text{abs}}$ :

$$\text{Scaled Counts} = \frac{\text{Raw Counts}}{\epsilon_{\text{abs}}}, \quad (6.2)$$

where  $\epsilon_{\text{abs}}$  was calculated for the entire CAGRA array at each corresponding  $\gamma$ -ray energy. The errors were calculated using the standardised propagation of errors method. The total number of scaled counts was then calculated by summing over each branches scaled counts, with their errors added in quadrature. This value was then used to normalise the scaled counts of each branch, to obtain the  $\gamma$ -ray branching ratio,  $BR_\gamma$ . The branching ratio of the 9161.8-keV transition is dominant, this is consistent with the phase space availability.

Table 6.3:  $\gamma$ -ray branching ratio calculations for the  $J^\pi=(4_7^+)$  state and calculated B(E2) and W.u values

Focal Plane Counts	Gate	$\sum$ Scaled Counts				
$8.877 \pm 0.013 \times 10^6$	t	$1.1097 \pm 0.0021 \times 10^6$				
$\gamma$ -ray Transition	Energy (keV)	Raw Counts	$\epsilon_{\text{abs}}(\%)$	Scaled Counts ( $10^3$ )	$\frac{\text{Scaled Counts}}{\text{Focal Plane Counts}}(\%)$	
$J^\pi=(4_7^+) \rightarrow J^\pi = 2_1^+$	9161.8	$2853.82 \pm 53.42$	$0.3277 \pm 0.0047$	$870.97 \pm 20.58$	$9.811 \pm 0.232$	
$J^\pi=(4_7^+) \rightarrow J^\pi = 2_2^+$	3562.9	$893.83 \pm 29.90$	$1.3487 \pm 0.0177$	$66.27 \pm 2.38$	$0.747 \pm 0.027$	
$J^\pi=(4_7^+) \rightarrow J^\pi = 2_3^+$	3527.3	$1287.15 \pm 35.88$	$1.3611 \pm 0.0178$	$94.57 \pm 2.91$	$1.065 \pm 0.033$	
$J^\pi=(4_7^+) \rightarrow J^\pi = 2_5^+$	2685.0	$1316.48 \pm 36.28$	$1.6911 \pm 0.0218$	$77.85 \pm 2.37$	$0.877 \pm 0.027$	
	$T_{1/2}$ (fs)	$\lambda$ ( $\text{s}^{-1}$ )	B(E2) <sub>s.p.</sub>			
$J^\pi=(4_7^+)$	$15 \pm 10$	$4.62 \pm 3.08 \times 10^{13}$	5.0505			
$\gamma$ -ray Transition	Energy (keV)	BR $_\gamma(\%)$	B(E2) <sub>exp</sub> / $\lambda$ ( $10^{-12}$ )	$\lambda_i$ ( $\text{s}^{-1}$ ) ( $10^{12}$ )	B(E2) <sub>exp</sub>	W.u
$J^\pi=(4_7^+) \rightarrow J^\pi = 2_1^+$	9161.8	$78.49 \pm 2.38$	0.013	$36.3 \pm 24.2$	$0.459 \pm 0.307$	$0.0908 \pm 0.0606$
$J^\pi=(4_7^+) \rightarrow J^\pi = 2_2^+$	3562.9	$5.97 \pm 0.24$	1.42	$2.76 \pm 1.84$	$3.924 \pm 2.621$	$0.7769 \pm 0.5189$
$J^\pi=(4_7^+) \rightarrow J^\pi = 2_3^+$	3527.3	$8.52 \pm 0.31$	1.49	$3.94 \pm 2.63$	$5.887 \pm 3.931$	$1.1657 \pm 0.7783$
$J^\pi=(4_7^+) \rightarrow J^\pi = 2_5^+$	2685.0	$7.02 \pm 0.25$	5.85	$3.24 \pm 2.16$	$18.964 \pm 12.661$	$3.7548 \pm 2.5069$

As all of the transitions tabulated here are E2 transitions, the formula from Table 2.1 was used to calculate the B(E2)<sub>exp</sub>/ $\lambda_i$  values. The partial decay constant is required here, this is calculated by:

$$\lambda_i = \text{BR}_\gamma \times \lambda. \tag{6.3}$$

Where  $\lambda$ , is the decay constant for the  $J^\pi=(4_7^+)$  state, which is known but has a considerably large error. The W.u values are then simply calculated as detailed in Chapter 2.

The BR $_\gamma$  calculations was repeated for all states observed in this research. The results of this is summarised in a derived level scheme, Figure 6.13. The widths represent the relative fraction of direct  $\gamma$ -decays in coincidence with a gated state on the focal plane spectrum. The red lines represent new transitions and blue states were not observed directly in the experiment.

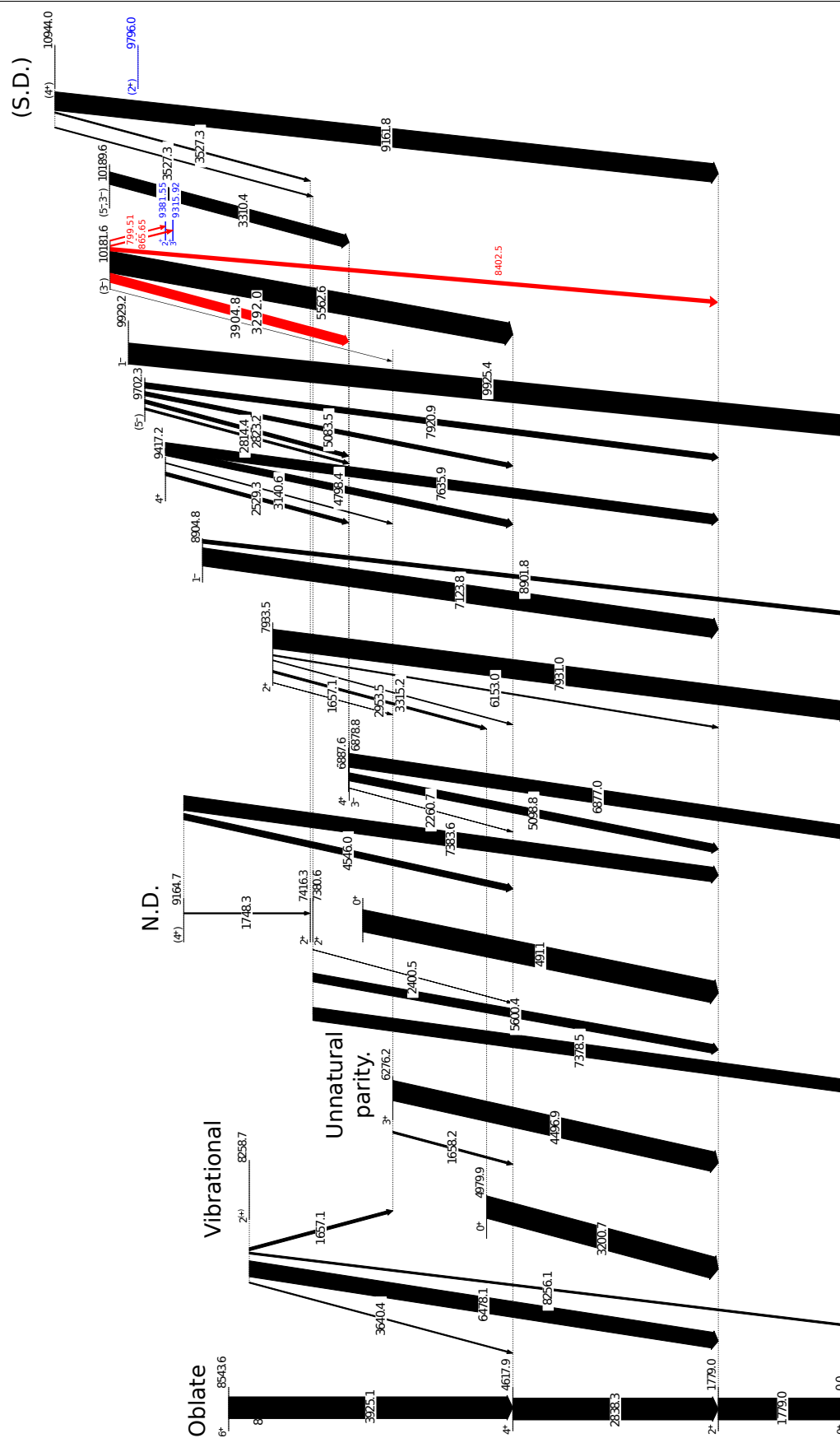


Figure 6.13: Derived level Scheme for all direct  $\gamma$ -ray transitions observed from populated states in  $^{28}\text{Si}$ . The width represent the relative fraction of direct  $\gamma$ -decays in coincidence with a gated state on the focal plane spectrum. Red lines are new transitions and blue lines were not observed directly.

## 6.8 Angular Correlations

The best candidate to study the  $\alpha'$ - $\gamma$  angular correlations was the  $J^\pi=4_1^+ \rightarrow 2_1^+$  transition of the oblate ground-state band. The optical potential used in the DWBA calculations to produce the m-state population distribution was taken from a study by M. Nolte *et al* (1987). They derived global optical potentials parameters for  $\alpha$  inelastic scattering above 80 MeV, see Table 6.4. The real,  $V(A,Z,E_\alpha)$ , and imaginary,  $W(A,E_\alpha)$ , were of the form:

$$V(A, Z, E_\alpha) = a_0 + a_1 A^{-\frac{1}{3}} + a_2 E_\alpha, \quad (6.4)$$

$$W(A, E_\alpha) = b_0 + b_1 A^{\frac{1}{3}} + b_2 E_\alpha. \quad (6.5)$$

The form factors used in the DWBA calculations also require diffuseness parameters. Which again research by M. Nolte *et al* derived expressions for the real,  $a_v$ , and imaginary,  $a_w$ , form factor parameters of the form:

$$a_v = c_0 + c_1 A^{\frac{1}{3}}, \quad (6.6)$$

$$a_w = d_0 + d_1 A^{\frac{1}{3}}, \quad (6.7)$$

The parameters from Table 6.4 were then used in these expressions to calculate the values summarised in Table 6.5. The coupling of the  $J^\pi=4_1^+$  to the  $J^\pi=2_1^+$  and ground-state were also included in the Chuck3 calculations, in which the required form factor parameters were the same as used in Table 6.5. The produced m-state population distribution could then be used in angcor to produce the predicted angular correlation. In this particular case, inputs specific to a  $J^\pi=4_1^+ \rightarrow 2_1^+$  transition were used.

Table 6.4: Fitted Optical model potential parameters (Nolte et al., 1987).

Parameter	$a_0$ (MeV)	$a_1$ (MeV)	$a_2$	$b_0$ (MeV)	$b_1$	$b_2$	$c_0$ (MeV)	$c_1$ (MeV)	$d_0$ (MeV)	$d_1$ (MeV)
Value	101.1	6.051	-0.248	26.82	-1.7	0.006	0.817	-0.0085	0.602	-0.020

Table 6.5: Derived Optical model potentials and diffuseness parameters.

V (MeV)	W(MeV)	$a_v$	$a_w$
96.76	22.42	0.84	0.75

Table 6.6: Polar angles and corresponding azimuthal angle as used in angor

Polar	Azimuthal	Clovers
90°	22.5°	6, 7
135°	45.0°	14
90°	67.5°	5, 8
90°	112.5°	9, 12
135°	135.0°	15, 16
90°	157.5°	11

CAGRA had 8 detectors at a polar angle of 90° and 4 at 135°. Due to the symmetry of the angular distributions around the reaction plane, which was the horizontal plane in the laboratory frame, there were only 6 unique azimuthal clover angles from 12 detectors. Four from the 90° ring and two from the 135°. These values are summarised in Table 6.6. The azimuthal angle was defined as 0° in the horizontal plane on the same side as the ejectile, i.e. on the same side as the spectrometer. Therefore, 180° corresponded to the recoil direction in this plane.

To compare experimental angular correlations to theoretical predictions, angor was ran for each azimuthal angle and the  $W(\theta)$  value was taken depending on which polar ring it belonged to.

The results from angor if integrated over the full solid angle will yield  $4\pi$ , therefore are internally normalised. Therefore, the experimental angular distributions were arbitrarily scaled for comparison. Table 6.7 summarises the steps to obtain the experimental angular correlation for the  $J^\pi=4_1^+ \rightarrow J^\pi=2_1^+$  transition. The total number of counts from each PHID group were first scaled by:

$$\frac{\sum C_i}{\sum \epsilon_i} = \frac{\text{Group Counts}}{\text{Group } \epsilon_{\text{abs}}}, \quad (6.8)$$

where,  $\sum C_i$  and  $\sum \epsilon_i$  represent the summation over all counts and absolute efficiencies for each clover in each PHID group. The group counts are then scaled by the group efficiency to get the scaled group counts. The results were then scaled down by the rescale factor to produce the  $W(\theta)_{\text{exp}}$  values. This could then be directly compared to the angor results,  $W(\theta)_{\text{theory}}$  and are plotted in Figure 6.14.

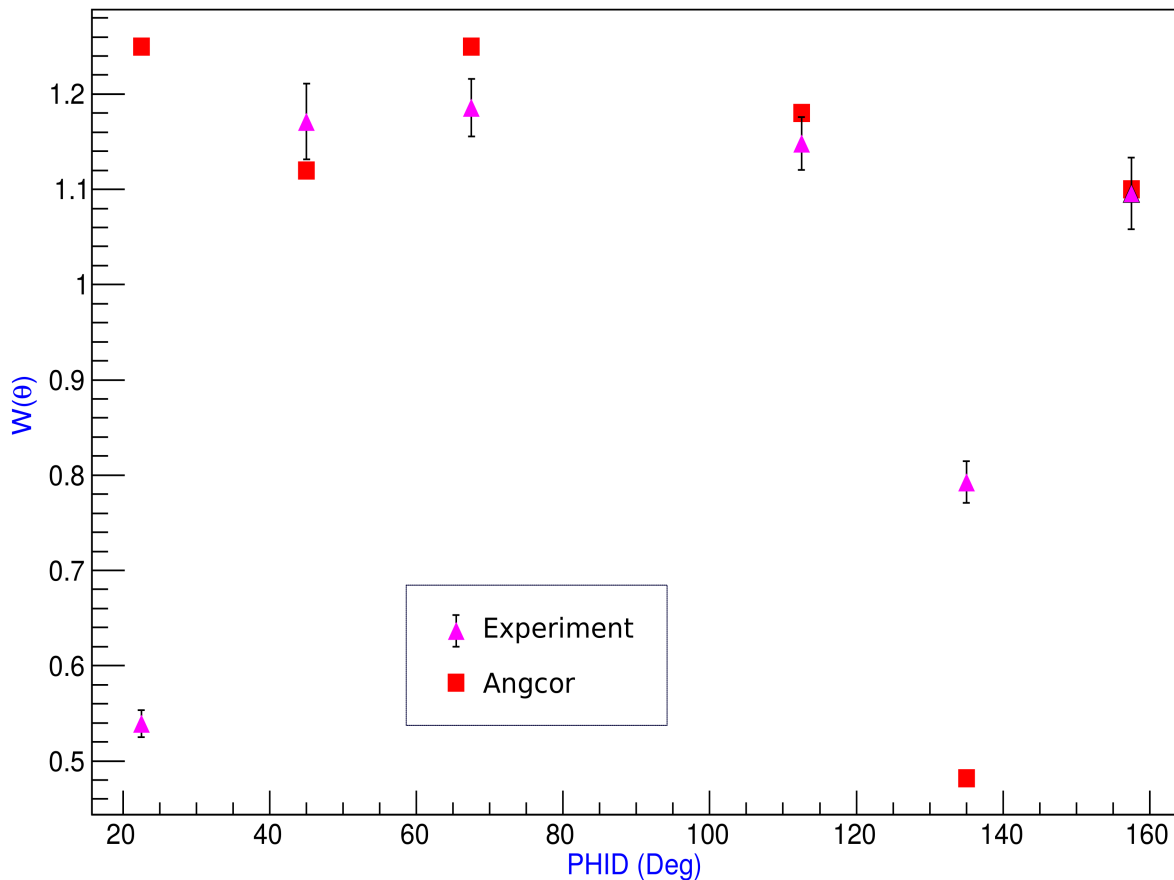


Figure 6.14: Experimental angular correlations compared to angcor for the  $J^\pi=4_1^+ \rightarrow 2_1^+$  transition. The distributions are well correlated except for the clear discrepancy for  $\text{PHID}=22.5^\circ$ .

The results do show promising signs and the distributions are correlated, however there is a clear discrepancy at  $\text{PHID}=22.5^\circ$ . As angcor is the only program that exist that is capable of calculating such angular distributions, there is no way currently of benchmarking its reliability. The angular distributions will have an effect on the previously calculated  $\text{BR}_\gamma$  values. As the measured counts for each detector will have to be re-scaled depending on their associated  $W(\theta)$  values. Due to this discrepancy, it was chosen to not include the angular correlations in the proceeding analysis to be discussed. Furthermore, for the SD band there has been no detailed coupled channel calculations research. This information is required to obtain accurate m-state population distributions for the SD band and therefore accurate angular correlations.

Table 6.7: Results from the experimental angular correlation analysis in comparison to angcor.

Transition	$\gamma$ -ray Energy (keV)	Rescale Factor			
$J^\pi=4_1^+ \rightarrow J^\pi=2_1^+$	2838.29	$1.872 \times 10^{-7}$			
PHID	Group Counts ( $10^3$ )	Group $\epsilon_{\text{abs}}$ (%)	Scaled Group Counts ( $10^6$ )	Rescaled $W(\theta)_{\text{exp}}$	Angcor $W(\theta)_{\text{theory}}$
22.5°	6.38±0.08	0.222±0.005	2.88±0.08	0.539±0.014	1.25
45.0°	8.83±0.09	0.141±0.003	6.26±0.21	1.171±0.040	1.12
67.5°	14.95±0.12	0.236±0.005	6.22±0.16	1.186±0.030	1.25
112.5°	14.94±0.12	0.244±0.005	6.13±0.15	1.148±0.028	1.18
135.0°	28.26±0.17	0.354±0.013	4.23±0.12	0.793±0.022	0.48
147.5°	6.78±0.08	0.116±0.003	5.85±0.20	1.096±0.038	1.1

## 6.9 $\gamma$ - $\alpha$ Branching ratios

The  $\alpha$ -breakup threshold in  $^{28}\text{Si}$  is 9984.14 keV. Therefore, in principle states below this energy should have a 1:1 ratio between CAGRA and the focal plane detector, once accounting for all necessary efficiencies:

$$\frac{\text{Focal Plane}}{\epsilon_{fp}} = \frac{\text{CAGRA}}{\epsilon_{fp}\epsilon_\gamma}, \quad (6.9)$$

where  $\epsilon_{fp}$  is the absolute efficiency of the focal plane detector. Grand Raiden data acquisition was simultaneously ran in coincident and in singles mode. Therefore, in singles mode only its own efficiency is required to get the true absolute state population. However, CAGRA was only operated in coincidence mode with the GR. Therefore, the overall efficiency is now the product of both detector systems absolute efficiencies. As you can see from Equation 6.9,  $\epsilon_{fp}$ , is a common denominator and therefore overall it is independent of  $\epsilon_{fp}$ .

Above the  $\alpha$ -breakup threshold, this process will start to compete with  $\gamma$ -decay. Therefore it can no longer be assumed that the ratio of the focal plane to CAGRA events will be 1:1. Any decrease in counts from CAGRA can then be assumed to be due to  $\alpha$ -breakup, therefore the ratio of CAGRA to the focal plane can be assumed to be the  $\gamma/\alpha$  branching ratio,  $\text{BR}_{\gamma/\alpha}$ .

Table 6.8: CAGRA to focal plane ratios for all states populated in  $^{28}\text{Si}$ .

Ex (keV)	$\frac{\sum_{\lambda_i} \text{Scaled Counts}}{\text{FocalPlaneCounts}}$ (%)	Scaled by Weighted Av (< 9984.14 keV)
4617.86	$45.87 \pm 0.61$	$1.06 \pm 0.12$
6690.74	$42.80 \pm 0.44$	$0.99 \pm 0.11$
7933.45	$41.26 \pm 0.76$	$0.95 \pm 0.11$
8904.8	$41.71 \pm 0.58$	$0.96 \pm 0.11$
9702.34	$46.85 \pm 0.53$	$1.08 \pm 0.12$
9929.2	$42.97 \pm 0.83$	$0.99 \pm 0.11$
10181.6	$29.73 \pm 0.40$	$0.68 \pm 0.08$
10944	$12.50 \pm 0.24$	$0.29 \pm 0.03$
11078.52	$7.15 \pm 0.13$	$0.16 \pm 0.02$

The summed counts of all  $\gamma$ -branches were scaled for absolute photopeak efficiency of CAGRA, at the appropriate energy. This was then divided by the total number of counts from that state, given by the background subtracted integral from the focal plane spectrum, in GR singles mode as seen in Figure 4.6.

The results are summarised in Table 6.8. There is a clear discrepancy for values belonging to states below the  $\alpha$ -breakup threshold, where they are expected to be 1:1. Assuming this is an unknown systematic error that is common to all data points, then these values can be re-normalised.

This was achieved by calculating the weighted average of all the data points below the threshold and re-normalising all data points by this value. The re-normalised error was calculated by taking the standard deviation using the weighted average, then taking the standard error, yielding  $0.434 \pm 0.048$ . Both the raw values and re-normalised values are plotted in Figure 6.15, the data points are summarised in Table 6.8. The re-scaled data points below the threshold energy are all 1:1 within error.

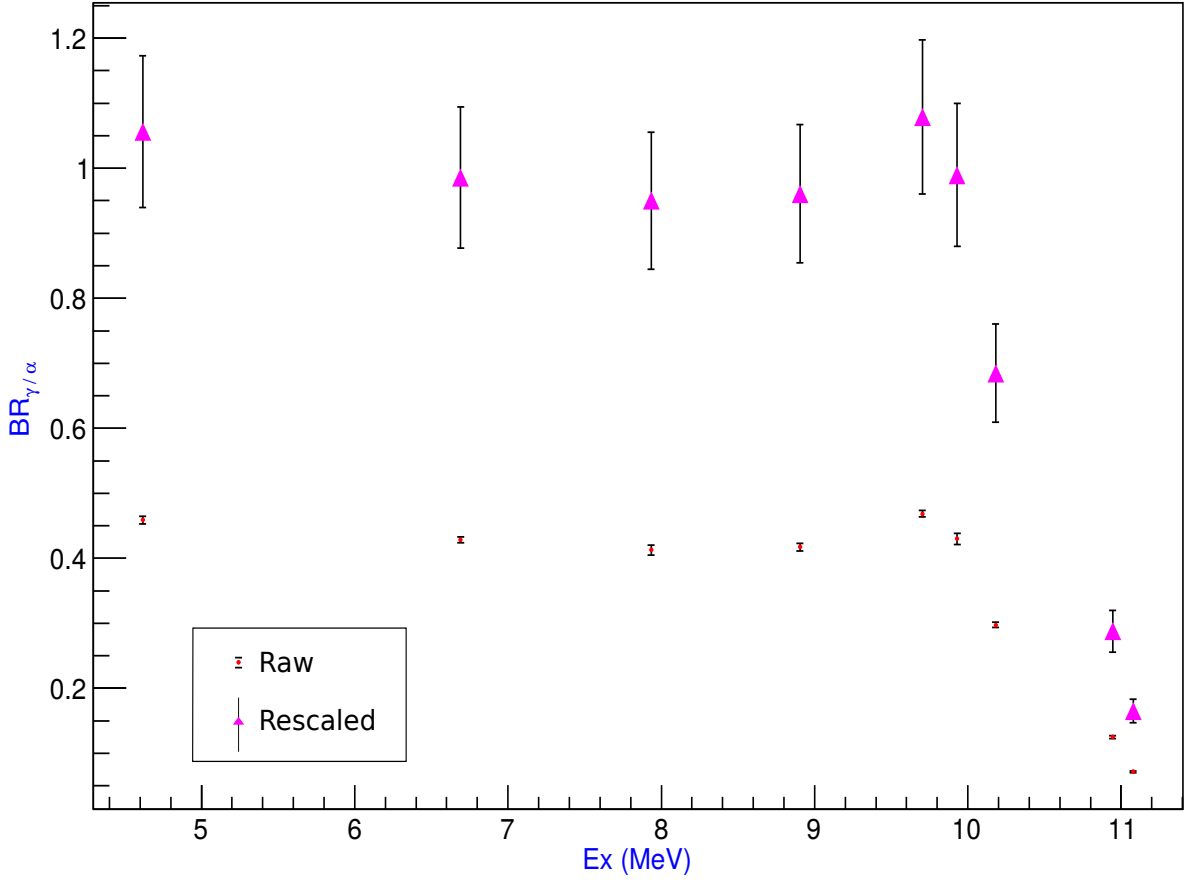


Figure 6.15: Raw and re-scaled  $BR_{\gamma/\alpha}$  plotted against excitation energy (MeV). Here,  $BR_{\gamma/\alpha}$  should be 1.0 at excitation energies below the  $\alpha$ -breakup threshold, which is at 9984.14 keV. Above the threshold,  $\alpha$ -breakup will start to compete with  $\gamma$ -decay and so  $BR_{\gamma/\alpha}$  decreases.

Both the raw and re-scaled  $BR_{\gamma/\alpha}$  values still significantly decrease after the breakup threshold is exceeded, showing there is sensitivity to the  $BR_{\gamma/\alpha}$ .

The  $BR_{\gamma/\alpha}$  has an effect on the calculated W.u values previously discussed. The W.u values calculated for the  $J^\pi=(4_7^+)$  state for each  $\gamma$ -branch in Table 6.3 have to be scaled by  $BR_{\gamma/\alpha}$ :

$$W.u_{\gamma/\alpha} = W.u \times BR_{\gamma/\alpha}. \quad (6.10)$$

This adjustment has the effect of reducing the apparent strength of the previously calculated transition strengths, as detailed in Table 6.9.

Table 6.9: W.u calculations scaled by  $BR_{\alpha/\gamma}$  values for the  $J^\pi=(4_7^+)$  state

$\gamma$ -ray Transition	Energy (keV)	W.u	W.u $\times BR_{\gamma/\alpha}$
$J^\pi=(4_7^+) \rightarrow J^\pi = 2_1^+$	9161.8	$0.0908 \pm 0.0606$	$0.0261 \pm 0.0177$
$J^\pi=(4_7^+) \rightarrow J^\pi = 2_2^+$	3562.9	$0.7769 \pm 0.5189$	$0.2237 \pm 0.1516$
$J^\pi=(4_7^+) \rightarrow J^\pi = 2_3^+$	3527.3	$1.1657 \pm 0.7783$	$0.3356 \pm 0.2273$
$J^\pi=(4_7^+) \rightarrow J^\pi = 2_5^+$	2685.0	$3.7548 \pm 2.5069$	$1.0810 \pm 0.7321$

## 6.10 SD In-Band transition B(E2) limit

As previously discussed, the in-band transition of the proposed SD band was not directly observed in this research. However, since this research has calculated the transition strengths for all of the known out of band transitions and accounted for the  $BR_{\gamma/\alpha}$  ratios, a limit can now be set on its transition strength.

This was achieved by fixing the centroid and FWHM of a Gaussian fit to the flat region as shown in Figure 6.12. The average FWHM for this energy was then used,  $FWHM_{av} = 6.93$  keV. The in-band transition was expected to be at 1148.05 keV and so the centroid was fixed to this position. The only free parameters was the area of the Gaussian and the linear background parameters. The fit yielded  $59.6 \pm 63.5$  net counts above background. The large error of course was expected from the nature of the fitting procedure. Assuming this was now a new  $\gamma$ -branch addition to the  $J^\pi=(4_7^+)$  state, the same analysis was repeated to calculate the updated W.u and  $W.u_{\gamma/\alpha}$  values, as previously detailed.

Table 6.10: Updated transitions strength with the addition of the in-band transition estimate.

$BR_\gamma$	$B(E2)/\lambda$	$\lambda_i$	$B(E2)_{\text{exp}}$	W.u	$W.u_{\gamma/\alpha}$
$0.0020 \pm 0.0023$	$4.09 \pm \times 10^{-10}$	$9.82 \pm 12.3 \times 10^{10}$	$40.18 \pm 50.55$	$7.96 \pm 10.01$	$2.29 \pm 3.79$

With this addition, the transitions strengths for the known branches did not change significantly and all remain the same, within error. This is due to the very small contribution to the overall statistics from the newly added in-band  $\gamma$ -branch. The results for the transition strength of this branch are summarised in Table 6.10.

Taking the upper limit of,  $W.u_{\gamma/\alpha}$ , from its error gives 6.08 W.u for the in-band transition strength of the proposed superdeformed band in  $^{28}\text{Si}$ .

# Chapter 7

## Conclusions & Further Work

A bespoke coupling of a Clover array to a high resolution spectrometer was met with many experimental and engineering challenges that were overcome in the efforts of the CAGRA campaign. It's clear from this research that there is still a great amount to be learnt about the structure  $^{28}\text{Si}$ , particularly above the  $\alpha$ -breakup threshold. Great effort was undertaken many years ago to calculate the widths and lifetimes of these states. Significant contributions came from proton and  $\alpha$ -inelastic scattering experiments, similar to this research. However, at that time, data acquisition capabilities were inadequate to handle  $\alpha'$ - $\gamma$  coincidences on the scale that the CAGRA campaign achieved. Furthermore, even now the application of state-of-the-art digital acquisition is still in its infancy. The rate dependent shift that affected CAGRA is a prime example of this. This research has therefore contributed to its characterisation and development, the techniques developed here can be used again in later research.

There is still a large gap in the  $\gamma$ -ray spectroscopy of  $^{28}\text{Si}$  at high excitation energy. CAGRA has shown it's possible and practical to study a vast number of states over a wide range in excitation energy, using its unique set-up. However, to really obtain its full potential, the coupled channel calculations need to be well understood and further research needs to be undertaken. A surprising number of tentative spin and parity assignments above 9.5 MeV still exist. A full description of the reaction mechanism through CC calculations, along with a complete understanding of the angular correlations using `angcor` could confirm these uncertainties and fill the gap in the data. This work also found new

$\gamma$ -ray transitions at high excitation, an achievement that has not been made for many years. Again, highlighting that there is still much to learn, even at stability.

The dominance of octupole deformation excitation in this data analysis is still not fully understood and this also supports the incentive for CC calculations to be applied. The possibility of multi-step excitation to the first  $J^\pi=3^+$  state is another aspect that could be explored in future work. This is exciting as further experimental evidence of a possible  $\gamma$ -band could be obtained, further adding to our knowledge of the nuclear structure of light nuclei.

Superdeformation in  $^{28}\text{Si}$  is still clearly an open question. However, this work has now supplied an upper limit to the transition strength of the in-band transition of the proposed superdeformed band, at a value of 6.08 W.u. As AMD calculations are now capable of predicting transition strengths it will be interesting to see in the future what constraints this can place on superdeformation in  $^{28}\text{Si}$ .

Further experimental and theoretical work is evidently required in order to improve the accuracy of this and subsequent research. Again, a deeper understanding of the coupled channel calculations would allow for more accurate angular correlations. This would then improve the accuracy of the derived  $\text{BR}_\gamma$  values needed to calculate the transition strengths of all the  $\gamma$ -branches from the proposed superdeformed band.

Experimentally, the coupled channel calculations would also increase the much needed population yield of the proposed superdeformed band region using inelastic scattering methods. The differential cross section predictions used for this research did not include the coupling of states at lower excitation to the  $J^\pi=4^+$  state of the proposed superdeformed band and most significantly other member states of this band. Including these could help maximise the much needed statistics. Firstly, by obtaining a more reliable optimum angle to study the  $\alpha$ -inelastic scattering. Secondly, optimising the set-up of the clover array based on the angular correlations, to obtain more PHID data points and through positioning detectors at angles corresponding to maxima from the improved angular correlations.

It is very unfortunate that the BGO suppression was not available during this research. As the majority of states fed the first  $J^\pi=2^+$  state, the 1778-keV transition to the

ground-state was singularly the strongest observed transition. The dominating Compton distribution from this transition overlaps directly with the expected region of the in-band transition of interest. Without effective BGO suppression, any transition with low statistics will not be resolved and will be folded into the background of the dominating Compton distribution.

The technique used to obtain the upper limit of the in-band transition strength was a reasonable first attempt. Nonetheless, there are more rigorous fitting procedures that can be used, for example maximum likelihood methods which are more reliable for low statistics analysis.

The full potential LaBr<sub>3</sub>-clover coincidence capabilities were not achieved in this research. Again, much more experimental testing is required to understand how this can be implemented more effectively. Gating on subsequent cascade transitions from the in-band transition in the LaBr<sub>3</sub> and looking for the direct in-band transition in the full clover array would have significantly reduced background. This technique could have significantly increased the probability of finding the first direct in-band transition of the proposed superdeformed band.

A much needed renaissance is due for the study of light stable nuclei. Their importance to nuclear structure theory gives a strong mandate for this change. Naturally, these were the first investigated nuclei and much of their low excitation structure is well studied. However, the technology required for detailed mapping of their high excitation landscape was beyond its years. The emergence of radioactive beams then pushed the attention to exotic nuclei and away from stability. Although, as this research has highlighted, it seems there is still an abundance of valuable discoveries yet to be made, even at stability. The CAGRA campaign has shown that the experimental techniques required are now possible and available. A push for a full theoretical description of the reaction mechanism and angular distribution used at CAGRA for <sup>28</sup>Si will give rise to a wealth of new information. This can be then used to validate the rich, varied and exciting nuclear model predictions that remain untested.

# Bibliography

Adsley, P., & Jenkins. 2017, Phys. Rev. C, 95, 024319. <https://link.aps.org/doi/10.1103/PhysRevC.95.024319>

Akkoyun, S., Algora, A., Alikhani, B., et al. 2012, Nuclear Instruments and Methods in Physics Research Section A: Accelerators, Spectrometers, Detectors and Associated Equipment, 668, 26 . <http://www.sciencedirect.com/science/article/pii/S0168900211021516>

Anni, R., Co', G., & Pellegrino, P. 1995, Nuclear Physics A, 584, 35 . <http://www.sciencedirect.com/science/article/pii/037594749400508K>

Bethe, H. A., & Bacher, R. F. 1936, Rev. Mod. Phys., 8, 82. <https://link.aps.org/doi/10.1103/RevModPhys.8.82>

Borg, K. V. D., Harakeh, M., & Nilsson, B. 1979, Nuclear Physics A, 325, 31 . <http://www.sciencedirect.com/science/article/pii/0375947479901490>

Brandolini, F., & Ribas, R. 1998, Nuclear Instruments and Methods in Physics Research Section A: Accelerators, Spectrometers, Detectors and Associated Equipment, 417, 150 . <http://www.sciencedirect.com/science/article/pii/S0168900298006536>

Brenneisen, J., Grathwohl, D., Lickert, M., et al. 1995, Zeitschrift für Physik A Hadrons and Nuclei, 352, 149. <https://doi.org/10.1007/BF01298901>

Campbell, P., Moore, I., & Pearson, M. 2016, Progress in Particle and Nuclear Physics, 86, 127 . <http://www.sciencedirect.com/science/article/pii/S0146641015000915>

- Cao, X. G., & Kim, E. J. 2018, AIP, 2038, 1. <https://aip.scitation.org/doi/abs/10.1063/1.5078840>
- Chernykh, M., Feldmeier, H., Neff, T., von Neumann-Cosel, P., & Richter, A. 2007, Phys. Rev. Lett., 98, 032501. <https://link.aps.org/doi/10.1103/PhysRevLett.98.032501>
- Chiba, Y., Taniguchi, Y., & Kimura, M. 2017, Phys. Rev. C, 95, 044328. <https://link.aps.org/doi/10.1103/PhysRevC.95.044328>
- Courtine, F., Sanzelle, S., Pilleyre, T., & Miallier, D. 2014, Radiation Measurements, 61, 78 . <http://www.sciencedirect.com/science/article/pii/S1350448713003776>
- Cseh, J., & Riczu, G. 2016, Physics Letters B, 757, 312 . <http://www.sciencedirect.com/science/article/pii/S0370269316300612>
- Cseh, J., Riczu, G., & Darai, J. 2019, Physics Letters B, 795, 160 . <http://www.sciencedirect.com/science/article/pii/S0370269319303946>
- Cseh, J., & Scheid, W. 1992, Journal of Physics G: Nuclear and Particle Physics, 18, 1419. <https://doi.org/10.1088%2F0954-3899%2F18%2F8%2F014>
- Dewald, A., Möller, O., & Petkov, P. 2012, Progress in Particle and Nuclear Physics, 67, 786 . <http://www.sciencedirect.com/science/article/pii/S0146641012000713>
- D.Kleppner. 1991, Physics Today, 0, 9. <https://physicstoday.scitation.org/doi/10.1063/1.2810343>
- Eberth, J., & Simpson, J. 2008, Progress in Particle and Nuclear Physics, 60, 283 . <http://www.sciencedirect.com/science/article/pii/S0146641007000828>
- Ferguson, A. 1974, in Pure and Applied Physics, Vol. 40, Nuclear Spectroscopy and Reactions, Part C, ed. J. CERNY (Elsevier), 277 – 306. <http://www.sciencedirect.com/science/article/pii/B978012165203650012X>

- Flerov, G., & Ter-Akopian, G. 1987, Progress in Particle and Nuclear Physics, 19, 197 .  
<http://www.sciencedirect.com/science/article/pii/0146641087900068>
- Freer, M., Betts, R., & Wuosmaa, A. 1995, Nuclear Physics A, 587, 36 . <http://www.sciencedirect.com/science/article/pii/037594749400820D>
- Glatz, F., Betz, P., Siefert, J., Heidinger, F., & Röpke, H. 1981a, Phys. Rev. Lett., 46, 1559. <https://link.aps.org/doi/10.1103/PhysRevLett.46.1559>
- Glatz, F., Siefert, J., Betz, P., et al. 1981b, Zeitschrift für Physik A Atoms and Nuclei, 303, 239. <https://doi.org/10.1007/BF01424765>
- Hadyńska-Klęk, K., Napiorkowski, P. J., Zielińska, M., et al. 2016, Phys. Rev. Lett., 117, 062501. <https://link.aps.org/doi/10.1103/PhysRevLett.117.062501>
- Jenkins, D. G., Lister, C. J., Carpenter, M. P., et al. 2012, Phys. Rev. C, 86, 064308. <https://link.aps.org/doi/10.1103/PhysRevC.86.064308>
- Kanada-En'yo, Y., Kimura, M., & Ono, A. 2012, Progress of Theoretical and Experimental Physics, 2012, <http://oup.prod.sis.lan/ptep/article-pdf/2012/1/01A202/11578300/pts001.pdf>, 01A202. <https://doi.org/10.1093/ptep/pts001>
- Krane, K. S. 1987, Introductory Nuclear Physics (Wiley). <https://www.wiley.com/en-us/Introductory+Nuclear+Physics%2C+3rd+Edition-p-9780471805533>
- Kubono, S., Morita, K., Tanaka, M., et al. 1986, Nuclear Physics A, 457, 461 . <http://www.sciencedirect.com/science/article/pii/0375947486903891>
- Lamnii, A., Lamnii, M., & Oumellal, F. 2016, Applied Mathematics and Computation, 283, 355 . <http://www.sciencedirect.com/science/article/pii/S0096300316301795>
- Lopez-Martens, A., Lauritsen, T., Leoni, S., et al. 2016, Progress in Particle and Nuclear Physics, 89, 137 . <http://www.sciencedirect.com/science/article/pii/S0146641016000351>

- Möller, P., Sierk, A., Ichikawa, T., & Sagawa, H. 2016, Atomic Data and Nuclear Data Tables, 109-110, 1 . <http://www.sciencedirect.com/science/article/pii/S0092640X1600005X>
- Nilsson, S. G., Tsang, C. F., Sobiczewski, A., et al. 1969, Nuclear Physics A, 131, 1 . <http://www.sciencedirect.com/science/article/pii/0375947469908094>
- Nolte, M., Machner, H., & Bojowald, J. 1987, Phys. Rev. C, 36, 1312. <https://link.aps.org/doi/10.1103/PhysRevC.36.1312>
- Peach, T., Garg, U., Gupta, Y. K., et al. 2016, Phys. Rev. C, 93, 064325. <https://link.aps.org/doi/10.1103/PhysRevC.93.064325>
- Shamsuzzoha Basunia, M. 2013, Nuclear Data Sheets, 114, 1189
- Sheline, R. K., Kubono, S., Morita, K., & Tanaka, M. 1982, Physics Letters B, 119, 263 . <http://www.sciencedirect.com/science/article/pii/0370269382906669>
- Shima, Y., Hayashi, H., Kojima, Y., Jyousyou, R., & Shibata, M. 2016, Applied Radiation and Isotopes, 109, 535 , proceedings of the 20th International Conference on Radionuclide Metrology and its Applications 8–11 June 2015, Vienna, Austria. <http://www.sciencedirect.com/science/article/pii/S0969804315302712>
- Staszczak, A., & Wong, C.-Y. 2014, Physics Letters B, 738, doi:10.1016/j.physletb.2014.10.013
- Strutinsky, V. 1967, Nuclear Physics A, 95, 420 . <http://www.sciencedirect.com/science/article/pii/0375947467905106>
- Suda, T., & Simon, H. 2017, Progress in Particle and Nuclear Physics, 96, 1 . <http://www.sciencedirect.com/science/article/pii/S0146641017300376>
- Suda, T., & Wakasugi, M. 2005, Progress in Particle and Nuclear Physics, 55, 417 , international School of Nuclear Physics 26th course. <http://www.sciencedirect.com/science/article/pii/S0146641005000232>

- Svensson, C. E., Macchiavelli, A. O., Juodagalvis, A., et al. 2000, Phys. Rev. Lett., 85, 2693. <https://link.aps.org/doi/10.1103/PhysRevLett.85.2693>
- Tamii, A., Fujita, Y., Matsubara, H., et al. 2009, Nuclear Instruments and Methods in Physics Research Section A: Accelerators, Spectrometers, Detectors and Associated Equipment, 605, 326
- Tanabe, T., Haga, K., Yasue, M., et al. 1983, Nuclear Physics A, 399, 241 . <http://www.sciencedirect.com/science/article/pii/0375947483906061>
- Taniguchi, Y., Kanada-En'yo, Y., & Kimura, M. 2009, Phys. Rev. C, 80, 044316. <https://link.aps.org/doi/10.1103/PhysRevC.80.044316>
- Taniguchi, Y., Kimura, M., Kanada-En'yo, Y., & Horiuchi, H. 2007, Phys. Rev. C, 76, 044317. <https://link.aps.org/doi/10.1103/PhysRevC.76.044317>
- Terashima, S. 2018, CAGRA Internal Report
- Twin, P. J., Nyakó, B. M., Nelson, A. H., et al. 1986, Phys. Rev. Lett., 57, 811. <https://link.aps.org/doi/10.1103/PhysRevLett.57.811>
- Wang, M., Audi, G., Wapstra, A. H., et al. 2012, Chin.Phys.C, 36, 1603
- Weinert, M. 2019, CAGRA Internal Report
- Weisskopf, V. F. 1951, Phys. Rev., 83, 1073. <https://link.aps.org/doi/10.1103/PhysRev.83.1073>
- Wood, J., & Rowe, D. 2010, Fundamentals of nuclear models: Foundational Models, 52–55, doi:<https://doi.org/10.1142/6209>
- Zalmstra, J., Harakeh, M., & van Hienen, J. 1991, Nuclear Physics A, 526, 59 . <http://www.sciencedirect.com/science/article/pii/037594749190298K>
- Ziegler, J. F., Ziegler, M., & Biersack, J. 2010, Nuclear Instruments and Methods in Physics Research Section B: Beam Interactions with Materials and Atoms, 268, 1818

, 19th International Conference on Ion Beam Analysis. <http://www.sciencedirect.com/science/article/pii/S0168583X10001862>

Zielińska, M., & Gaffney, L. 2016, *The European Physical Journal A*, 55, doi:10.1140/epja/i2016-16099-8